

Electronic Thesis and Dissertation Repository

5-28-2024 12:00 PM

Investigating CO₂ Adsorption Behavior in Metal-Organic Frameworks by Solid-state NMR


Yan Ham Ng, *Western University*

Supervisor: Huang, Yining, *The University of Western Ontario*

A thesis submitted in partial fulfillment of the requirements for the Master of Science degree in Chemistry

© Yan Ham Ng 2024

Follow this and additional works at: <https://ir.lib.uwo.ca/etd>

 Part of the [Inorganic Chemistry Commons](#), [Materials Chemistry Commons](#), and the [Physical Chemistry Commons](#)

Recommended Citation

Ng, Yan Ham, "Investigating CO₂ Adsorption Behavior in Metal-Organic Frameworks by Solid-state NMR" (2024). *Electronic Thesis and Dissertation Repository*. 10151.
<https://ir.lib.uwo.ca/etd/10151>

This Dissertation/Thesis is brought to you for free and open access by Scholarship@Western. It has been accepted for inclusion in Electronic Thesis and Dissertation Repository by an authorized administrator of Scholarship@Western. For more information, please contact wlsadmin@uwo.ca.

Abstract

With increasing demands in controlling carbon dioxide emissions, metal-organic frameworks (MOFs) are considered as promising candidates for CO₂ capture due to their large CO₂ adsorption capacity. In this study, the adsorption behavior of CO₂ molecules in [Zn₂(TRZ)₂(NH₂-BDC)] (TRZ=1,2,4-triazolate, NH₂-BDC=2-amino-1,4-benzenedicarboxylic acid), and CALF-20 are studied. Moreover, water is ubiquitous in the atmosphere and could have a negative impact on the MOF's gas adsorption. Therefore, understanding the behavior of water and CO₂ in MOFs is of fundamental importance. Solid-state nuclear magnetic resonance (SSNMR) is a powerful technique which reveals guest molecules' behavior in MOFs. Herein, [Zn₂(TRZ)₂(NH₂-BDC)] was loaded with pure CO₂ and D₂O, and CALF-20 was loaded with pure CO₂ in this study. ²H and ¹³C variable temperature SSNMR was performed to investigate the behavior of CO₂ and D₂O in the framework. D₂O exhibits restricted motions between 173-213K and becomes more mobile with increasing temperature and increasing concentrations in [Zn₂(TRZ)₂(NH₂-BDC)]. CO₂ also shows higher mobility upon temperature increase for both MOFs. NMR results suggest that D₂O undergoes a π -flip flop motion and a 4-site jumping motion in [Zn₂(TRZ)₂(NH₂-BDC)]. Additionally, CO₂ undergoes C₂ hopping and C₃ wobbling motion for both MOFs. Once single component adsorption was examined, co-adsorption of CO₂ and water was also investigated for [Zn₂(TRZ)₂(NH₂-BDC)].

Keywords: Water adsorption, CO₂ adsorption, gas adsorption, metal-organic frameworks, SSNMR, CALF-20, variable temperature.

Summary for Lay Audience

Metal-organic frameworks (MOFs) are a class of 3D porous materials that have gained significant attention since 1990s due to their potential applications in gas storage and separation, catalysis, drug delivery, and energy conversion. In this study, 2 MOFs were selected due to their high CO₂ adsorption capability. Both MOFs are featured with the triazole ligands for a higher CO₂ affinity. The CO₂ motions in [Zn₂(TRZ)₂(NH₂-BDC)] and CALF-20 were investigated using SSNMR. The SSNMR experiments were conducted under variable temperatures to investigate the relationship between the change in temperature and adsorption behavior of CO₂ within the framework. Different amount of guest molecules was also loaded into the frameworks to study the influence on guest molecule motions. The motional information obtained from this study allows for better optimization of CO₂ adsorption based on humidity levels and temperatures.

Acknowledgement

First, I would like to thank my supervisor Professor Yining Huang for his support and guidance throughout my academic journey. His expertise in SSNMR and attention to detail have helped me a lot along the way towards conducting this thesis. I'm truly grateful for the effort and time he invested in my academics.

Secondly, I would like to extend my appreciation to my committee members: Dr. François Lagugné-Labarthe, Dr. Tsun-Kong Sham and Brian L. Pagenkopf, thank you for giving me precious advice and inputting effort towards the completion of my degree.

I would also like to express my gratitude towards the faculty and staff in the Department of Chemistry. I want to thank Dr. Mathew Williams for his help on the NMR experiments. I really appreciate all his support on data processing and troubleshooting for the instrument. I would also like to thank the 1st year chemistry supervisors and technicians that have helped me gain valuable experience during TAing: Naeem Shahid, Susan England, and Shan Jiang. Additionally, I want to thank Ms. Darlene McDonald for her great assistance during my program.

I would also like to thank the current and past members of our research group: Shuting Li, Wanli Zhang, Tahereh Azizvahed, Jingyan Liu, Jiabin Xu, Sandamini Alahakoon, and Yihao Shen. I'm truly grateful for the joyful environment they've created and the help they've provided me in the lab. It's been a wonderful experience working with all of them. I'm very lucky to have them as lab mates.

Special thanks to Dr. Vinicius Martins for supporting me with my project since my fourth year in undergrad. He has offered me an enormous amount of support countless times throughout my research experience. I really appreciate all the suggestions and insights he provided based on his research experience. He's been a very supportive mentor, coworker, and friend.

I also want to thank my friends for all the support they've provided during my study, they've helped me maintain my mental health at a healthy level. Thanks to Cédric Lambin, Lorena Veliz Portal, and Congyang Zhang for being therapeutic technical support humans in the office. Thanks to Hanxuan Cui for her late-night durian and mango pancakes. Thanks to Kirsty Ng for her suggestions when I started my studies. Thanks to Bingyu Dong and Jing Ma for their emotional

support when I was clearly not sane. Thanks to Yishu Shi for her flavoured vanilla extract and hand-drawing postcard when I was struggling with my thesis writing, those are the most targeted presents I've ever received.

Finally, I would like to thank my family for their support all these years. I'm really grateful to have my parents backing me up, they've been very supportive throughout the whole duration of my studies. I would also like to thank my brother for preventing me from starving by shovelling pizza slices onto my face when I was focusing too much on my studies. Without their support, I would not be where I am.

Thank you all for being part of my life.

Table of Contents

ABSTRACT	II
SUMMARY FOR LAY AUDIENCE	III
ACKNOWLEDGEMENT	IV
TABLE OF CONTENTS	VI
LIST OF TABLES	X
LIST OF FIGURES	XI
LIST OF APPENDICES	XVI
LIST OF ABBREVIATIONS	XVIII
CHAPTER 1. GENERAL INTRODUCTION	1
1.1. METAL-ORGANIC FRAMEWORKS (MOFs).....	1
1.1.1. MOFs as gas storage materials.....	2
1.1.2. Carbon dioxide (CO ₂) capture and storage.....	3
1.1.3. Water effects on CO ₂ adsorption in MOFs.....	4
1.1.4. pillar-layered MOFs.....	5
1.1.5. MOFs studied in this thesis.....	5
1.2. CHARACTERIZATION OF MOFs.....	10
1.2.1. X-ray Crystallography.....	10
1.2.2. Thermogravimetric analysis (TGA).....	12
1.3. SOLID-STATE NMR (SSNMR).....	12
1.3.1. NMR interactions.....	13

1.3.2.	Zeeman interactions	14
1.3.3.	Chemical shielding interaction	15
1.3.4.	Dipolar interaction	17
1.3.5.	J-coupling interaction.....	18
1.3.6.	Quadrupolar interaction	19
1.3.7.	SSNMR spectral simulations	21
1.3.8.	Probing CO ₂ adsorption behavior using static SSNMR	21
1.3.9.	Probing D ₂ O adsorption behavior using static ² H SSNMR.....	24
	REFERENCES:	25
CHAPTER 2. WATER EFFECTS ON CO₂ ADSORPTION IN MOF [Zn₂(TRZ)₂(NH₂-		
BDC)] AT DIFFERENT LOADING LEVELS AND TEMPERATURES		31
2.1.	INTRODUCTION.....	31
2.2.	EXPERIMENTAL SECTION	31
2.2.1.	MOF synthesis	31
2.2.2.	Sample activation.....	32
2.2.3.	Powder X-ray diffraction (PXRD) measurements	32
2.2.4.	Thermogravimetric analysis (TGA).....	33
2.2.5.	CO ₂ adsorption.....	33
2.2.6.	D ₂ O adsorption.....	33
2.2.7.	Co-adsorption of CO ₂ and D ₂ O.....	34
2.2.8.	Solid-State Nuclear Magnetic Resonance Spectroscopy (SSNMR).....	34
2.2.8.1.	Cross polarization Magic-angle spinning (CPMAS)	34
2.2.8.2.	Static SSNMR.....	34

2.2.8.3. Spectral simulations	35
2.3. RESULTS AND DISCUSSION	36
2.3.1. Characterization	36
2.3.1.1. PXRD results.....	36
2.3.1.2. TGA results	36
2.3.1.3. Distribution of guest molecules in ZTP-3	38
2.3.2. Static ¹³ C variable temperature (VT) SSNMR.....	39
2.3.3. Static ² H variable temperature (VT) SSNMR.....	47
2.3.4. Adsorption scenarios.....	56
2.3.5. MAS SSNMR	59
2.4. SUMMARY	62
REFERENCES	62

CHAPTER 3. CO₂ ADSORPTION IN CALF-20 AT DIFFERENT LOADING LEVELS

AND TEMPERATURES..... 65

3.1. INTRODUCTION.....	65
3.2. EXPERIMENTAL SECTION.....	65
3.2.1. MOF synthesis CALF-20.....	65
3.2.2. Sample activation.....	65
3.2.3. Powder X-ray diffraction (PXRD) measurements	66
3.2.4. Thermogravimetric analysis (TGA).....	66
3.2.5. CO ₂ adsorption.....	66
3.2.6. Solid-State Nuclear Magnetic Resonance Spectroscopy (SSNMR).....	66
3.3. RESULTS AND DISCUSSION.....	67

3.3.1. Characterization	67
3.3.1.1. PXRD results.....	67
3.3.1.2. TGA results	68
3.3.1.3.....	69
3.3.2. Static ¹³ C variable temperature (VT) SSNMR of CO ₂	70
3.3.3. Adsorption scenarios.....	78
3.3.4. MAS SSNMR	80
3.4. SUMMARY	81
REFERENCES	82
CHAPTER 4. CONCLUSIONS AND FUTURE WORK.....	84
4.1. CONCLUSIONS	84
4.2. FUTURE WORK.....	85
REFERENCES	85
APPENDICES.....	86
APPENDIX A2.....	86
APPENDIX A3.....	101
CURRICULUM VITAE	103

List of Tables

Table 1.1. CO ₂ uptake of MIL-120 under dry and wet flue gas ⁴⁸	4
Table 1.1 Spin quantum number <i>I</i> prediction based on number of protons and neutrons of the nucleus.	13
Table 1.2. Magnitudes of typical NMR interactions	14
Table 2.1. Average distribution of guest molecules within [Zn ₂ (TRZ) ₂ (NH ₂ -BDC)]	38
Table 2.2. VT ¹³ C static SSNMR simulation parameters ^{3,4} of CO ₂ signal 1 for 0.25eq CO ₂ /Zn and 0.25eq CO ₂ + 0.25eq D ₂ O loading.	44
Table 2.3. Free CO ₂ relative signal intensities at different loadings.....	46
Table 2.4. VT ² H static SSNMR spectra simulation parameters of D ₂ O signal 1 for 0.5eq D ₂ O/Zn and 0.25eq CO ₂ + 0.5eq D ₂ O loading.	52
Table 2.5. η _Q parameter extracted from 373 K ² H VT SSNMR for all loadings.	56
Table 3.1. average distribution of guest molecules within CALF-20.....	70
Table 3.2. VT ¹³ C static SSNMR simulation parameters ^{3,4} for 0.25eq CO ₂ loading.	75
Table 3.3. VT ¹³ C static SSNMR simulation parameters ^{3,4} for 0.5eq CO ₂ loading.	76
Table 3.4. VT ¹³ C static SSNMR simulation parameters ^{3,4} for 0.75eq CO ₂ loading.	77

List of Figures

Figure 1.1. schematic diagram of composition of MOFs. ¹²	1
Figure 1.2. Schematic diagram of different gas adsorption mechanisms in MOFs. ¹⁵	2
Figure 1.3. Schematic diagram for carbon capturing. ¹⁶	3
Figure 1.4. Simplified structure of pillar layered MOFs.....	5
Figure 1.5. Seven Zn-triazolate dicarboxylate MOFs from Zhai's work. ¹⁸	6
Figure 1.6. Components of $[\text{Zn}_2(\text{TRZ})_2(\text{NH}_2\text{-BDC})]^{18}$	7
Figure 1.7. Coordination on zinc in $[\text{Zn}_2(\text{TRZ})_2(\text{NH}_2\text{-BDC})]^{18}$	8
Figure 1.8. Components of Calf-20 ²⁰	9
Figure 1.9. Coordination on zinc in Calf-20 ²⁰	10
Figure 1.10. Schematic diagram for X-ray diffraction ¹⁹	12
Figure 1.11. Zeeman interaction when $I=1/2$	15
Figure 1.12. Chemical shielding components in 3 dimensions.....	16
Figure 1.13. SSNMR powder pattern showing 3 chemical shielding components.....	17
Figure 1.14. Dipolar interaction.....	18
Figure 1.15. Perturbation of first and second order interaction on Zeeman energy levels of nucleus with half-integer spin quantum number $I=3/2$	20
Figure 1.16. Quadrupolar interaction when $I=1$	21

Figure 1.17. Effects of a) span Ω ($\delta_{\text{iso}} = 125$ ppm, $\kappa = 1$) and b) skew κ ($\delta_{\text{iso}} = 125$ ppm, $\Omega = 200$ ppm) and c) isotropic chemical shift δ_{iso} ($\Omega = 200$ ppm, $\kappa = 1$) on the ^{13}C SSNMR pattern. 22

Figure 1.18. Simulated static ^{13}C SSNMR spectra of CO_2 undergoing a) C_3 wobbling motion at different angles, b) C_2 hopping motion at different angles, c) combined C_2 hopping and C_3 wobbling motion at different angles, d) Simulated ^{13}C SSNMR pattern of CO_2 undergoing C_2 hopping and C_3 wobbling at different jumping rates ($\alpha=40^\circ$, $\beta=40^\circ$). The spectra were simulated with Express²⁶ software. The ^{13}C SSNMR parameters of static CO_2 are $\delta_{\text{iso}} = 125$ ppm, $\Omega = 335$ ppm, and $\kappa = 1$ 23

Figure 1.19. a) Energy level diagram of ^2H ($I = 1$), b) Pake doublet pattern formed by ^2H 24

Figure 1.20. Effects of (a) quadrupolar coupling constant C_Q and (b) η_Q on the ^2H SSNMR pattern. 24

Figure 1.21. Simulated static ^2H SSNMR spectra of a) π -flipflop motion at an angle of 54° , b) 4 site jumping motion at an angle of 40° , c) combined π -flipflop and 4 site jumping motion $\alpha=54^\circ$ $\beta=40^\circ$. The spectra were simulated with Express²⁶ software. The ^2H SSNMR parameter of static D_2O are $C_Q = 215$ kHz, and $\eta_Q = 0$ 25

Figure 2.1. Powder X-ray diffraction pattern (PXRD) of $[\text{Zn}_2(\text{TRZ})_2(\text{NH}_2\text{-BDC})]$ and the simulated as-made PXRD pattern based on the crystal structure provided in the literature¹. 36

Figure 2.2. Thermogravimetric analysis (TGA) curves of as-made (black curve) and activated (blue curve) $[\text{Zn}_2(\text{TRZ})_2(\text{NH}_2\text{-BDC})]$ 37

Figure 2.3. (a) Possible 2 adsorption location in each $[\text{Zn}_2(\text{TRZ})_2(\text{NH}_2\text{-BDC})]$ cage (b) top view of top part (green) (c) bottom view of the bottom part (brown) 39

Figure 2.5. Simulated static ^{13}C SSNMR spectra of rigid CO_2 ($\delta_{iso}=125$ ppm, $\Omega = 335$ ppm, $\kappa = 1$). ¹²	40
Figure 2.6. Experimental VT static ^{13}C SSNMR spectra of CO_2 at different pure CO_2 loadings from 213 K to 373 K for MOF $[\text{Zn}_2(\text{TRZ})_2(\text{NH}_2\text{-BDC})]$	41
Figure 2.7. VT static ^{13}C SSNMR pattern of CO_2 with 0.75eq CO_2/Zn at 273 K. ³ , green signal represents CO_2 signal 1, orange signal represents CO_2 signal 2 and purple signal represents free CO_2	42
Figure 2.8. Experimental VT static ^{13}C SSNMR spectra of CO_2 at different $\text{CO}_2 + \text{D}_2\text{O}$ co-adsorbed loadings from 213 K to 373 K.	43
Figure 2.9. Experimental and simulated ^{3,4} VT ^{13}C static SSNMR spectra of CO_2 at 273 K with 0.25eq CO_2/Zn loading for $[\text{Zn}_2(\text{TRZ})_2(\text{NH}_2\text{-BDC})]$	44
Figure 2.10. a) C_2 hopping motion of CO_2 molecule of 180° rotation about the C_2 axis scheme, b) C_3 wobbling motion scheme of CO_2 , c) combined wobbling and hopping motions.	45
Figure 2.11. Experimental ^2H static SSNMR spectrum of D_2O at 373 K with 0.5eq $\text{D}_2\text{O}/\text{Zn}$ showing both D_2O and ND_2 , the narrow signal from D_2O ($C_Q = 37.8$ kHz) superimposes on the broad signal with low intensity from ND_2 ($C_Q = 101.5$ kHz) in the MOF.	47
Figure 2.12. Simulated pattern of a) ND_2 ($C_Q = 120$ kHz, $\eta_Q = 0.75$) and b) rigid D_2O ($C_Q = 216$ kHz, $\eta_Q = 0.1$) at 220K. ⁸	49
Figure 2.13. Experimental VT ^2H static SSNMR from 173 K to 373 K loaded with 0.25eq, 0.5eq and 1eq $\text{D}_2\text{O}/\text{Zn}$	50

Figure 2.14. Experimental VT ^2H static SSNMR spectra from 173 K to 373 K loaded with 0.25eq $\text{CO}_2 + 0.25\text{eq D}_2\text{O}$ and 0.25eq $\text{CO}_2 + 0.5\text{eq D}_2\text{O}$.	51
Figure 2.15. Experimental and simulated ^{3,4} VT ^2H static SSNMR spectra at 273 K with 0.25eq $\text{CO}_2 + 0.5\text{eq D}_2\text{O}$ loading.	53
Figure 2.16. a) π -flipflop motion of 180° rotation about the molecular C_2 axis of D_2O scheme. 4-site jumping motion scheme of D_2O b) C_4 axis pointing out of paper with 4-nitrogen rings in the paper, c) C_4 axis parallel to the paper with ring perpendicular to the paper, (d) top view of $[\text{Zn}_2(\text{TRZ})_2(\text{NH}_2\text{-BDC})]$ cages with nitrogen adsorption sites labeled as N1, (e) side view of $[\text{Zn}_2(\text{TRZ})_2(\text{NH}_2\text{-BDC})]$ cages with nitrogen adsorption sites labeled as N1.	54
Figure 2.17. Occupation of CO_2 molecules for pure CO_2 loadings.	57
Figure 2.18. Occupation of CO_2 molecules for pure D_2O loadings.	57
Figure 2.19. Occupation of CO_2 and D_2O molecules for co-adsorption loadings.	59
Figure 2.20 (a) ^1H - ^{13}C CP MAS SSNMR for 0.5eq CO_2 loaded $[\text{Zn}_2(\text{TRZ})_2(\text{NH}_2\text{-BDC})]$. (b) One-pulse ^{13}C MAS SSNMR for 0.5eq CO_2 loaded $[\text{Zn}_2(\text{TRZ})_2(\text{NH}_2\text{-BDC})]$. (c) Asymmetric carbons on the $[\text{Zn}_2(\text{TRZ})_2(\text{NH}_2\text{-BDC})]$ structure.	61
Figure 3.1. Powder X-ray diffraction patterns (PXRD) pattern of CALF-20 and the simulated as-made PXRD pattern was extracted based on the crystal structure provided in the reported literature ¹ .	68
Figure 3.2. Thermogravimetric analysis (TGA) curves of as-made (black curve) and activated (blue curve) CALF-20.	69
Figure 3.3. Side view of CALF-20 cage.	70

Figure 3.4. static ^{13}C SSNMR pattern of a) CO_2 with 0.25eq CO_2/Zn loading for CALF-20 at 173 K ($\Omega = 226$ ppm, $\kappa = 0.52$), b) rigid CO_2 ($\Omega = 335$ ppm, $\kappa = 1$).⁹ 71

Figure 3.5. Experimental VT static ^{13}C SSNMR spectra of adsorbed CO_2 at various CO_2 loadings and temperatures for CALF-20. 72

Figure 3.6. Experimental and simulated^{3,4} VT ^{13}C static SSNMR spectra of CO_2 from 173 K to 373 K with 0.25eq CO_2/Zn loading for CALF-20. 74

Figure 3.7. a) C_2 hopping motion of CO_2 molecule of 180° rotation about the C_2 axis scheme, b) C_3 wobbling motion scheme of CO_2 , c) C_2 hopping + C_3 wobbling motion in the CALF-20 framework with pure CO_2 loadings. Hydrogen adsorption sites labeled as H on the CALF-20 framework d) top view, e) side view. 78

Figure 3.8. Adsorption scenarios of different CO_2 loadings in CALF-20. 79

Figure 3.9. (a) ^1H - ^{13}C CP MAS SSNMR for 0.5eq CO_2 loaded CALF-20 framework. (b) One-pulse ^{13}C MAS SSNMR for 0.5eq CO_2 loaded CALF-20. (c) Asymmetric carbons on the CALF-20 framework structure. 81

List of Appendices

Figure A2.1. Experimental and simulated VT ¹³ C static SSNMR spectra at variable temperature with 0.25eqCO ₂ /Zn loading [Zn ₂ (TRZ) ₂ (NH ₂ -BDC)].	86
Figure A2.2. Experimental and simulated VT ¹³ C static SSNMR spectra at variable temperature with 0.5eqCO ₂ /Zn loading [Zn ₂ (TRZ) ₂ (NH ₂ -BDC)].	87
Figure A2.3. Experimental and simulated VT ¹³ C static SSNMR spectra at variable temperature with 0.75eqCO ₂ /Zn loading [Zn ₂ (TRZ) ₂ (NH ₂ -BDC)].	88
Figure A2.4. Experimental and simulated VT ¹³ C static SSNMR spectra at variable temperature with 0.25eqCO ₂ /Zn+0.25eqD ₂ O/Zn loading [Zn ₂ (TRZ) ₂ (NH ₂ -BDC)].	89
Figure A2.5. Experimental and simulated VT ¹³ C static SSNMR spectra at variable temperature with 0.25eqCO ₂ /Zn+0.5eqD ₂ O/Zn loading [Zn ₂ (TRZ) ₂ (NH ₂ -BDC)].	90
Figure A2.6. Experimental and simulated VT ¹³ C static SSNMR spectra at variable temperature with 0.25eqCO ₂ /Zn+1eqD ₂ O/Zn loading [Zn ₂ (TRZ) ₂ (NH ₂ -BDC)].	91
Figure A2.7. Experimental and simulated ^{1,2} VT ¹³ C static SSNMR spectra at variable temperature with 0.5eqCO ₂ /Zn+0.5eqD ₂ O/Zn loading [Zn ₂ (TRZ) ₂ (NH ₂ -BDC)].	92
Figure A2.8. Experimental and simulated ^{1,2} VT ¹³ C static SSNMR spectra at variable temperature with 0.5eqCO ₂ /Zn+1eqD ₂ O/Zn loading [Zn ₂ (TRZ) ₂ (NH ₂ -BDC)].	93
Figure A2.9. Experimental and simulated ^{1,2} VT ² H static SSNMR spectra at variable temperature for all coloaded samples of [Zn ₂ (TRZ) ₂ (NH ₂ -BDC)].	94

Table A2.1. VT ¹³C static SSNMR simulation parameters of CO₂ signal 1 for 0.25eq CO₂/Zn	95
.....	
Table A2.2. VT ¹³C static SSNMR simulation parameters of CO₂ signal 1 for 0.75eq CO₂/Zn	96
.....	
Table A2.3. VT ¹³C static SSNMR simulation parameters of CO₂ signal 1 for 0.25eq CO₂ + 0.25eq CO₂ + 0.5eq D₂O loading.	97
.....	
Table A2.4. VT ¹³C static SSNMR simulation parameters of CO₂ signal 1 for 0.25eq CO₂ + 0.25eq CO₂ + 1eq D₂O loading.	98
.....	
Table A2.5. VT ¹³C static SSNMR simulation parameters of CO₂ signal 1 for 0.25eq CO₂ + 0.5eq CO₂ + 0.5eq D₂O loading.	99
.....	
Table A2.6. VT ¹³C static SSNMR simulation parameters of CO₂ signal 1 for 0.25eq CO₂ + 0.5eq CO₂ + 1eq D₂O loading.	100
.....	
Figure A3.1. Experimental and simulated VT ¹³C static SSNMR spectra at variable temperature with 0.5eqCO₂/Zn loading for Calf-20.	101
.....	
Figure A3.2. Experimental and simulated VT ¹³C static SSNMR spectra at variable temperature with 0.75eqCO₂/Zn loading for Calf-20.	102
.....	

List of Abbreviations

BET	Brunauer, Emmett and Teller
BDC	1,4-benzenedicarboxylic acid
CP MAS	Cross Polarization Magic Angle Spinning
CSA	Chemical Shift Anisotropy
CT	Central Transition
DMF	N, N-dimethylformamide
EFG	Electric Field Gradient
MAS	Magic Angle Spinning
MOF	Metal-Organic Framework
NH ₂ -BDC	2-amino-1,4-benzenedicarboxylic acid
NMR	Nuclear Magnetic Resonance
PAS	Principle Axis System
ppm	Parts Per Million
PXRD	Powder X-ray Diffraction
SBU	Secondary Building Units
SSNMR	Solid-State Nuclear Magnetic Resonance
ST	Satellite transition

TGA	Thermogravimetric analysis
TRZ	1,2,4-triazolate
VT	Variable Temperature
XRD	X-ray Diffraction
ZTP-3	$[\text{Zn}_2(\text{TRZ})_2(\text{NH}_2\text{-BDC})]$

Chapter 1. General introduction

1.1. Metal-organic frameworks (MOFs)

Metal-organic frameworks (MOFs) are a class of porous, crystalline materials emerging since the 1990s.¹ These 3D polymeric frameworks were first designed and synthesized by B.F. Hoskins and R. Robson in 1990 with the purpose of catalytic applications.¹ In 1995, this type of material was first given the name “metal-organic frameworks” in O. M. Yaghi’s work on binding and removal of guest molecules in MOFs.² MOFs are comprised of metal containing units or secondary building units (SBUs) with organic linkers through coordination bonds as depicted in **Figure 1.1**. The specific catalytic, magnetic, electrical, optical, and structural properties can arise from enormous combinations of metals and organic linkers, which allows flexible functional optimization of the MOFs for an extensive range of research fields. Therefore, MOFs with targeted properties including large pore size, large surface area, and high framework stability can be modified and synthesized.^{3,4} This flexible tunability distinguishes MOFs from traditional porous materials such as zeolite and activated carbon.⁵ MOFs are promising candidates for many applications such as energy conversion,⁶ drug delivery,⁷ heterogenous catalysis,⁸ water purification,⁹ and gas storage and separation.^{10,11}

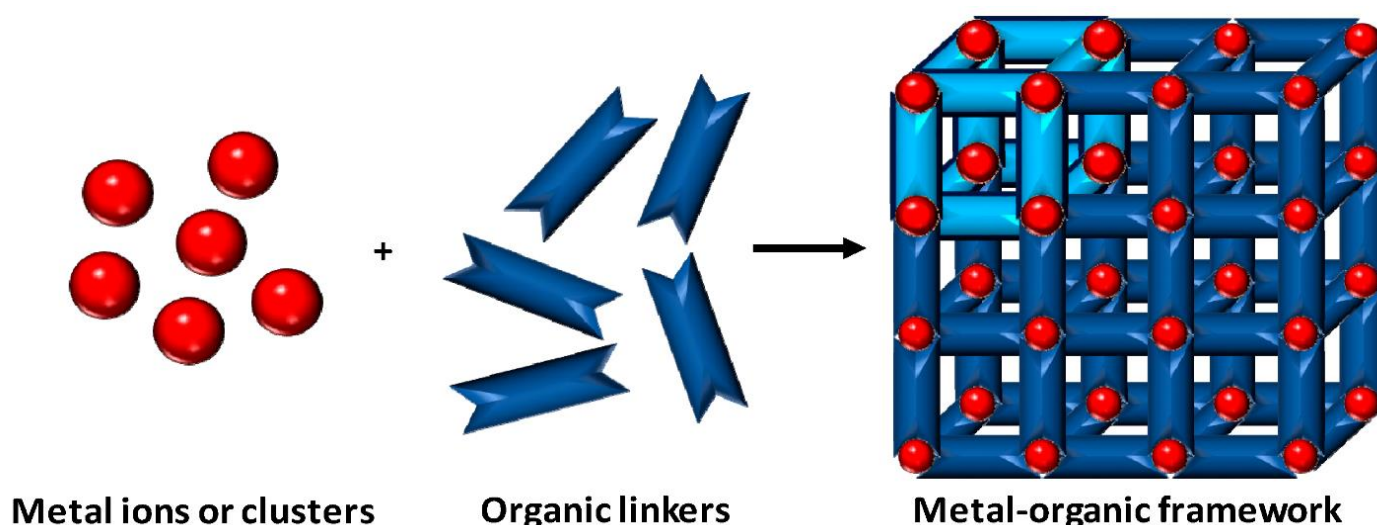


Figure 1.1. schematic diagram of composition of MOFs.¹²

1.1.1. MOFs as gas storage materials

MOFs could be used as an ideal gas storage material due to its nature of high porosity and tunability. By changing the functional ligand, properties such as higher selectivity and affinity of certain gases, larger pore size and surface area could be attained, which greatly enhance the gas adsorption capacity compared to other porous materials.

Despite of having higher tunability, gas adsorption in MOFs follows the same mechanisms as zeolites and activated carbon: 1) physisorption ($\Delta H_{\text{ads}} \sim 5\text{--}50 \text{ kJ mol}^{-1}$), 2) chemisorption ($\Delta H_{\text{ads}} > 50 \text{ kJ mol}^{-1}$).¹⁴ Physisorption refers to physical adsorption to the surface usually due to surface characteristics. As indicated in Figure 1.2, adsorption due to electrostatic attraction, van der Waals forces, and diffusion are some of the examples of physisorption.¹⁵ Chemisorption refers to adsorption via chemical bonding between the adsorbent surface and adsorbate. Since the enthalpy of chemisorption is significantly higher, regeneration of the adsorbent would be difficult, resulting in a decrease in reusability, which is less competitive against MOFs using physisorption.¹⁵ Therefore in this thesis, physisorption MOFs were selected.

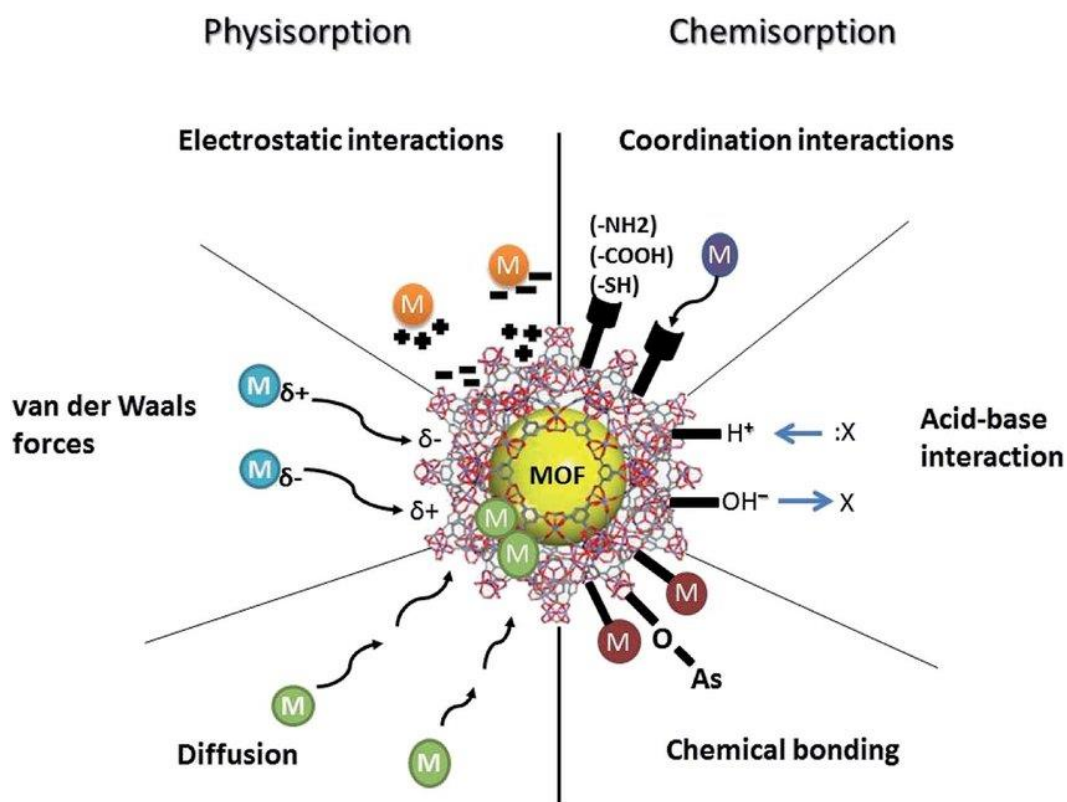
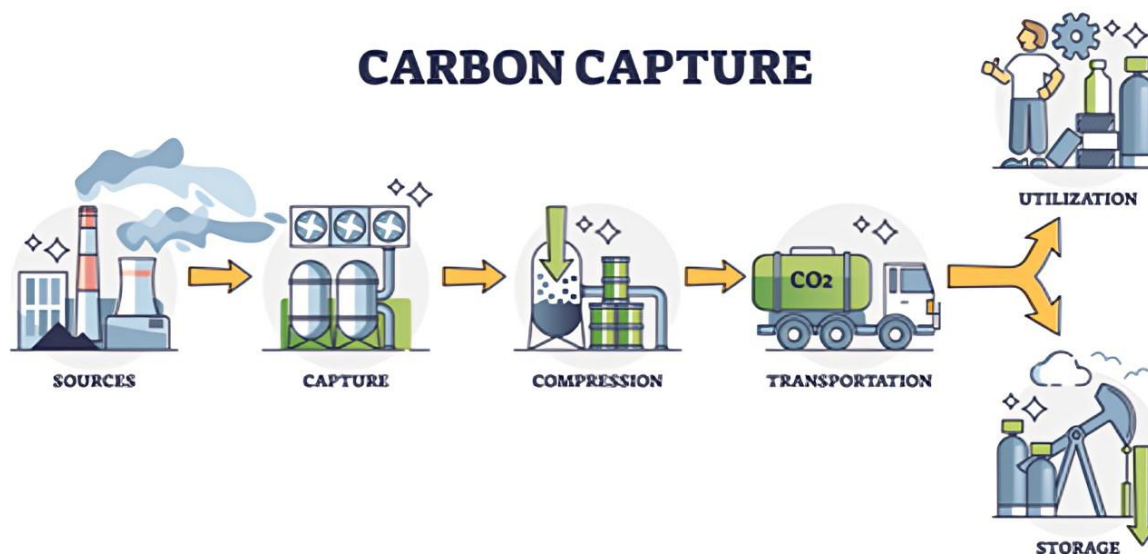


Figure 1.2. Schematic diagram of different gas adsorption mechanisms in MOFs.¹⁵

1.1.2. Carbon dioxide (CO₂) capture and storage



Climate change has been an escalating global issue since the last few decades with the fact that anthropogenic carbon dioxide being the main contributor to global warming and other environmental issues.¹² Hence, mitigation techniques to reduce anthropogenic CO₂ emissions are of great significance. Carbon capture and storage (CCS) is one of the promising technologies to control CO₂ concentration in the atmosphere.^{13,14} CO₂ gas is first captured from sources of generation (e.g. power plants), compressed into a supercritical fluid, and then separated during the CCS process.¹³ **Figure 1.3** below shows a demonstration of a general CCS process.

Figure 1.3. Schematic diagram for carbon capturing.¹⁶

MOFs can be optimized as outstanding materials for gas storage and separation due to their high porosity and flexibility in metal centers and ligand choices.^{15,16} As a result, research on CO₂ storage, adsorption, and separation has drawn much attention.¹⁷ Pore size, functionality, and CO₂ selectivity against other gases could be optimized through changing the functional group of the selected ligand to maximize the CO₂ adsorption capacity of MOFs while maintaining structural stability.^{16,18} Many MOFs exhibit excellent carbon dioxide selectivity compared to hydrocarbons and nitrogen, which could be viable options for pre-combustion and post-combustion carbon

dioxide capturing.^{18,19} However, water is ubiquitous in the atmosphere and the fuel gas generated in the power plants, CO₂ selectivity and adsorption capacities of some MOFs could be negatively impacted in the presence of water, which would be a drawback of its application.²⁰

1.1.3. Water effects on CO₂ adsorption in MOFs

A wide range of effects could be observed on different MOFs when water is present.²⁰ In some MOFs, guest molecules adsorption and framework stability could be drastically reduced, and even structural dissociation could be promoted with the introduction of water.²¹ As an example, in Yu's work, the CO₂ isotherms for MOF-74 indicated significant decreases in CO₂ uptake at higher hydration levels. While in some other MOFs, water can have a positive effect on carbon dioxide adsorption. For example, according to J. Yu's work on post-combustion CO₂ adsorption MOF HKUST-1, the carbon dioxide adsorption was found to be enhanced with an increase in hydration level.²¹ Pore size and guest molecules binding energy with the framework were found to be significant regarding to the adsorption capacity. In HKUST-1, the increase in CO₂ binding energy with the framework through increased coulombic interaction between CO₂ and water results in the increased CO₂ adsorption capacity.²¹ Thus, understanding the impact of water on MOFs is crucial for improving CO₂ adsorption performance. Furthermore, Open Metal sites could also possess the trait of reduced CO₂ adsorption under humid conditions.⁴⁹ Therefore in this work, MOFs without open metal sites were chosen. **Table 1.1** below shows an example of CO₂ adsorption capacity decreasing when water was present for MIL-120, a MOF without open metal sites. In **Table 1.1**, q_{CO_2} refers to the amount of CO₂ uptake, and SD refers to the standard deviation.

Table 1.1. CO₂ uptake of MIL-120 under dry and wet flue gas⁴⁸

Pretreatment	Adsorbate gas	q_{CO_2} (mmol/g)	Average q_{CO_2} (mmol/g)	SD q_{CO_2} (mmol/g)
Activation 15 min	dry 15%CO ₂ :85%N ₂	1.224	1.215	0.016
		1.228		
		1.193 ^a		
Activation 4.5 h	humid 15%CO ₂ :85%N ₂	1.049	1.118	0.06
		1.191 ^b		
		1.113		

1.1.4. pillar-layered MOFs

In pillar-layered MOFs, the 3D framework structure was formed first by connecting 2D layers with linker ligands as pillars (**Figure 1.4**). The pore size and functionalities can be precisely modified by connecting the same 2D layers with different pillars.¹⁸ This type of MOFs is also found to retain higher structural stability than the non-pillar-layered ones.²¹ Permanent porosity has been a crucial concern in MOF assembly since it directly affects its efficacy in gas adsorption. Water can result in degradation of the framework structure that greatly decrease the performance of MOF's adsorption capability. By simply optimizing the pillars, MOFs more suitable for practical applications can be utilized, the porosity of MOF could even be pertained under acidic, basic, high temperature and humid conditions.⁵⁰

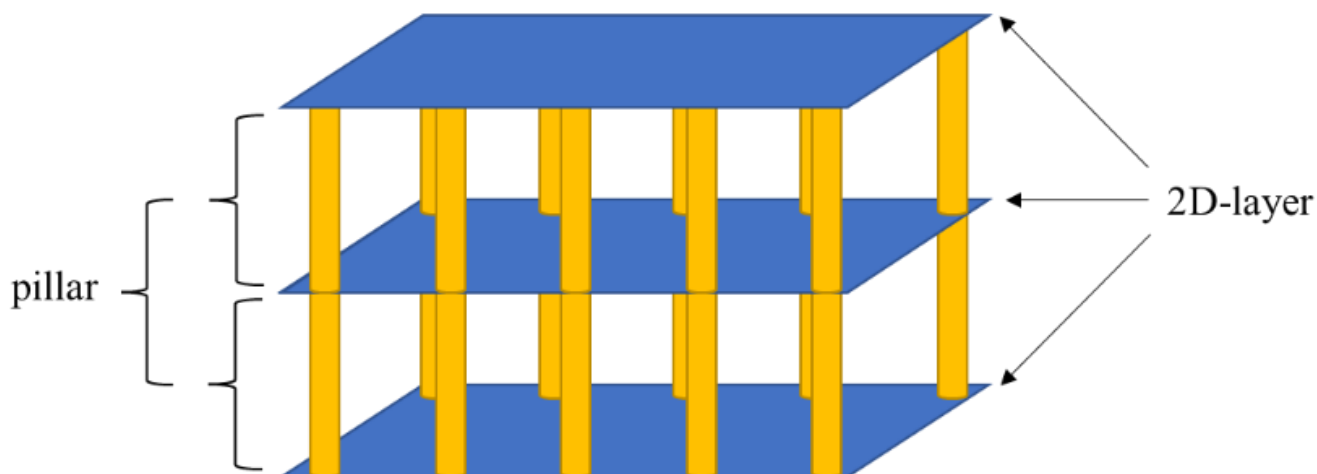


Figure 1.4. Simplified structure of pillar layered MOFs

1.1.5. MOFs studied in this thesis

$[Zn_2(TRZ)_2(NH_2-BDC)]$. In Q. G. Zhai's work, seven Zn-triazolate dicarboxylate frameworks were found to exhibit excellent CO_2 selectivity against CH_4 and N_2 with high CO_2 adsorption capability, the MOFs were constructed by connecting dicarboxylate ligands as pillars with a 2D layer formed by zinc ions and 1,2,4 triazolate (**Figure 1.5, 1.6**).¹⁸ Each of the zinc in the structure was 5 coordinated, connected with 3 nitrogens from 3 different triazole ligands and 2 oxygens from the same dicarboxylate group (**Figure 1.7**). The zinc triazolate dicarboxylate pillar-layered MOFs show potential application of CO_2 storage and separation, therefore in this work,

[Zn₂(TRZ)₂(NH₂-BDC)] (abbreviated as ZTP-3 in this work) was selected to investigate the CO₂ adsorption behavior in humid environment. 2-amino-1,4-benzenedicarboxylic acid (NH₂-BDC) was used as the pillar in ZTP-3, in which its amino functional groups enhance CO₂ affinity. The CO₂ adsorption capacity was found to be 3.08 mmol/g at 273 K under 1.01 bar.¹⁸ ZTP-3 is a pillar layered tetragonal MOF with a pillar length of 10.8 Å, with large pore size and good thermal stability.

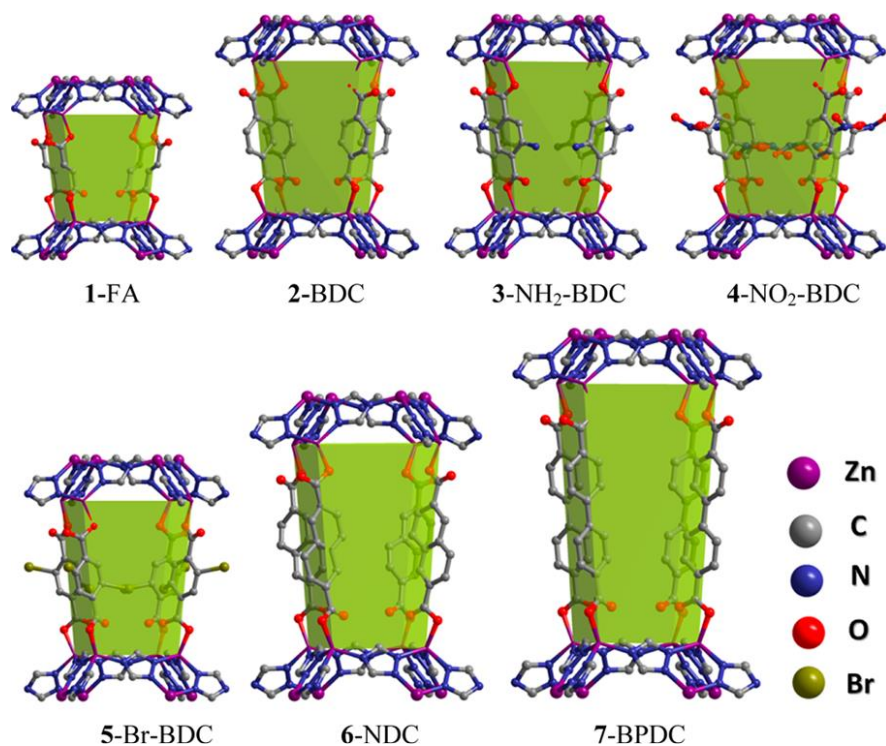


Figure 1.5. Seven Zn-triazolate dicarboxylate MOFs from Zhai's work.¹⁸

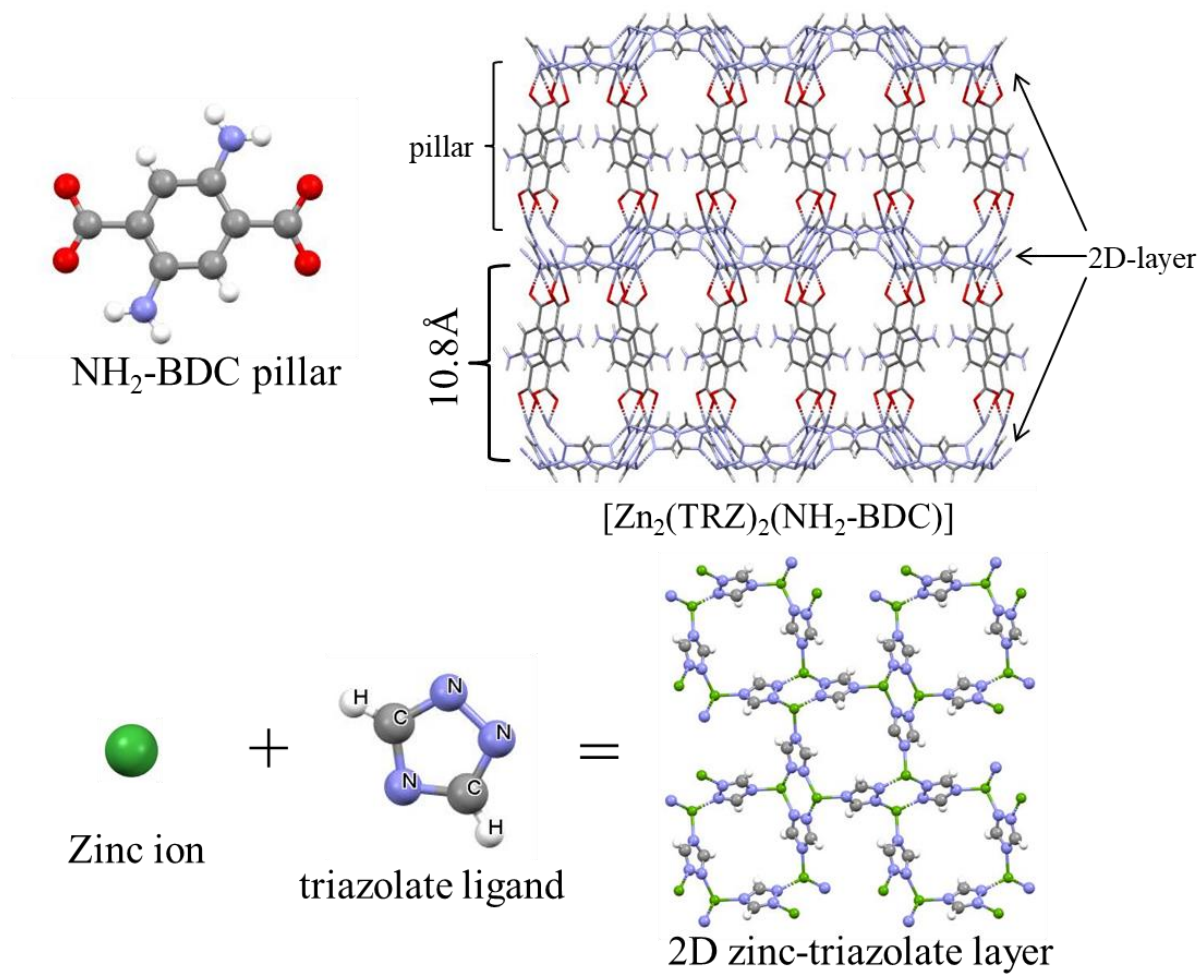


Figure 1.6. Components of ZTP-3¹⁸

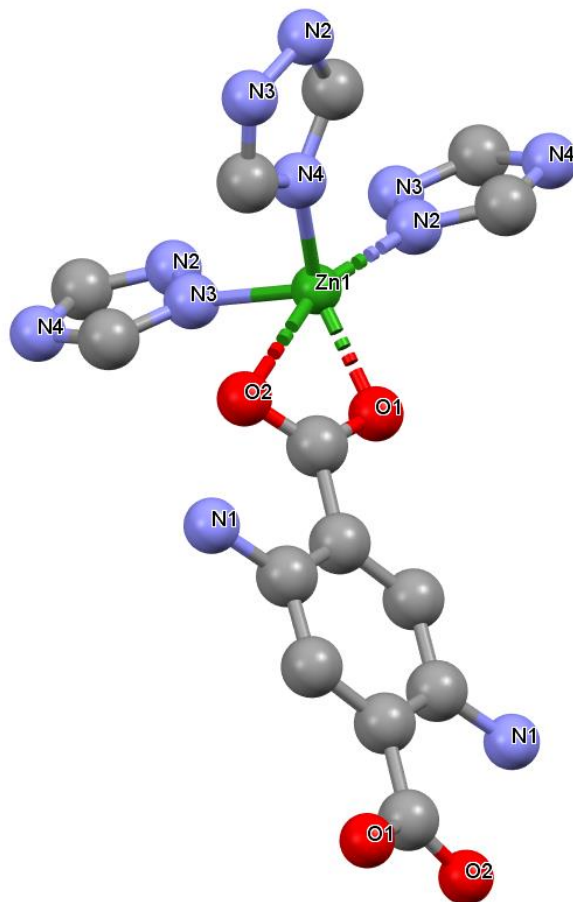


Figure 1.7. Coordination on zinc in ZTP-3¹⁸

CALF-20. CALF-20 is a new MOF developed by Jian-Bin Lin et al. from University of Calgary. It is a monoclinic pillar layered MOF consisting of layers of 1,2,4-triazolate bridged zinc (II) ions connected by oxalate ligands (**Figure 1.8**). Each of the zinc in the structure was 5 coordinated, connected with 3 nitrogens from 3 different triazole ligands and 2 oxygens from the same oxalate ligand (**Figure 1.9**). The CO₂ adsorption capacity was found to be 4.07 mmol at 293 K under 1.2 bar.²⁰ This framework was selected due to its exceptional properties of high CO₂ adsorption capacity and selectivity, large scale production capability, good thermal stability and its resistance against water.²⁰

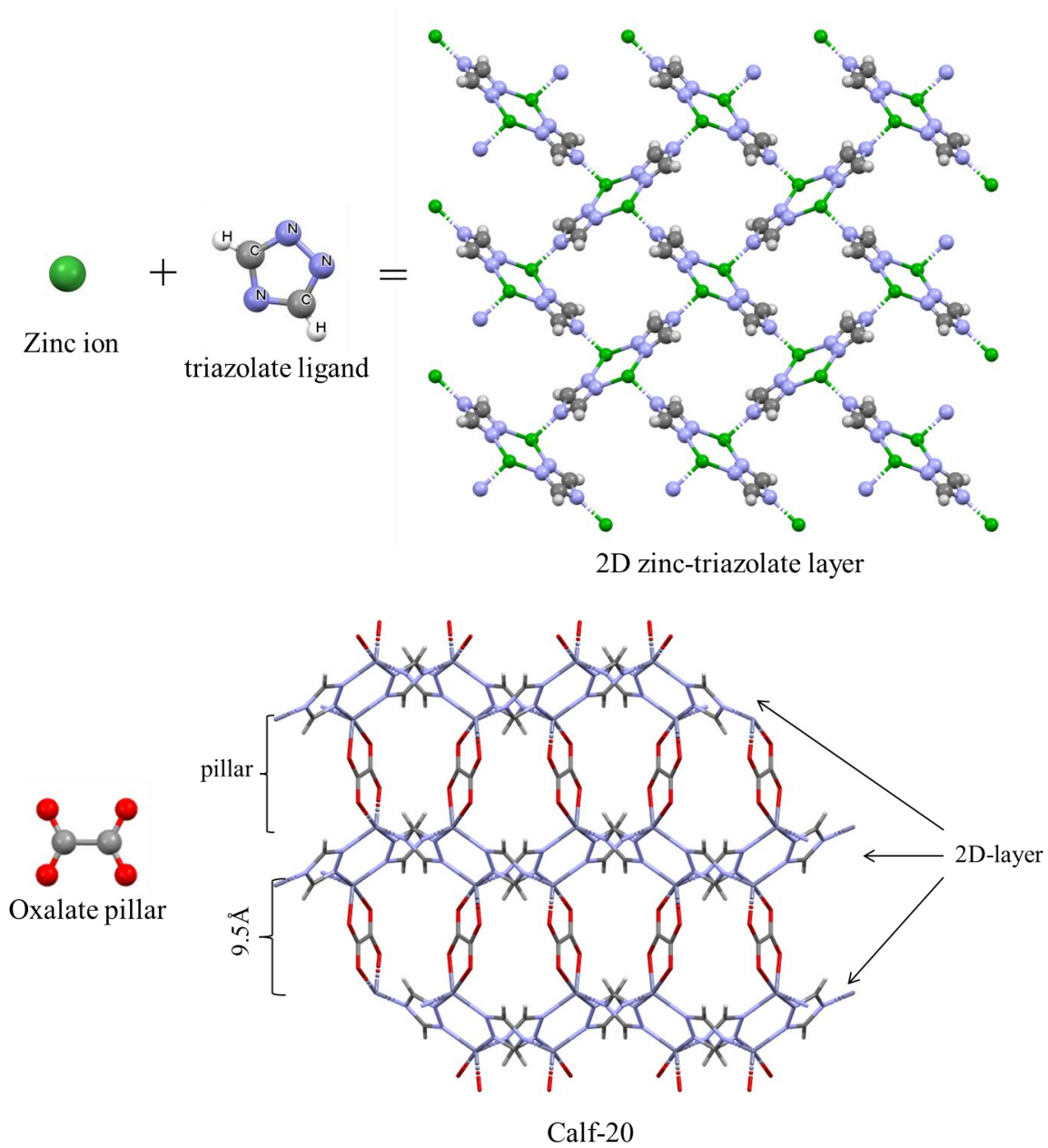


Figure 1.8. Components of Calf-20²⁰

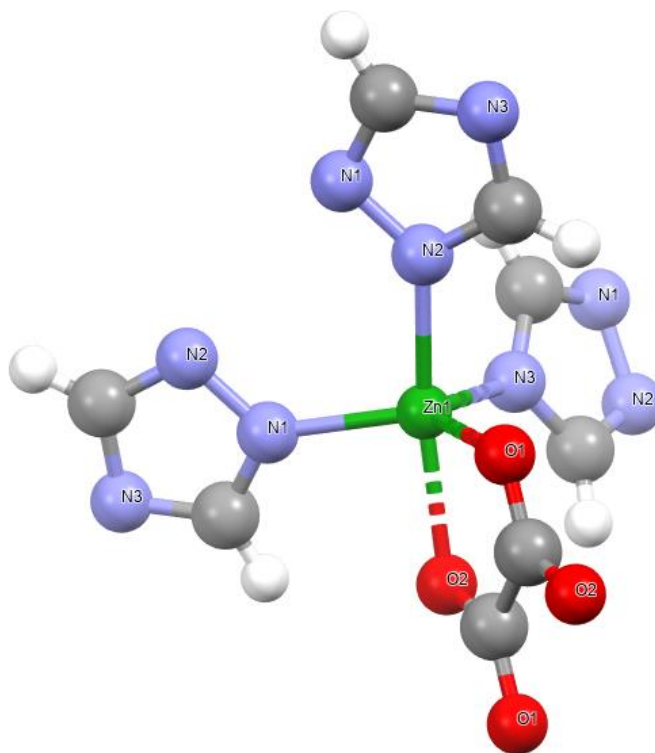


Figure 1.9. Coordination on zinc in CalF-20²⁰

1.2. Characterization of MOFs

Characterization of MOFs is essential to understand the properties of the system. Powder X-ray diffraction (PXRD), thermogravimetric analysis (TGA), Brunauer, Emmett and Teller (BET) are widely used as characterization techniques for MOFs. Through characterization, we are able to obtain valuable information such as crystal structure, phase purity, thermal stability, surface area, reproducibility and other properties of MOFs.

1.2.1. X-ray Crystallography

Single-crystal XRD and PXRD are both widely used for characterizing crystal structures. Single-crystal XRD is a powerful technique with high precision for crystal structure elucidation in three-dimensional space. However, single-crystal XRD could be challenging due to its requirement for well ordered, large high qualities crystals. Synthesis of well-ordered single MOF crystal can be difficult. While PXRD requires only a small amount of sample and could be done on a wide range

of variety of materials including crystalline powder, nanoparticles, and amorphous materials. PXRD allows us to confirm the phase purity and identify the structure of the MOF.

Bragg's law is a fundamental concept in comprehending the crystal structures in X-ray crystallography and structural analysis. By directing X-rays with a fixed wavelength onto crystalline materials at specific angles of incidence, atomic-level interactions are generated with the crystals' lattice planes. The resulting effect produces intense reflected X-rays due to constructive interference, whereby the wavelengths of the scattered X-rays reinforce each other.¹⁹ The scattered X-rays need their path differences to reflect integer multiples of the wavelength to produce constructive interference. Consequently, the crystal's diffracted X-ray beam exits at precisely the same angle as the incident beam.

To illustrate this concept, consider a crystal with crystal lattice planar distances represented by 'd.' When the travel path length difference between X-ray paths, such as ABC and A'B'C' (**Figure 1.10**), equals an integer multiple of the wavelength, constructive interference occurs. This specific wavelength, crystal lattice planar spacing, and angle of incidence (Θ) form a unique combination for which constructive interference occurs. For X-rays at a fixed wavelength, each rational atomic plane within the crystal will refract at a distinct angle.¹⁹

The general expression capturing the relationship between the wavelength of incident X-rays (λ), the angle of incidence (Θ), and the spacing between the crystal lattice planes of atoms (d) is known as Bragg's Law and can be represented as:

$$n\lambda = 2d \sin\Theta$$

Here, 'n' signifies the order of reflection, which is an integer value. Bragg's Law plays a crucial role in the identification and characterization of crystalline materials, which is especially useful in X-ray diffraction (XRD). In XRD, the known wavelength of the incident X-ray is utilized, and measurements are taken of the incident angle (Θ) at which constructive interference occurs. By solving Bragg's Equation, the interplanar spacing (d-spacing) between the crystal lattice planes of atoms responsible for the constructive interference can be determined.

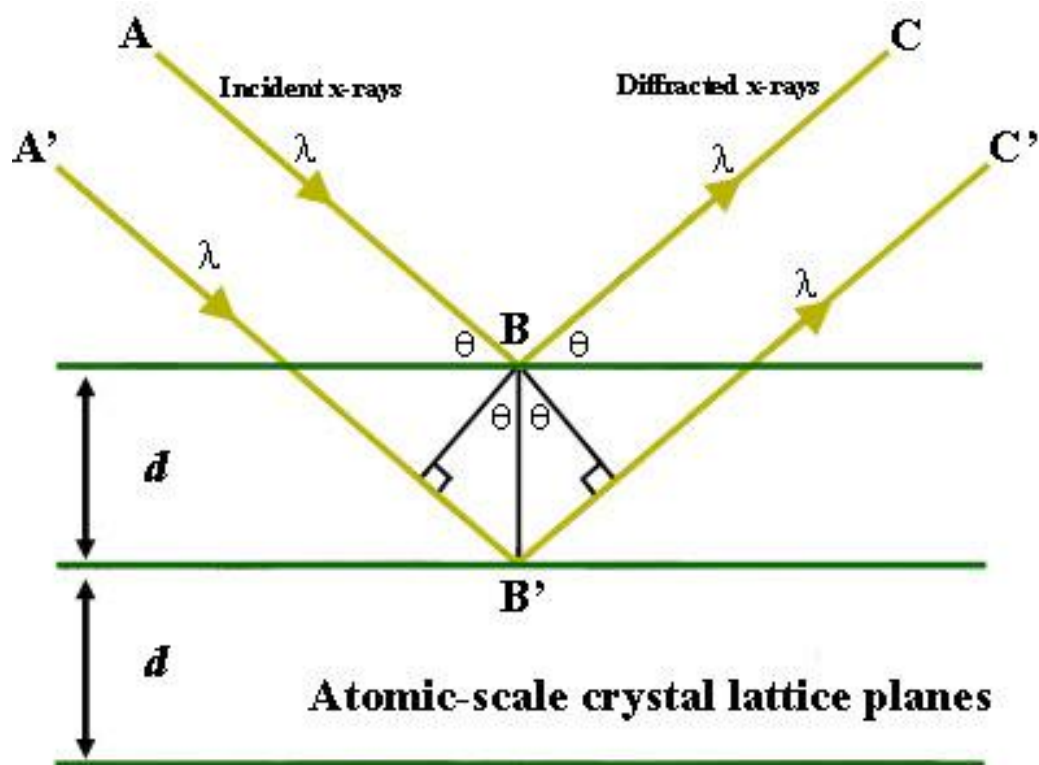


Figure 1.10. Schematic diagram for X-ray diffraction¹⁹

1.2.2. Thermogravimetric analysis (TGA)

Thermogravimetric analysis measures the weight loss of the sample as a function of temperature or time under controlled and stable atmosphere. It provides information on thermal stability and decomposition kinetics of the sample. Activation of a MOF could also be confirmed if weight loss of solvents is not observed at their boiling points.

1.3. Solid-state NMR (SSNMR)

Nuclear Magnetic resonance spectroscopy (NMR) was first discovered in 1928 by Isidor Isaac Rabi,⁴⁰ who was later awarded the Nobel Prize in 1944 for his discovery.⁴⁰ Solid-state NMR has been employed extensively as a powerful technique to characterize MOFs to an atomic level.⁴¹ SSNMR allows investigation of MOFs' structure, mapping of functional groups, and guest molecule behavior within the structure.⁴¹

NMR is governed by 2 fundamental properties: 1) nuclear spins (I) and the applied external magnetic field (B_0). The nuclear spin quantum number I is associated with the nuclear spin angular momentum of the target nuclei, which is an intrinsic property, while the applied magnetic field B_0 is an extrinsic property. To be NMR active, the isotope with a non-zero nuclear spin quantum number I is required. By counting the number of protons and neutrons of the nucleus, the spin quantum number I can be predicted. Odd number in either protons or neutrons results in an NMR-active isotope, in contrast, if the protons and neutrons of the isotope are both even, the nucleus is NMR-inactive.

Table 1.1 Spin quantum number I prediction based on number of protons and neutrons of the nucleus.

Number of protons	Number of neutrons	Spin quantum number
Even	Even	Zero
Even	Odd	Half-integer (e.g. 1/2, 3/2)
Odd	Even	Half-integer (e.g. 1/2, 3/2)
Odd	Odd	Integer (e.g. 1)

1.3.1. NMR interactions

In NMR spectroscopy, various interactions between nuclear spins and external magnetic fields play a crucial role in determining the information that can be obtained from NMR experiments. These interactions provide valuable insights into the structure, motions, and chemical environment of molecules and materials. Typical nuclear spin interactions can be summarized in the formula $\hat{H}_{\text{NMR}} = \hat{H}_Z + \hat{H}_{\text{rf}} + \hat{H}_{\text{CS}} + \hat{H}_D + \hat{H}_J + \hat{H}_Q$, which corresponds to Zeeman interaction, radio frequency interaction, dipolar coupling interaction, J-coupling interaction and quadrupolar interaction, which have different magnitudes listed in **Table 1.2**.⁴²

Table 1.2. Magnitudes of typical NMR interactions

Interactions	Magnitude (Hz)
Zeeman	10^7 - 10^9
Magnetic shielding	10^3 - 10^5
Dipolar coupling	10^3 - 10^4
J-coupling	0 - 10^3
Quadrupolar	10^3 - 10^7

1.3.2. Zeeman interactions

The Zeeman interaction arises from the interaction of a nuclear magnetic moments with an external magnetic field (B_0). It results in the separation of nuclear energy levels into different spin states, leading to the observed NMR signal. Zeeman interaction is known as the strongest interaction among all interactions. For a nucleus with spin I , it has $2I+1$ possible energy levels. In the absence of an applied external magnetic field (B_0), the energy levels are degenerate.⁴² However, when an external magnetic field is applied to the nucleus, all the $2I+1$ energy levels will no longer be degenerate, they will split into discrete energy levels which can be distinguished by magnetic quantum number m_I ($m_I = -I, -I+1, -I+2, \dots, I-2, I-1, I$),⁴² which can be described with the equation: $\Delta E = \gamma \hbar B_0 = \hbar \omega_0$.⁴² Where ΔE refers to the energy difference between the separated energy levels upon the presence of the external magnetic field B_0 , proportional to the Larmor frequency ω_0 describing the rate of transition between the levels and the gyromagnetic ratio γ , and \hbar is the Plank's constant (h) divided by 2π .⁴²

Figure 1.11 serves to provide a visual demonstration of the Zeeman energy splitting from a nucleus with $I=1/2$. The stronger the applied external magnetic field, the stronger the interaction, resulting in a stronger NMR signal.

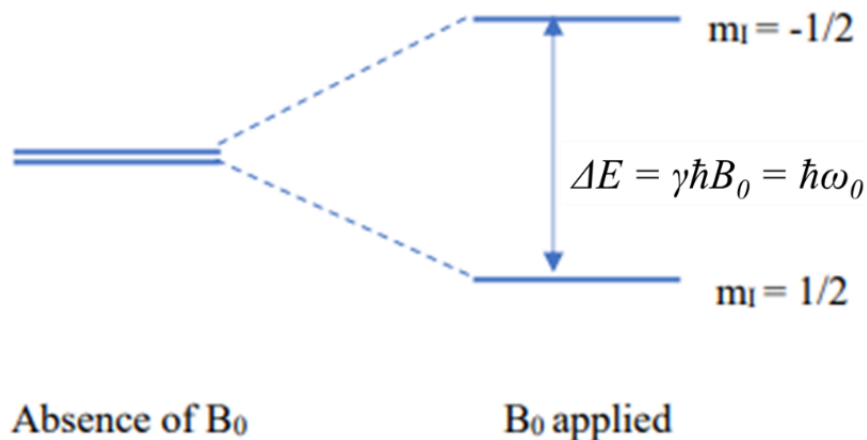


Figure 1.11. Zeeman interaction when $I=1/2$

1.3.3. Chemical shielding interaction

Chemical shield interaction arises from the additional motion of the electrons surrounding the nucleus induced by external magnetic field.

0 With the presence of an external magnetic field B_0 , a small secondary magnetic field generated by the additional motion shields or deshields the nucleus, which creates a small deviation in frequency. This frequency deviation is known as the chemical shielding interaction. Additionally, the term chemical shielding refers to the shift in NMR frequency induced by the shielding interaction in an NMR spectrum. The chemical shielding Hamiltonian operator \hat{H}_{CS} can be described using the equation:⁴³

$$\hat{H}_{CS} = -\gamma \hbar \hat{\sigma} B_0$$

Where $\hat{\sigma}$ refers to the spin operator, σ is a second rank chemical shielding tensor, which can be interpreted by a 3x3 matrix:⁴⁴

$$\sigma = \begin{pmatrix} \sigma_{xx} & \sigma_{xy} & \sigma_{xz} \\ \sigma_{yx} & \sigma_{yy} & \sigma_{yz} \\ \sigma_{zx} & \sigma_{zy} & \sigma_{zz} \end{pmatrix}$$

Since the NMR pattern is only contributed by the symmetric shielding tensor components in the matrix, 3 chemical shielding tensor components (σ_{11} , σ_{22} , and σ_{33}) corresponding to the principal axis system (PAS) can be defined:⁴³

$$\sigma^{PAS} = \begin{pmatrix} \sigma_{11} & 0 & 0 \\ 0 & \sigma_{22} & 0 \\ 0 & 0 & \sigma_{33} \end{pmatrix}$$

The degree of chemical shielding in all three dimensions can be described by the 3 components and can be arranged as follows: $\sigma_{11} \leq \sigma_{22} \leq \sigma_{33}$ (**Figure 1.12**). σ_{11} is the least shielded and σ_{33} is the most shielded component. The 3 principal components can be further converted using $\delta = \frac{\sigma_{ref} - \sigma}{\sigma_{ref}} \approx (\sigma_{ref} - \sigma)$ to obtain the 3 chemical shifts δ_{11} , δ_{22} and δ_{33} . In the NMR spectrum, δ_{11} appears to have the highest frequency positioning on the left, while δ_{33} positions at the lowest frequency on the right, which is shown in **Figure 1.13**.

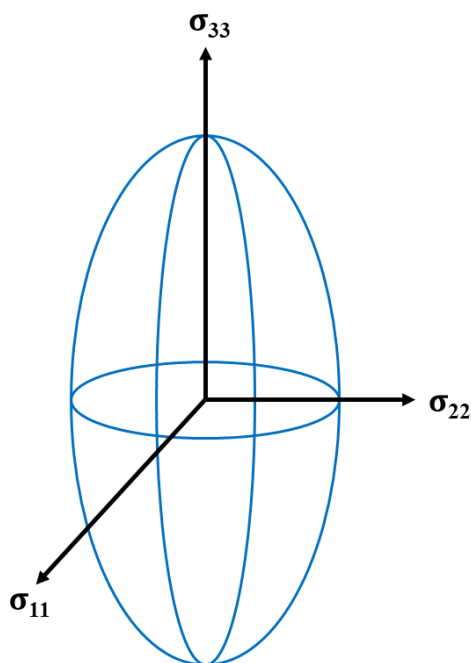


Figure 1.12. Chemical shielding components in 3 dimensions.

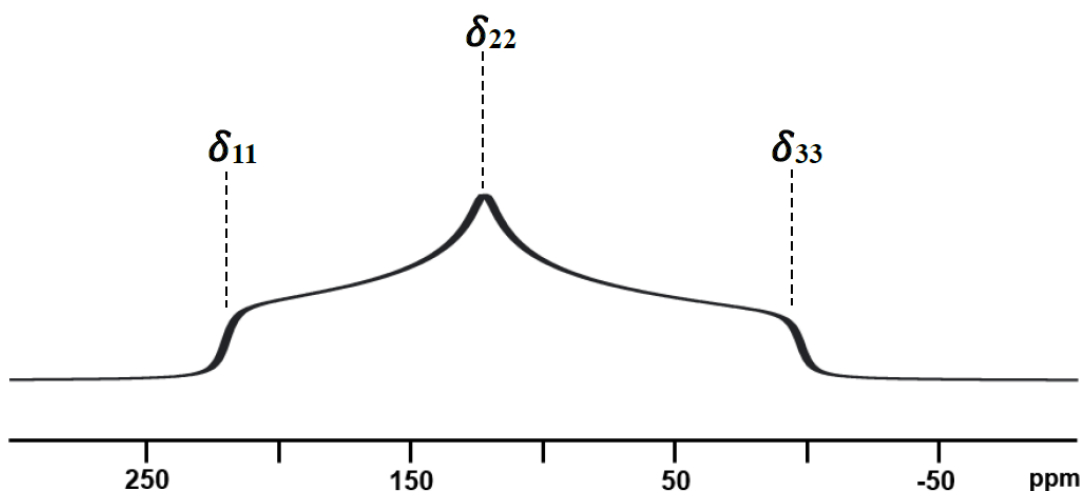


Figure 1.13. SSNMR powder pattern showing 3 chemical shielding components.

1.3.4. Dipolar interaction

The dipolar interaction represents a fundamental phenomenon in NMR spectroscopy, which results from the coupling between 2 magnetic dipoles. The dipolar interaction involves the interaction of 2 nuclear spins I and S. The strength of the dipolar interaction can be described by the dipolar coupling constant D. Dipolar coupling constant is a parameter intimately linked to the magnetic properties of the nuclei involved and the distance (r) separating them. The expression for D, influenced by factors like the permeability of vacuum (μ_0), the gyromagnetic ratios (γ_I and γ_S) of the spins I and S, and fundamental constants such as Planck's constant (h) and 2π , embodies the intricate relationship that characterizes this interaction:⁴⁵

$$D = \frac{\mu_0}{4\pi} \frac{\gamma_I \gamma_S}{r^3} \frac{h}{2\pi}$$

In this context, the modified frequency, which governs the orientation-dependent behavior of nuclear spins under the dipolar interaction, can be calculated as:⁴⁵

$$\nu = \nu_0 \pm 1/2 D(1 - 3 \cos^2 \alpha)$$

Where ν_0 represents the Larmor frequency, and α refers to the angle between the inter-nuclear vector and the direction of the external magnetic field (B_0).

In NMR spectra for an isolated I-S spin pair, the dipolar interaction is displayed by the characteristic pattern of a Pake doublet. Two mirrored powder patterns identified by "horns" and "feet," which represent the opposing perturbations to the Zeeman interaction, make up the Pake doublet. Two "horns" appear when the I-S vector is perpendicular to the external magnetic field B_0 , and "feet" appear when the I-S vector is parallel to B_0 . Additionally, the frequency gaps between these "horns" equal to $1D$ for heteronuclear spin pair, and $0.75D$ for homonuclear spin pair respectively. The "feet" equal to twice the length of the "horns", which is shown in **Figure 1.14**.

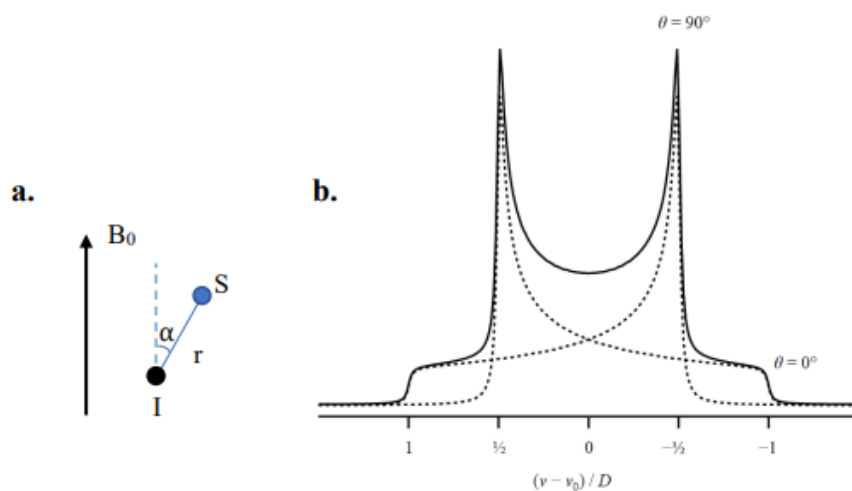


Figure 1.14. Dipolar interaction

1.3.5. J-coupling interaction

When compared to the dipolar interaction, the J-coupling interaction is characterized by a relatively weaker magnitude and originates from the chemical bonds between nuclei.⁴² The nature of these interactions leads to this difference in strength. The J-coupling interaction has much less effect on SSNMR spectra because of its relatively weak strength, particularly when broad line-shapes are present due to other interactions. J-coupling interactions, on the other hand, are more frequently seen in solution NMR when line broadening along with other interactions, such as quadrupolar interactions, are not present.

1.3.6. Quadrupolar interaction

Electric quadrupole moment arises from a non-spherical nuclear charge distribution, which results from quadrupolar nucleus with a spin quantum number larger than $\frac{1}{2}$. A quadrupolar interaction occurs when the change in electric field caused by local distribution of nuclear and electronic charges, which is the electric field gradient (EFG), interacts with the electric quadrupole moment. The EFG is described by a second-rank EFG tensor in the principal axis system (PAS), which has 3 non-zero components denoted by V_{xx} , V_{yy} , and V_{zz} , where $V_{zz} > V_{yy} > V_{xx}$.^{46,47} This tensor characterizes the local electric field's directional characteristics and hence, the behavior of the quadrupolar interaction.⁴⁶

Two crucial parameters are used to describe the quadrupolar interaction: 1) quadrupolar coupling constant (C_Q) and 2) asymmetric parameter (η_Q), which can be calculated using the equation below:

47

$$C_Q = \frac{eQV_{zz}}{h}$$

$$\eta_Q = \frac{V_{xx} - V_{yy}}{V_{zz}}$$

Q is the nuclear quadrupole moment. C_Q refers to the magnitude of the quadrupolar interaction and describes the degree of spherical symmetry of the electronic environment of the nucleus. The higher the C_Q , the stronger the quadrupolar interaction, the lower the degree of spherical symmetry. On the other hand, η_Q describes the axial symmetry of the EFG tensor and has a range of 0 to 1. Higher axial symmetry is indicated by lower η_Q values.

For a nuclear system involving only Zeeman interactions, $2I+1$ energy levels with same transitional energy are formed. Upon the perturbation of quadrupolar interactions, these energy levels shift according to the orientation of the chemical structure containing the target nucleus, which can be calculated by considering the first and second order quadrupolar interactions.⁴⁵

Figure 1.15. demonstrates the perturbation of the first and second order quadrupolar interactions on the Zeeman energy levels of the nucleus with spin quantum number of half-integer $I=3/2$.⁴⁵ Upon the influence of first-order quadrupolar interactions, all energy levels were shifted while the energy difference of the nuclear central transition (CT) between $m_I=-1/2$ and $m_I=+1/2$ remains the

same.⁴⁵ The other 2 energy levels transitions (satellite transitions (ST)), are greatly shifted, resulting in broadening of the spectral pattern. Since the CT is not affected by first-order quadrupolar interactions, it has a higher signal intensity compared to the ST, making the detection of CT more favorable for SSNMR experiments of half-integer nucleus.^{45,48} While upon the perturbation of second-order quadrupolar interaction, the CT also is affected.⁴⁶

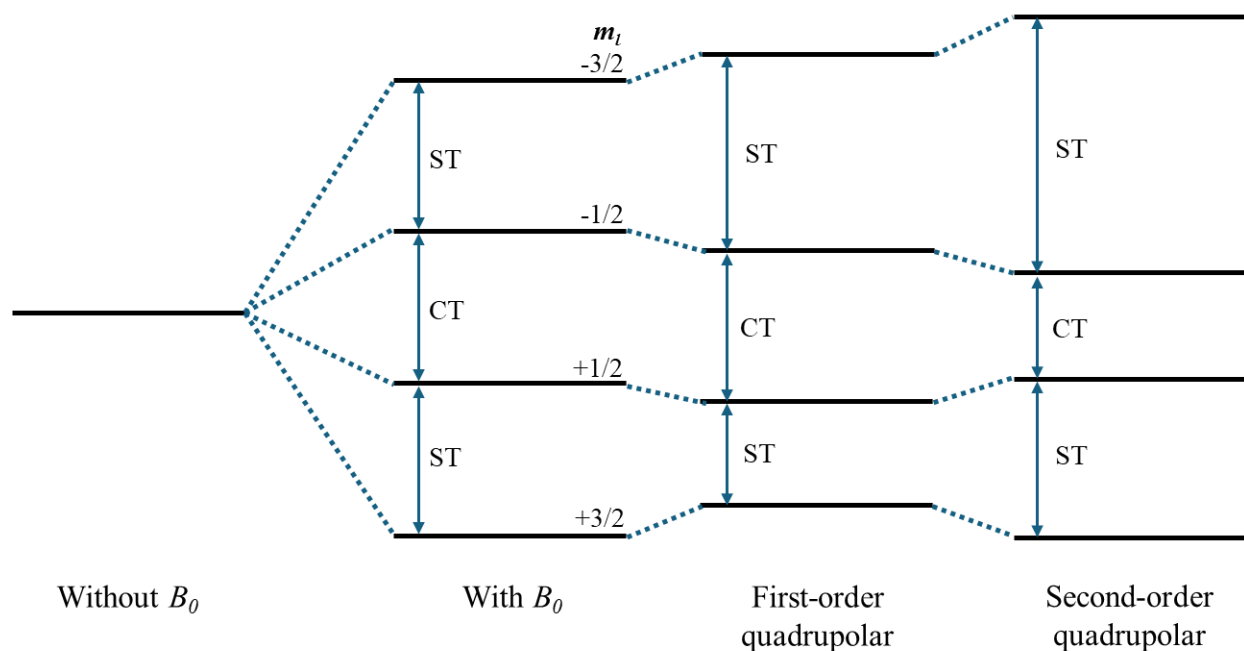


Figure 1.15. Perturbation of first and second order interaction on Zeeman energy levels of nucleus with half-integer spin quantum number $I=3/2$.

For nucleus with an integer spin quantum number, even number of energy transitions are generated by the Zeeman interactions. For example, when $I=1$, 2 energy transitions are generated. The SSNMR powder pattern will only be greatly influenced by the first order quadrupolar interactions, which are shown in **Figure 1.16**. As depicted in Figure 1.17 (b), the pake doublet shape was formed by the combination of 2 horns. The left horn arises from the energy level with $m_I=+1$, and the right horn arises from the energy level with $m_I=-1$.

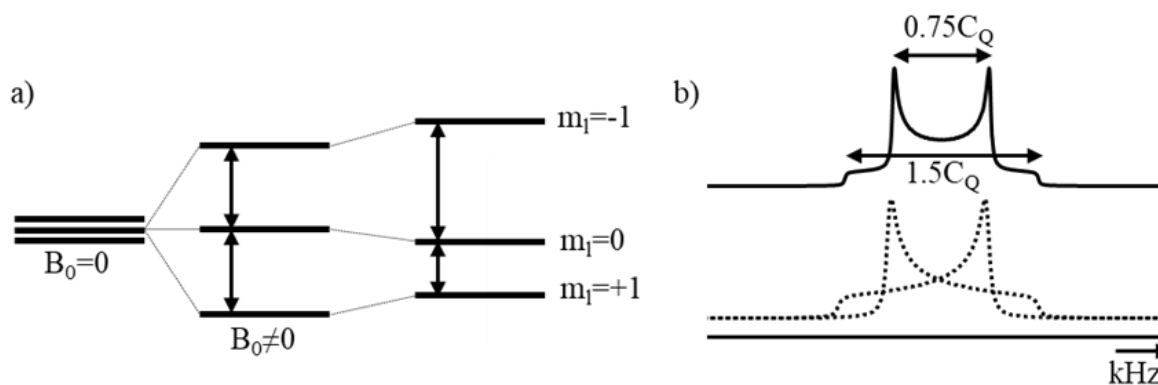


Figure 1.16. Quadrupolar interaction when $I=1$

The subsequent sections delve into SSNMR techniques and their applications in the context of the quadrupolar interactions, increasing our comprehension of this complex phenomenon and its significance in elucidating the motional and structural characteristics of various molecular systems.

1.3.7. SSNMR spectral simulations

Two types of simulations can be performed based on the NMR spectra of the molecules: analytical (Wsolids), and motional (EXPRESS). Which allows further analysis through the extraction of spectral parameters and motional information.

1.3.8. Probing CO₂ adsorption behavior using static SSNMR

For ¹³C SSNMR, the static NMR line shape is mainly determined by the chemical shift anisotropy (CSA), where distribution of the orientation of the CO₂ molecules in a powder sample gives rise to the ¹³C line shape. The ¹³C line shape can be described with 3 parameters: isotropic chemical shift (δ_{iso}), span (Ω), and skew (κ), which can be extracted by simulating the ¹³C experimental line shape using software Wsolids²⁵. The 3 parameters have different effects on the pattern as shown in **Figure 1.17**. Using the chemical shift tensor parameters extracted from experimental spectra, motional simulations were further carried out to simulate the effects of different types and rates of molecular motions on NMR spectra and to extract the parameters defining the motions (such as motional rates and angles). The effect of jump rates and different motions are shown in **Figure 1.18**.

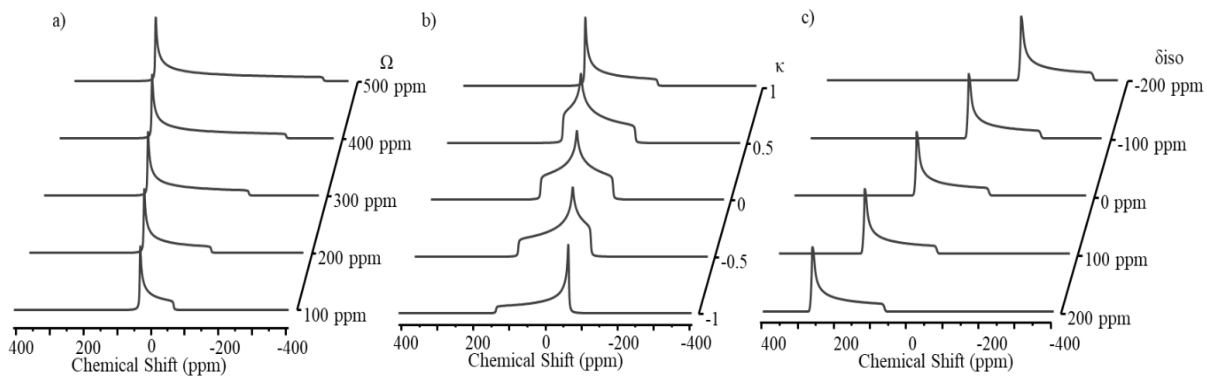


Figure 1.17. Effects of a) span Ω ($\delta_{\text{iso}} = 125$ ppm, $\kappa = 1$) and b) skew κ ($\delta_{\text{iso}} = 125$ ppm, $\Omega = 200$ ppm) and c) isotropic chemical shift δ_{iso} ($\Omega = 200$ ppm, $\kappa = 1$) on the ^{13}C SSNMR pattern.

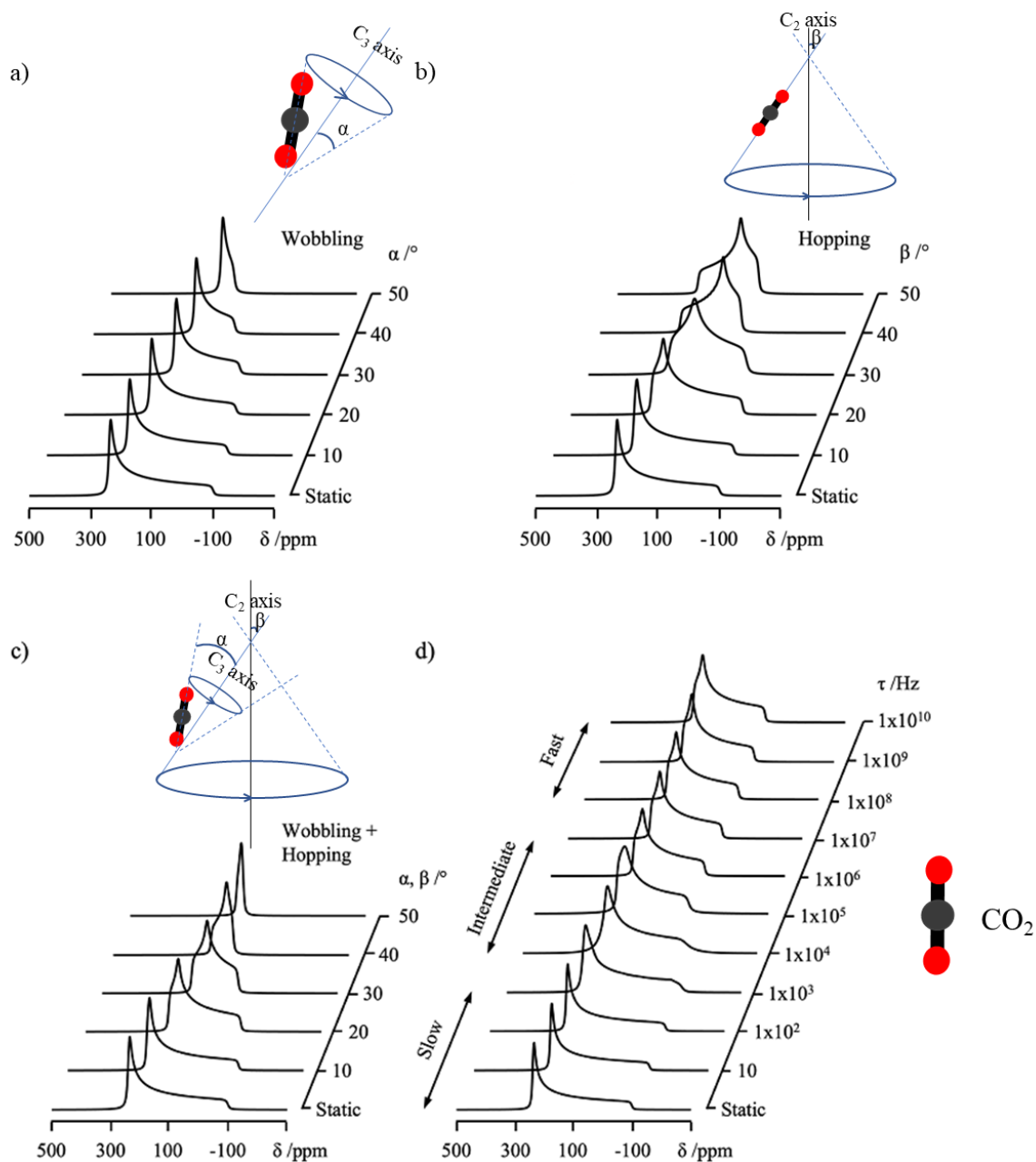


Figure 1.18. Simulated static ^{13}C SSNMR spectra of CO_2 undergoing a) C_3 wobbling motion at different angles, b) C_2 hopping motion at different angles, c) combined C_2 hopping and C_3 wobbling motion at different angles, d) Simulated ^{13}C SSNMR pattern of CO_2 undergoing C_2 hopping and C_3 wobbling at different jumping rates ($\alpha = 40^\circ$, $\beta = 40^\circ$). The spectra were simulated with Express²⁶ software. The ^{13}C SSNMR parameters of static CO_2 are $\delta_{\text{iso}} = 125$ ppm, $\Omega = 335$ ppm, and $\kappa = 1$.

1.3.9. Probing D₂O adsorption behavior using static ²H SSNMR

For ²H (I=1) SSNMR, the static NMR signals are mainly dominated by the first order quadrupolar interaction as ²H has a spin of I=1 (**Figure 1.19 (a)**). The quadrupolar interaction arises from the interaction between the ²H's quadrupole moment and the electric field gradient generated by its electronic environment. The two allowed transitions between $m_I = 1 \leftrightarrow 0$ and $m_I = -1 \leftrightarrow 0$ give rise to a doublet pattern. The overall ²H pattern has a symmetric shape called a Pake doublet with the horn separation of $0.75C_Q$ and breadth of signal of $1.5C_Q$ when the asymmetric parameter is 0 (**Figure 1.19 (b)**). Again, the ²H experimental pattern can be simulated to obtain the 2 parameters using Wsolids²⁵ (**Figure 1.20**). After extracting the 2 parameters from Wsolids²⁵, the Express software²⁶ was used to simulate the types and rates of molecular motions on the SSNMR spectra and to extract the motional rates and angles of the molecules. The effect of different motions on the ²H SSNMR pattern is shown in **Figure 1.21**.

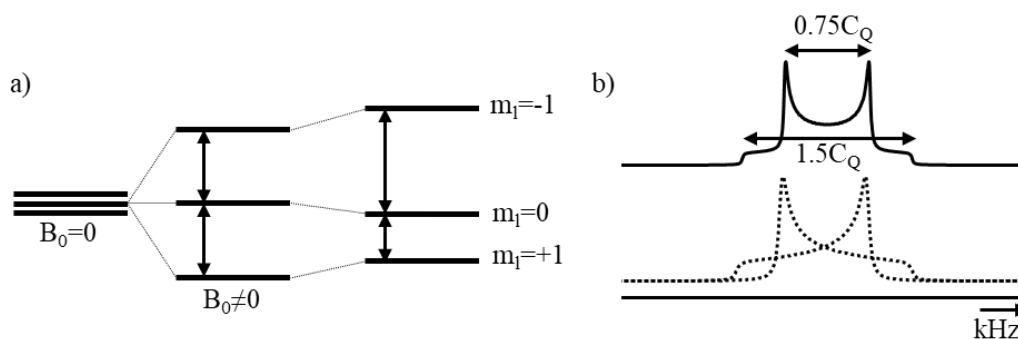


Figure 1.19. a) Energy level diagram of ²H (I = 1), b) Pake doublet pattern formed by ²H.

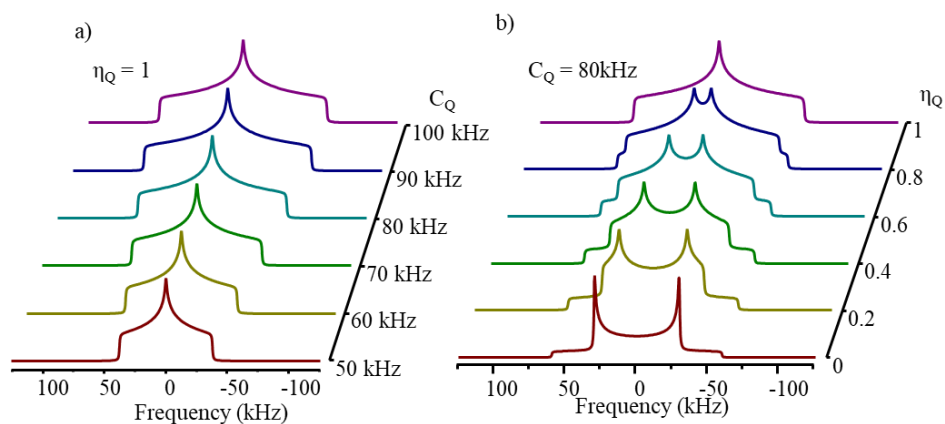


Figure 1.20. Effects of (a) quadrupolar coupling constant C_Q and (b) η_Q on the ²H SSNMR pattern.

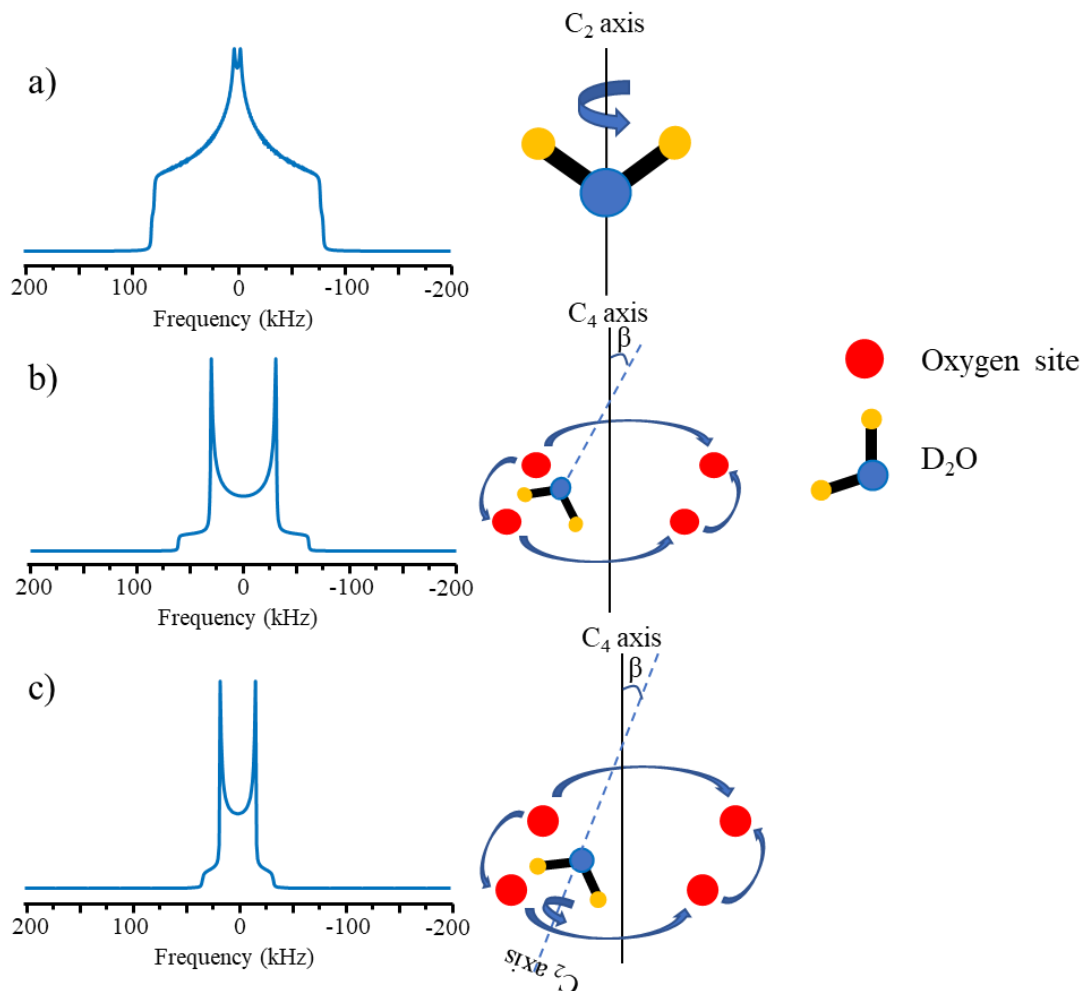


Figure 1.21. Simulated static ^2H SSNMR spectra of a) π -flipflop motion at an angle of 54° , b) 4 site jumping motion at an angle of 40° , c) combined π -flipflop and 4 site jumping motion $\alpha=54^\circ$ $\beta=40^\circ$. The spectra were simulated with Express²⁶ software. The ^2H SSNMR parameter of static D_2O are $C_Q = 215$ kHz, and $\eta_Q = 0$.

References:

1. Hoskins, B. F.; Robson, R. Design and Construction of a New Class of Scaffolding-like Materials Comprising Infinite Polymeric Frameworks of 3D-Linked Molecular Rods. A Reappraisal of the $\text{Zn}(\text{CN})_2$ and $\text{Cd}(\text{CN})_2$ Structures and the Synthesis and Structure of the Diamond-Related Frameworks $[\text{N}(\text{CH}_3)_4][\text{CuI}\text{ZnII}(\text{CN})_4]$ and $\text{CuI}[4,4',4'',4''']$ -

- Tetracyanotetraphenylmethane]BF₄·xC₆H₅NO₂. *J. Am. Chem. Soc.* **1990**, *112* (4), 1546–1554. <https://doi.org/10.1021/ja00160a038>.
2. Yaghi, O., Li, G. & Li, H. Selective binding and removal of guests in a microporous metal–organic framework. *Nature* **378**, 703–706 (1995). <https://doi.org/10.1038/378703a0>
 3. Liu, X.; Zhang, L.; Wang, J. Design Strategies for MOF-Derived Porous Functional Materials: Preserving Surfaces and Nurturing Pores. *J. Mater.* **2021**, *7* (3), 440–459. <https://doi.org/10.1016/j.jmat.2020.10.008>.
 4. Ding, M.; Cai, X.; Jiang, H. L. Improving MOF Stability: Approaches and Applications. *Chem. Sci.* **2019**, *10* (44), 10209–10230. <https://doi.org/10.1039/c9sc03916c>.
 5. Rowsell, J. L. C.; Yaghi, O. M. Effects of Functionalization, Catenation, and Variation of the Metal Oxide and Organic Linking Units on the Low-Pressure Hydrogen Adsorption Properties of Metal-Organic Frameworks. *J. Am. Chem. Soc.* **2006**, *128* (4), 1304–1315. <https://doi.org/10.1021/ja056639q>.
 6. Adegoke, K. A.; Maxakato, N. W. Porous Metal-Organic Framework (MOF)-Based and MOF-Derived Electrocatalytic Materials for Energy Conversion. *Mater. Today Energy* **2021**, *21*, 100816. <https://doi.org/10.1016/j.mtener.2021.100816>.
 7. Wu, M. X.; Yang, Y. W. Metal–Organic Framework (MOF)-Based Drug/Cargo Delivery and Cancer Therapy. *Adv. Mater.* **2017**, *29* (23), 1–20. <https://doi.org/10.1002/adma.201606134>.
 8. Bavykina, A.; Kolobov, N.; Khan, I. S.; Bau, J. A.; Ramirez, A.; Gascon, J. Metal-Organic Frameworks in Heterogeneous Catalysis: Recent Progress, New Trends, and Future Perspectives. *Chem. Rev.* **2020**, *120* (16), 8468–8535. <https://doi.org/10.1021/acs.chemrev.9b00685>.
 9. Li, S.; Chen, Y.; Pei, X.; Zhang, S.; Feng, X.; Zhou, J.; Wang, B. Water Purification: Adsorption over Metal-Organic Frameworks. *Chinese J. Chem.* **2016**, *34* (2), 175–185. <https://doi.org/10.1002/cjoc.201500761>.
 10. Wang, H.; Yao, K.; Zhang, Z.; Jagiello, J.; Gong, Q.; Han, Y.; Li, J. The First Example of Commensurate Adsorption of Atomic Gas in a MOF and Effective Separation of Xenon from Other Noble Gases. *Chem. Sci.* **2014**, *5* (2), 620–624. <https://doi.org/10.1039/c3sc52348a>.
 11. DeSantis, D.; Mason, J. A.; James, B. D.; Houchins, C.; Long, J. R.; Veenstra, M. Techno-Economic Analysis of Metal-Organic Frameworks for Hydrogen and Natural Gas Storage. *Energy and Fuels* **2017**, *31* (2), 2024–2032. <https://doi.org/10.1021/acs.energyfuels.6b02510>.

12. Carrasco, S. Metal-Organic Frameworks for the Development of Biosensors: A Current Overview. *Biosensors* **2018**, *8* (4), 92. <https://doi.org/10.3390/bios8040092>.
13. Fan, W.; Liu, X.; Wang, X.; Li, Y.; Xing, C.; Wang, Y.; Guo, W.; Zhang, L.; Sun, D. A Fluorine-Functionalized Microporous in-Mof with High Physicochemical Stability for Light Hydrocarbon Storage and Separation. *Inorg. Chem. Front.* **2018**, *5* (10), 2445–2449. <https://doi.org/10.1039/c8qi00652k>.
14. Petit, C. Present and Future of MOF Research in the Field of Adsorption and Molecular Separation. *Curr. Opin. Chem. Eng.* **2018**, *20*, 132–142. <https://doi.org/10.1016/j.coche.2018.04.004>.
15. Ramanayaka, S.; Vithanage, M.; Sarmah, A.; An, T.; Kim, K.-H.; Ok, Y. S. Performance of Metal–Organic Frameworks for the Adsorptive Removal of Potentially Toxic Elements in a Water System: A Critical Review. *RSC Advances* **2019**, *9* (59), 34359–34376. <https://doi.org/10.1039/C9RA06879A>.
16. *Introduction to Carbon Capture and Storage (CCS) Technology*. Energy News for the Canadian Oil & Gas Industry | EnergyNow.ca. <https://energynow.ca/2022/02/introduction-to-carbon-capture-and-storage-ccs-technology/>.
17. Yang, Y.; Lin, R.; Ge, L.; Hou, L.; Bernhardt, P.; Rufford, T. E.; Wang, S.; Rudolph, V.; Wang, Y.; Zhu, Z. Synthesis and Characterization of Three Amino-Functionalized Metal–Organic Frameworks Based on the 2-Aminoterephthalic Ligand. *Dalton Trans.* **2015**, *44* (17), 8190–8197. <https://doi.org/10.1039/c4dt03927k>.
18. Anderson, T. R.; Hawkins, E.; Jones, P. D. CO₂, the Greenhouse Effect and Global Warming: From the Pioneering Work of Arrhenius and Callendar to Today 's Earth System Models. *Endeavour* **2016**, *40* (3), 178–187. <https://doi.org/10.1016/j.endeavour.2016.07.002>.
19. Clark, C.; Dutrow, B. *Single-crystal X-ray Diffraction*. Techniques. https://serc.carleton.edu/research_education/geochemsheets/techniques/SXD.html.
20. Lin, J.-B.; Nguyen, T. T. T.; Vaidhyanathan, R.; Burner, J.; Taylor, J. M.; Durekova, H.; Akhtar, F.; Mah, R. K.; Ghaffari-Nik, O.; Marx, S.; Fylstra, N.; Iremonger, S. S.; Dawson, K. W.; Sarkar, P.; Hovington, P.; Rajendran, A.; Woo, T. K.; Shimizu, G. K. H. A Scalable Metal-Organic Framework as a Durable Physisorbent for Carbon Dioxide Capture. *Science* **2021**, *374* (6574), 1464–1469. <https://doi.org/10.1126/science.abi7281>.

21. Pires, J. C. M.; Martins, F. G.; Simões, M. Recent Developments on Carbon Capture and Storage: An Overview. *Chem. Eng. Res. Des.* **2011**, *89* (9), 1446–1460. <https://doi.org/10.1016/j.cherd.2011.01.028>.
22. Wilberforce, T.; Olabi, A. G.; Sayed, E. T.; Elsaid, K.; Abdelkareem, M. A. Progress in Carbon Capture Technologies. *Sci. Total Environ.* **2021**, *761* (xxxx), 143203. <https://doi.org/10.1016/j.scitotenv.2020.143203>.
23. Yap, M. H.; Fow, K. L.; Chen, G. Z. Synthesis and Applications of MOF-Derived Porous Nanostructures. *Green Energy Environ.* **2017**, *2* (3), 218–245. <https://doi.org/10.1016/j.gee.2017.05.003>.
24. Poloni, R.; Smit, B.; Neaton, J. B. Ligand-Assisted Enhancement of CO₂ Capture in Metal-Organic Frameworks. *J. Am. Chem. Soc.* **2012**, *134* (15), 6714–6719. <https://doi.org/10.1021/ja2118943>.
25. Fernández, J. R.; Garcia, S.; Sanz-Pérez, E. S. CO₂ Capture and Utilization Editorial. *Ind. Eng. Chem. Res.* **2020**, *59* (15), 6767–6772. <https://doi.org/10.1021/acs.iecr.0c01643>.
26. Zhai, Q. G.; Bai, N.; Li, S.; Bu, X.; Feng, P. Design of Pore Size and Functionality in Pillar-Layered Zn-Triazolate-Dicarboxylate Frameworks and Their High CO₂/CH₄ and C₂ Hydrocarbons/CH₄ Selectivity. *Inorg. Chem.* **2015**, *54* (20), 9862–9868. <https://doi.org/10.1021/acs.inorgchem.5b01611>.
27. D'Alessandro, D. M.; Smit, B.; Long, J. R. Carbon Dioxide Capture: Prospects for New Materials. *Angew. Chemie - Int. Ed.* **2010**, *49* (35), 6058–6082. <https://doi.org/10.1002/anie.201000431>.
28. Keskin, S.; van Heest, T. M.; Sholl, D. S. Can Metal-Organic Framework Materials Play a Useful Role in Large-Scale Carbon Dioxide Separations? *ChemSusChem* **2010**, *3* (8), 879–891. <https://doi.org/10.1002/cssc.201000114>.
29. Yu, J.; Balbuena, P. B. Water Effects on Postcombustion Co₂ Capture in Mg-MOF-74. *J. Phys. Chem. C* **2013**, *117* (7), 3383–3388. <https://doi.org/10.1021/jp311118x>.
30. Kondo, M.; Okubo, T.; Asami, A.; Noro, S.; Yoshitomi, T.; Kitagawa, S.; Ishii, T.; Matsuzaka, H.; Seki, K. Rational Synthesis of Stable Channel-Like Cavities with Methane Gas Adsorption. **1999**, No. 1, 140–143.
31. Sutrisno, A.; Huang, Y. Solid-State NMR: A Powerful Tool for Characterization of Metal – Organic Frameworks. *Solid State Nucl. Magn. Reson.* **2013**, *49–50*, 1–11. <https://doi.org/10.1016/j.ssnmr.2012.09.003>.

32. Lucier, B. E. G.; Chen, S.; Huang, Y. Characterization of Metal-Organic Frameworks: Unlocking the Potential of Solid-State NMR. *Acc. Chem. Res.* **2018**, *51* (2), 319–330. <https://doi.org/10.1021/acs.accounts.7b00357>.
33. Eichele K., Wasylishen R. E., WSolids1: Solid-State NMR Spectrum Simulation Package, ver. 1.20.21; Universität Tübingen: Tübingen, **2013**.
34. Vold, R. L.; Hoatson, G. L. Effects of Jump Dynamics on Solid State Nuclear Magnetic Resonance Line Shapes and Spin Relaxation Times. *J. Magn. Reson.* **2009**, *198*, 57–72.
35. Miyatou, T.; Ohashi, R.; Ida, T.; Kittaka, S.; Mizuno, M. An NMR Study on the Mechanisms of Freezing and Melting of Water Confined in Spherically Mesoporous Silicas SBA-16. *Phys. Chem. Chem. Phys.* **2016**, *18* (27), 18555–18562. <https://doi.org/10.1039/c6cp03111k>.
36. Liu, J.; He, X.; Zhang, J. Z. H.; Qi, L. W. Hydrogen-Bond Structure Dynamics in Bulk Water: Insights from: Ab Initio Simulations with Coupled Cluster Theory. *Chem. Sci.* **2018**, *9* (8), 2065–2073. <https://doi.org/10.1039/c7sc04205a>.
37. Qiu, X. F.; Zhu, H. L.; Huang, J. R.; Liao, P. Q.; Chen, X. M. Highly Selective CO₂ Electroreduction to C₂H₄ Using a Metal-Organic Framework with Dual Active Sites. *J. Am. Chem. Soc.* **2021**, *143* (19), 7242–7246. <https://doi.org/10.1021/jacs.1c01466>.
38. Wan, Y.; Miao, Y.; Zhong, R.; Zou, R. High-Selective CO₂ Capture in Amine-Decorated Al-MOFs. **2022**, 1–10.
39. Sato, K.; Hunger, M. Carbon Dioxide Adsorption in Open Nanospaces Formed by Overlap of Saponite Clay Nanosheets. *Commun. Chem.* **2020**, *3* (1), 1–7. <https://doi.org/10.1038/s42004-020-00346-5>.
40. Sajid Ur Rehman; Xu, S.; Han, X.; Tao, T.; Li, Y.; Yu, Z.; Ma, K.; Xu, W.; Wang, J. The Role of NMR in Metal Organic Frameworks: Deep Insights into Dynamics, Structure and Mapping of Functional Groups. *Materials today advances* **2022**, *16*, 100287–100287. <https://doi.org/10.1016/j.mtadv.2022.100287>.
41. Wittebort, R. J.; Usha, M. G.; Ruben, D. J.; Wemmer, D. E.; Pines, A. Observation of Molecular Reorientation in Ice by Proton and Deuterium Magnetic Resonance. *J. Am. Chem. Soc.* **1988**, *110* (17), 5668–5671. <https://doi.org/10.1021/ja00225a013>
42. Duer, M. J. *Introduction to Solid-State NMR Spectroscopy*; Blackwell: Oxford, Uk; Malden, Ma, 2004.

43. Kenneth J.D. MacKenzie; Smith, M. E. *Multinuclear Solid-State Nuclear Magnetic Resonance of Inorganic Materials*; Elsevier, 2002.
44. McBrierty, V. J. NMR Spectroscopy of Polymers in the Solid State. *Elsevier eBooks* **1989**, 397–428. <https://doi.org/10.1016/b978-0-08-096701-1.00019-7>.
45. M. J. Duer. *Solid-State NMR Spectroscopy: Principles and Applications*. Blackwell Science, Oxford, 2002.
46. Oosterhuis, W. T.; Lang, G. Mössbauer Effect in Low-Spin (D7) Complex Molecules of Fe. *J. Chem. Phys.* **1969**, *50* (10), 4381–4387. <https://doi.org/10.1063/1.1670907>.
47. McBrierty, V. J. NMR Spectroscopy of Polymers in the Solid State. *Elsevier eBooks* **1989**, 397–428. <https://doi.org/10.1016/b978-0-08-096701-1.00019-7>.
48. Loughran, R. P.; Hurley, T.; Andrzej Gładysiak; Chidambaram, A.; Konstantin Khivantsev; Walter, E. D.; Graham, T. R.; Reardon, P.; Szanyi, J.; Fast, D. B.; Quin R.S. Miller; Ah-Hyung Alissa Park; Stylianou, K. C. CO₂ Capture from Wet Flue Gas Using a Water-Stable and Cost-Effective Metal-Organic Framework. *Cell Rep. Phys. Sci.* **2023**, *4* (7), 101470–101470. <https://doi.org/10.1016/j.xcrp.2023.101470>.
49. Liang, L.; Liu, C.; Jiang, F.; Chen, Q.; Zhang, L.; Xue, H.; Jiang, H.-L.; Qian, J.; Yuan, D.; Hong, M. Carbon Dioxide Capture and Conversion by an Acid-Base Resistant Metal-Organic Framework. *Nat. Commun.* **2017**, *8* (1). <https://doi.org/10.1038/s41467-017-01166-3>.
50. Liu, G.-Z.; Li, X.-L.; Xin, L.-Y.; Wang, L.-Y. Two Topologically New Trinodal Cobalt(II) Metal–Organic Frameworks Characterized as a 1D Metallic Oxide and a 2D → 3D Penetrated Porous Solid. *Cryst. Eng. Comm.* **2012**, *14* (16), 5315. <https://doi.org/10.1039/c2ce25556a>.

Chapter 2. Water Effects on CO₂ adsorption in MOF [Zn₂(TRZ)₂(NH₂-BDC)] at different loading levels and temperatures

2.1. Introduction

Since global warming has become an escalating environmental concern over the past decades, green house gas mitigation techniques such as carbon capture and storage (CCS) has been greatly investigated. Among the diverse range of storage materials, MOFs have drawn a significant attention in this field due to its exceptional performance on gas storage and separations. However, in practical applications, water is ubiquitous in the atmosphere, it can interfere with the CO₂ adsorption within the MOF. The CO₂ adsorption capacity can be negatively affected by the introduction of water molecules. Therefore, understanding the effects of water on the adsorption capacity in MOF is of great importance. In this chapter, a pillar layered MOF, [Zn₂(TRZ)₂(NH₂-BDC)] (ZTP-3), was selected due to its high CO₂ adsorption capacity and selectivity.¹ The adsorption behavior of CO₂ at different loading levels and temperatures were investigated to understand the influence of water.

2.2. Experimental section

2.2.1. MOF synthesis

As-made ZTP-3 sample was synthesized according to previously reported procedures with some modifications.¹ All starting materials were used as received without further purification. A mixture of zinc nitrate hexahydrate (Zn(NO₃)₂ · 6H₂O, 0.5952 g or 2.0 mmol, Alfa Aesar), 2-aminoterphthalic acid (NH₂BDC, 0.1812 g or 1.0 mmol, 99% Sigma Aldrich), and 1,2,4-triazole (C₂H₃N₃, 0.138 g, 2.0 mmol, 99% Alfa Aesar) were dissolved in 16 mL of N,N-Dimethylformamide (DMF, C₃H₇NO, Fisher Chemical), and 4 mL of deionized water (H₂O) in a 25 mL glass vial. The glass vial was sealed and placed in an oven at 120°C for 5 days. Light yellow crystal powder was obtained after cooling the sample to room temperature. Vacuum filtration was performed to remove unreacted reagents dissolved in the DMF solvent. To perform the vacuum

filtration, the powdered sample was washed with DMF, and dried using the vacuum. The pure sample was further collected and placed in an oven and dried at 80°C for 1 day. The resulting light-yellow crystal powder sample was referred to as-made ZTP-3 sample in this work.

2.2.2. Sample activation

To prepare ZTP-3 for loading guest molecules, activation of the MOF is necessary in order to remove all residual solvent molecules and unreacted chemicals. Prior to activation, solvent exchange using methanol (CH₃OH) was performed for ZTP-3 to shorten the activation time of the MOF since methanol is more volatile than DMF. The solvent exchange was performed by soaking and washing as-made ZTP-3 in methanol using centrifugation and vacuum filtration for 5 times repeatedly.

A Schlenk vacuum line was used to activate as-made ZTP-3. Approximately 0.15 g sample was first placed in an L-shaped glass tube which can fit into the 5 mm coil of the static probe. After placing the sample into the bottom of the tube, a small amount of glass wool was placed at the top of the sample to prevent the sample from escaping the glass tube to the Schlenk line. The Schlenk line has a pressure monitor attached and was connected to a vacuum pump. The pressure in the vacuum line was monitored to be 0 mbar during activation. Liquid nitrogen was used to cool the Schlenk line for the purpose of condensing solvent extracted from the framework. The glass tube was placed in a furnace at 110°C for 2 days and cooled to room temperature during the activation process. The end product of the activation gives rise to activated ZTP-3.

2.2.3. Powder X-ray diffraction (PXRD) measurements

Powder X-ray Diffraction patterns were performed to measure the diffraction pattern in order to confirm the phase purity and structure identity of the synthesized MOF by comparing the powder pattern of the synthesized product with the ones reported in literature¹ The PXRD pattern were obtained using a Inel CPS powder diffractometer operating with Cu K α radiation ($\lambda = 1.5406 \text{ \AA}$). The powder pattern was collected in the range $5^\circ \leq 2\theta \leq 45^\circ$ at a rate of 10°/min, with a step size of 0.02°.

2.2.4. Thermogravimetric analysis (TGA)

To confirm the completion of solvent removal during the activation process, thermogravimetric analysis of as-made and activated samples was carried out under N₂ atmosphere (40 mL·min⁻¹) using Mettler Toledo AG TGA/SDTA851e instrument. The samples were heated from 30 to 800 °C at a rate of 10 °C·min⁻¹. The TGA graphs were compared to those provided in the literature.¹

2.2.5. CO₂ adsorption

¹³C isotopically labeled ¹³CO₂ (<3 atom % ¹⁸O, 99 atom % ¹³C isotope enriched, Sigma-Aldrich) was used as one of the guest molecules in this work since ¹³C is an NMR active nucleus.

Approximately 200 mbar of ¹³CO₂ gas was first condensed into a glass Schlenk glass flask in the Schlenk line using liquid nitrogen. The L-shaped tube was then connected to the Schlenk line and evacuated under vacuum. ~50-180 mbar of ¹³CO₂ (depending on the loading level) in the flask was then released to the enclosed Schlenk line while the L-shaped tube containing the activated sample was immersed in liquid nitrogen. The designated amount of ¹³CO₂ was then adsorbed by the ZTP-3. The L-shaped tube was then flame sealed using a torch while immersing the sample part into liquid nitrogen.

After the sealed tube reached room temperature, it was then placed in the oven at 80°C in an autoclave for at least 12 hours to reach the equilibrium of the adsorption process. The equilibrated sample was then cooled to room temperature prior to SSNMR measurements.

2.2.6. D₂O adsorption

Deuterium Oxide (D₂O, 99.9% Cambridge Isotope Laboratories) was used as one of the guest molecules in this work.

After the furnace was removed from the activated sample, different amounts (4-15µL) of D₂O were loaded into the sample using a syringe. The pressure in the L-shaped tube was then evacuated by connecting to the vacuum line. The L-shaped tube was then immersed in liquid nitrogen, and flame sealed using a torch.

After the sealed tube reached room temperature, it was then placed in the oven at 80°C in an autoclave for at least 12 hours to reach the equilibrium of the adsorption process. The equilibrated sample was then cooled to room temperature prior to SSNMR measurements.

2.2.7. Co-adsorption of CO₂ and D₂O

Co-adsorption of CO₂ and D₂O involves the combination of the 2 processes mentioned above. The sample was first loaded with D₂O using a syringe, evacuated under vacuum, and then loaded with CO₂ using liquid nitrogen. The co-adsorbed sample was also flame sealed using a torch.

The sealed tube was cooled to room temperature and then placed in the oven at 80°C in an autoclave for at least 12 hours to reach equilibrium. The equilibrated sample was then cooled to room temperature prior to SSNMR measurements.

2.2.8. Solid-State Nuclear Magnetic Resonance Spectroscopy (SSNMR)

¹³C, and ²H SSNMR experiments were conducted on a 400WB Varian Infinity Plus SSNMR spectrometer operating at a magnetic field of 9.4 T. Variable temperature experiments were performed using a Varian VT temperature control unit.

2.2.8.1. Cross polarization Magic-angle spinning (CPMAS)

¹H-¹³C cross polarization (CP) experiments were conducted using a 5mm HXY Varian/Chemagnetics probe at a spinning rate of 10 kHz. ¹H-¹³C CP MAS spectra were acquired using a contact time of 9 ms. The spectra were referenced using solid adamantane set at a chemical shift of 38.5 ppm.¹⁰ The 90° pulse width was set to 2.7 μs, and the pulse delay was set to 3.0 s. Samples were first prepared in L-shaped glass tubes and then transferred to the 5mm rotor in a glove box filled with N₂. Acquisition numbers vary between 1000-2000 depending on signal intensity. All ¹H-¹³C CP MAS spectra were measured at room temperature.

2.2.8.2. Static SSNMR

Static ²H and ¹³C SSNMR spectra of activated samples of ZTP-3 with different D₂O and/or CO₂ loadings were measured with Varian Infinity Plus spectrometer equipped with a 9.4 T Oxford Instruments superconducting magnet and a double channel (HX) 5 mm Varian/Chemagnetics static probe.

^2H static SSNMR were obtained at Larmor frequency $\nu_0 = 61.32$ MHz. A quadrupolar echo sequence was used to eliminate spectral distortion. The spectra were referenced using liquid D_2O set at a chemical shift of 4.8 ppm.¹¹ The parameters used were 90° pulse width = $2.20 \mu\text{s}$; separation between pulses $\tau = 30 \mu\text{s}$; pulse delay = 0.5 s; spectral width = 500 kHz; and number of scans = 1000 – 120000, depending on signal intensity.

^{13}C static SSNMR spectra were acquired at Larmor frequency $\nu_0 = 100.46$ MHz. The experiment was performed using the DEPTH-echo pulse sequence. The spectra were referenced using liquid ethanol ($\text{C}_2\text{H}_6\text{O}$) set at a chemical shift of 56.96 ppm.¹¹ The parameters used were 90° pulse width = $2.50 \mu\text{s}$; pulse delay = 3.0 s; spectral width = 149.254 kHz; and number of scans = 1000 – 120000, depending on signal intensity.

Static variable temperature (VT) SSNMR spectra of loaded samples were collected at temperatures between 213 K and 373 K using a Varian VT temperature control unit to probe D_2O and/or CO_2 motions in ZTP-3. The spectrum at each temperature was not measured until the temperature was stable and the sample reached thermal equilibrium. Each spectrum was measured when the temperature has been stable for around 10 minutes.

2.2.8.3. Spectral simulations

Simulations of the experimental ^2H static SSNMR spectra were carried out using Wsolids package³ and EXPRESS software⁴. The simulated ^{13}C and ^2H powder patterns were obtained through varying the C_Q and η_Q input values in Wsolids³ to match the experiment NMR patterns. ^{13}C and ^2H powder patterns obtained through matching with Wsolids simulated patterns using EXPRESS⁴ were used to extract the information on the types of D_2O and CO_2 motions and the parameters defining particular motions. The known parameters for static CO_2 are $\delta_{\text{iso}} = 125$ ppm, $\Omega = 335$ ppm, and $\kappa = 1$.² The known parameters for static D_2O and ND_2 are C_Q (^2H) = 225 kHz and $\eta_Q = 0$, and C_Q (^2H) = 200 kHz and $\eta_Q = 0$, respectively.^{5,6}

2.3. Results and discussion

2.3.1. Characterization

2.3.1.1. PXRD results

The ZTP-3 structure is constructed by connecting the Zn-triazolate 2D layers with the 2-amino-1,4-benzenedicarboxylate pillars. The distance between each layer is $\sim 10.8 \text{ \AA}$.¹ The identity and purity of the sample were confirmed by PXRD. The experimental powder pattern matches well with the simulated pattern as shown in **Figure 2.1**. At higher 2θ range, diffraction pattern could be possibly affected by the present of solvent, resulting in peak shifts.

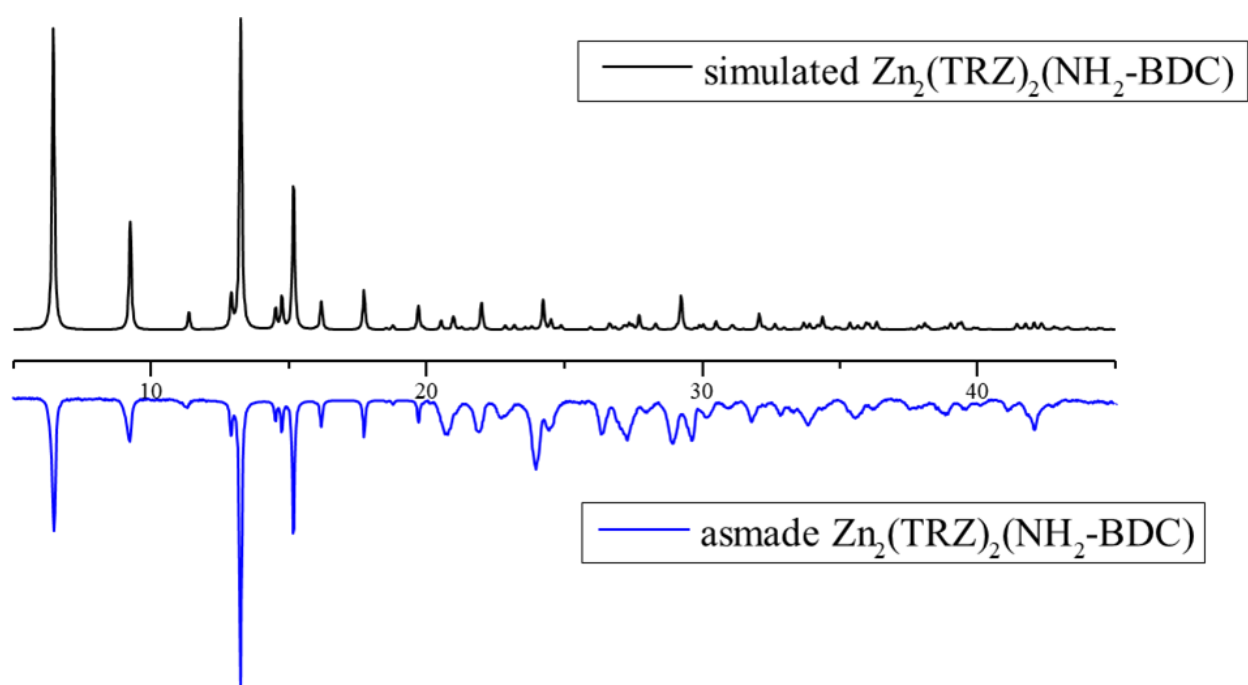


Figure 2.1. Powder X-ray diffraction pattern (PXRD) of ZTP-3 and the simulated as-made PXRD pattern based on the crystal structure provided in the literature¹.

2.3.1.2. TGA results

The activation process of ZTP-3 was confirmed by temperature programmed TGA. Activation refers to the process of removing solvents from the pores of sample to create available binding sites for guest molecules. Therefore, the complete removal of solvents is an indication of successful activation. By monitoring the weight loss of the sample as a function of temperature, 2 weight

losses responsible for the solvent desorption of water and DMF were observed for the as-made sample (**Figure 2.2**). The 8% weight loss from 100% to 91% starting from 87°C indicates departure of water. At 271 °C, the weight dropped from 91% to 79%, responsible for the removal of DMF. The 2 weight losses were not observed in the TGA graph of activated sample, which indicates the successful activation of sample. Furthermore, the decomposition temperature of the as-made and activated sample were found to be around 376°C, which matches well with the literature value of 380°C.¹

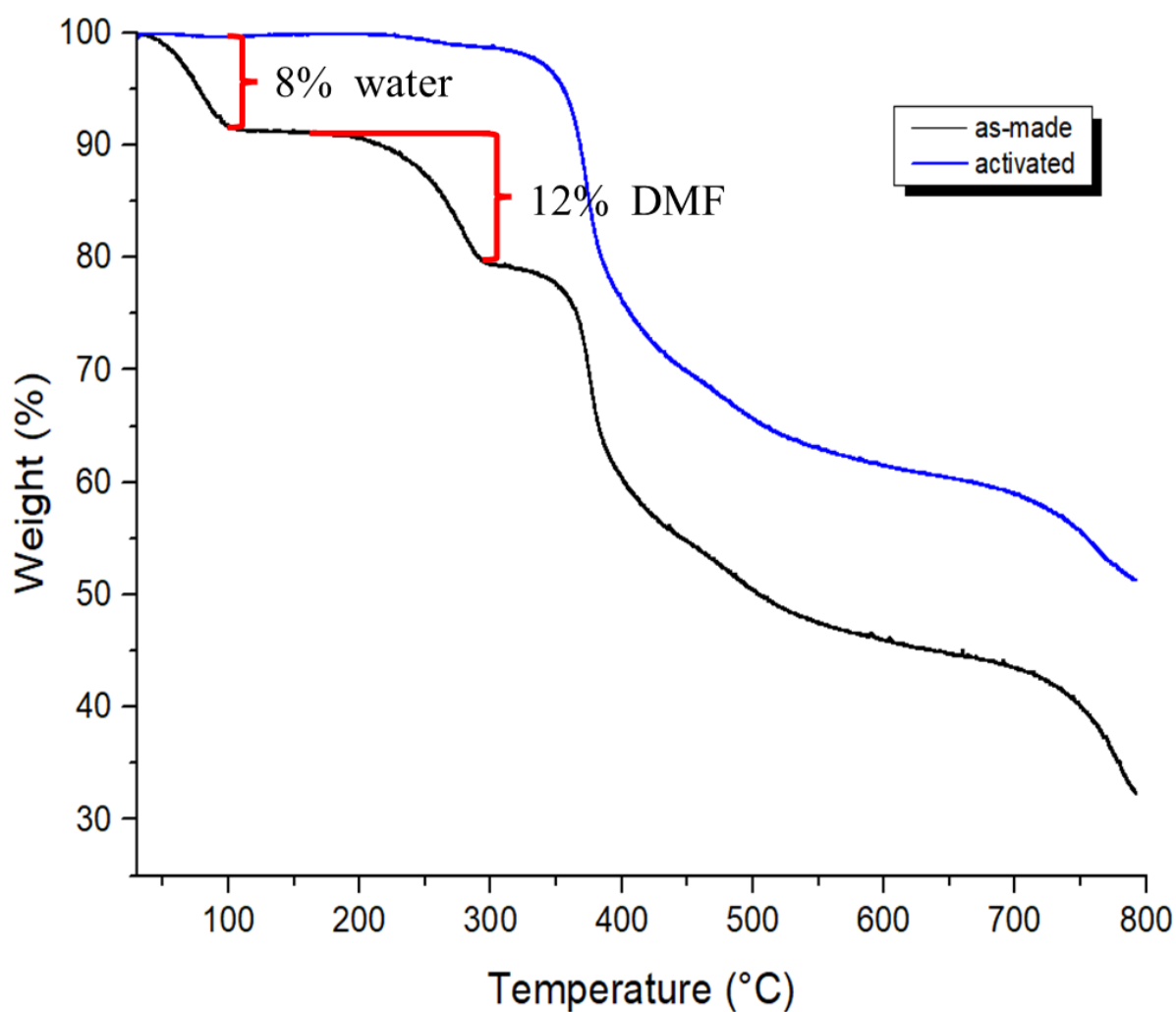


Figure 2.2. Thermogravimetric analysis (TGA) curves of as-made (black curve) and activated (blue curve) ZTP-3

2.3.1.3. Distribution of guest molecules in ZTP-3

According to the structural information provided by the literature¹, ZTP-3 consists of large cages each featuring a narrow top part and a wide bottom part with varying dimensions as depicted in **Figure 2.3**. Guest molecules can be possibly adsorbed at the adsorption sites in both parts of the cages. Based on the symmetry and structural information provided, each unit cell consists of 8 cages, and 16 Zn ions. Each of the cages would therefore have 2 Zn ions on average. Number of molecules on average for each cage can therefore be calculated as following:

Table 2.1. Average distribution of guest molecules within ZTP-3

# of equivalents per Zn	average # of guest molecules in each cage	
0.25eq	0.5	1 molecule in every 2 cages
0.5eq	1	1 molecule in each cage
0.75eq	1.5	3 molecules in every 2 cages
1eq	2	2 molecules in each cage

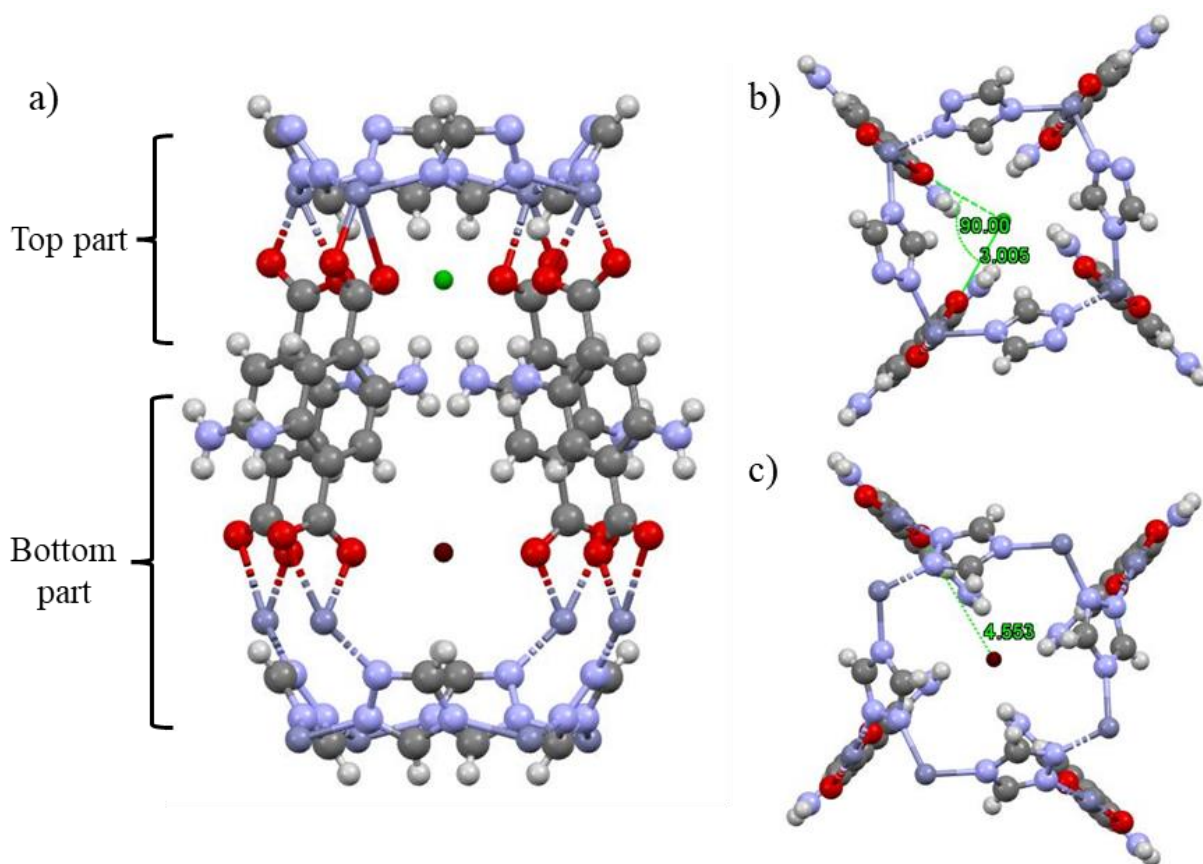


Figure 2.3. (a) Possible 2 adsorption location in each ZTP-3 cage (b) top view of top part (green) (c) bottom view of the bottom part (brown)

2.3.2. Static ¹³C variable temperature (VT) SSNMR

The majority of static ¹³C VT SSNMR spectra at different pure CO₂ loadings contain 1 signal (CO₂ signal 1) as depicted in **Figure 2.4.(a)**. The spectra consist of a narrow signal ($\Omega = 100$ -130 ppm) (relatively mobile) from adsorbed CO₂ at ~ 125 ppm, which is significantly narrower than the signal of rigid CO₂ (see **Figure 2.5**).¹² The breadth of the signals is almost identical for all loadings, indicating that the adsorbed CO₂ motions has very little difference. The experimental and simulated static VT ¹³C spectra with 0.25eq CO₂ loading are shown in **Figure 2.6**. At higher temperatures, an isotropic free CO₂ signal also appeared in the pattern, suggesting that a small amount of CO₂ was desorbed with an increase in temperature. For the highest loading at 0.75eq, a broader signal (CO₂ signal 2) was observed ($\Omega = \sim 250$ ppm). Although motional information could not be extracted from this signal, it was suspected to be contributed by a different CO₂ motion (**Figure 2.7**).

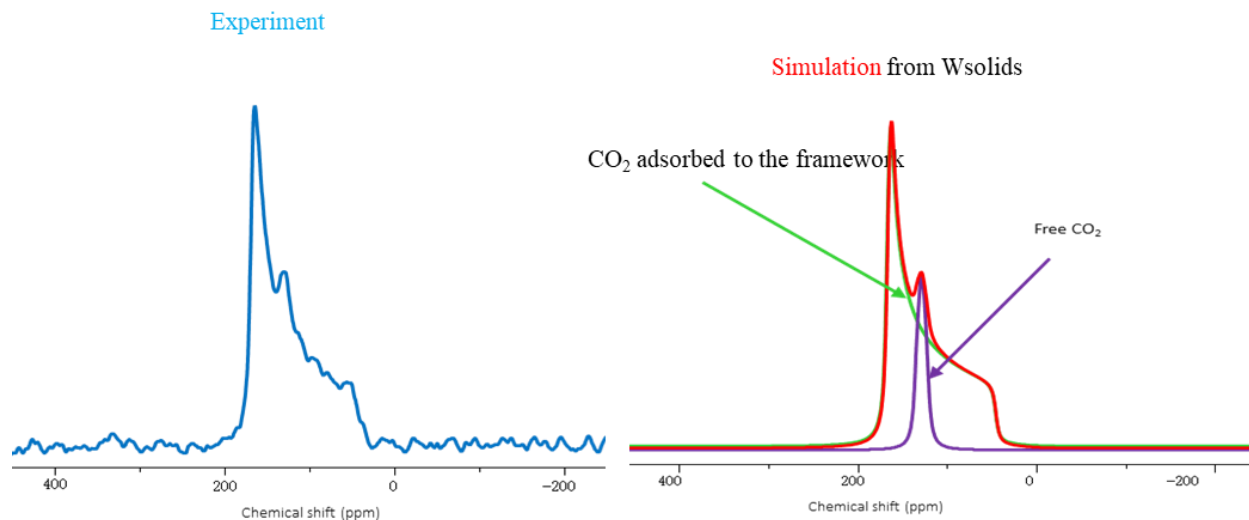


Figure 2.4. VT static ^{13}C SSNMR pattern of CO_2 with 0.25eq CO_2/Zn loading at 373 K for ZTP-3.³

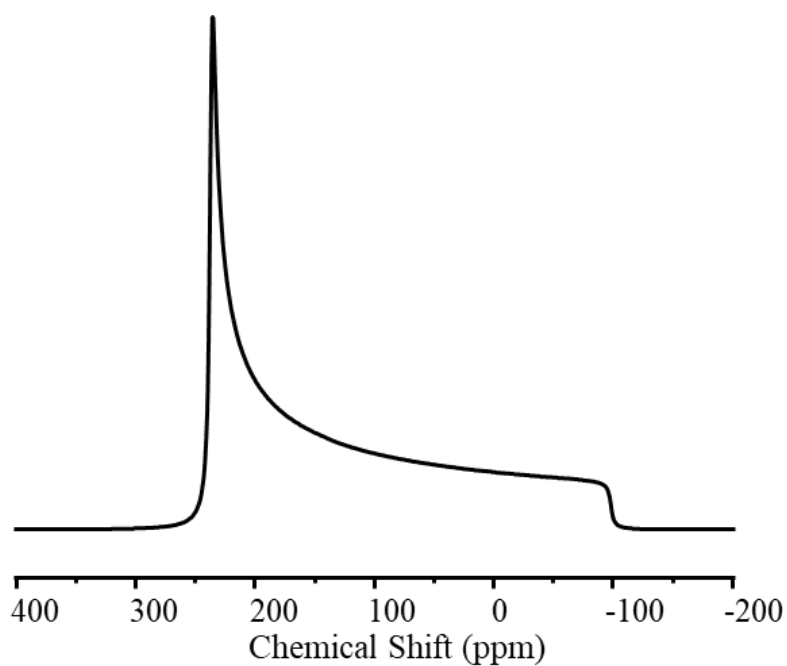


Figure 2.5. Simulated static ^{13}C SSNMR spectra of rigid CO_2 ($\delta_{iso}=125$ ppm, $\Omega = 335$ ppm, $\kappa = 1$).¹²

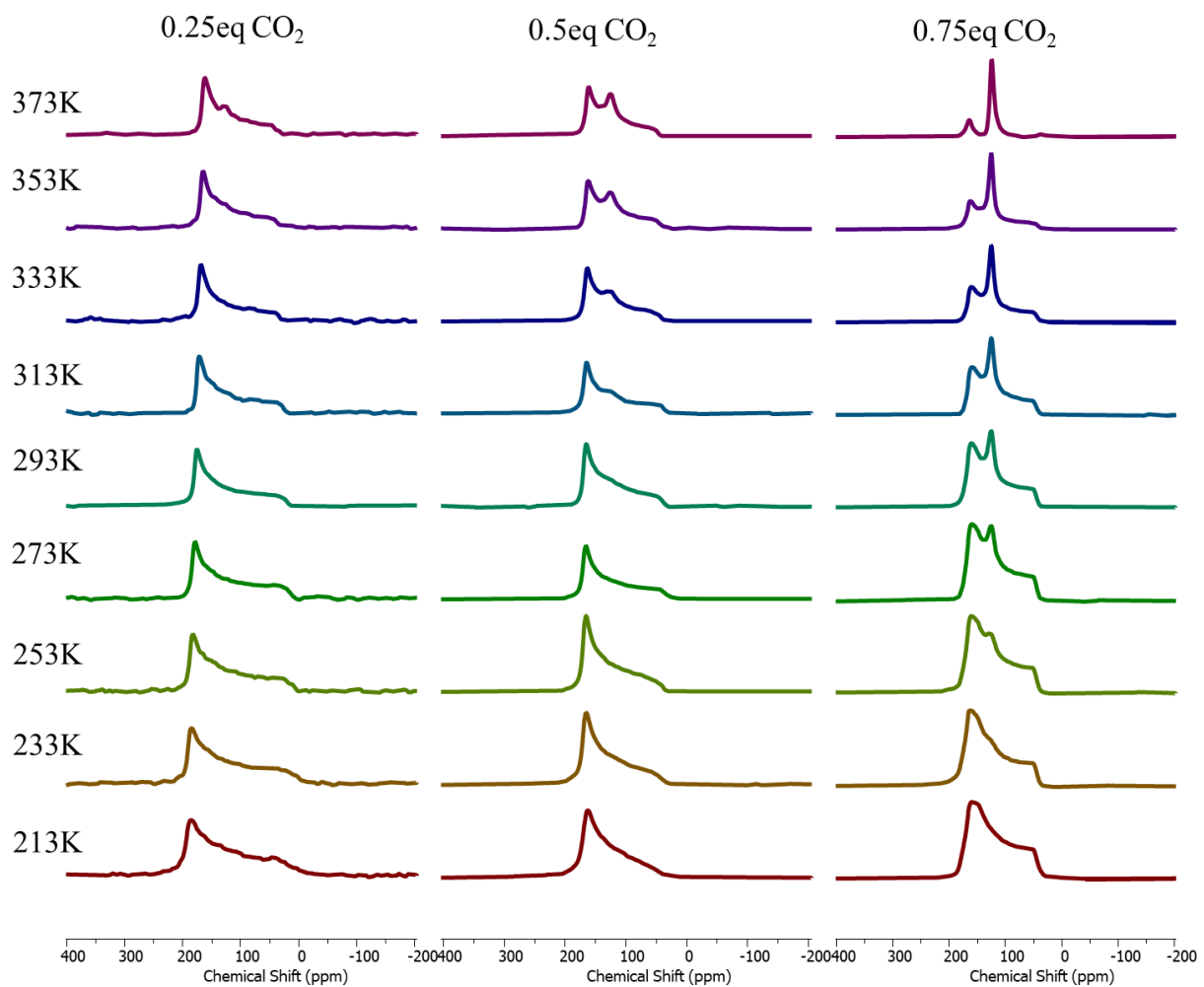


Figure 2.6. Experimental VT static ^{13}C SSNMR spectra of CO_2 at different pure CO_2 loadings from 213 K to 373 K for MOF ZTP-3.

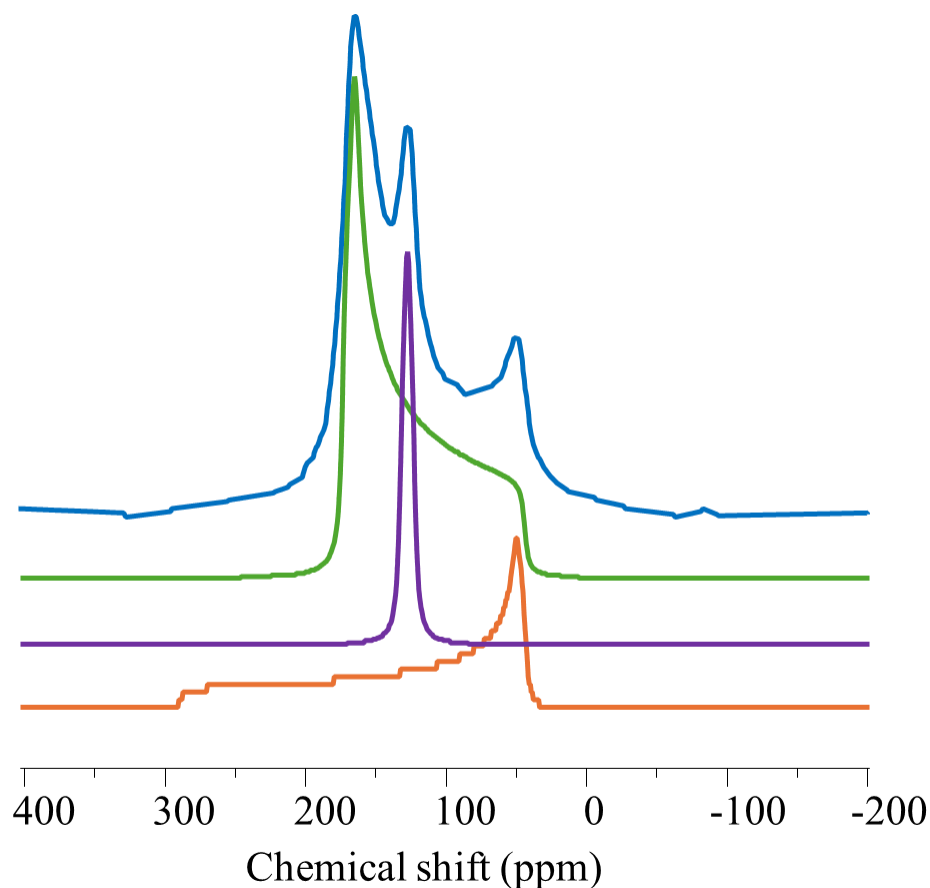


Figure 2.7. VT static ^{13}C SSNMR pattern of CO_2 with 0.75eq CO_2/Zn at 273 K.³, green signal represents CO_2 signal 1, orange signal represents CO_2 signal 2 and purple signal represents free CO_2 .

For the $\text{CO}_2 + \text{D}_2\text{O}$ co-adsorbed samples, the SSNMR line shapes have the same features as the pure 0.25eq/0.5eq CO_2 loaded samples (see **Figure 2.8**). When co-adsorbed with water, the isotropic CO_2 appeared earlier at lower temperatures compared to the pure CO_2 loaded samples when the same amount of CO_2 was loaded. Less CO_2 was adsorbed to the framework, suggesting that water has a negative effect on the CO_2 adsorption capability.

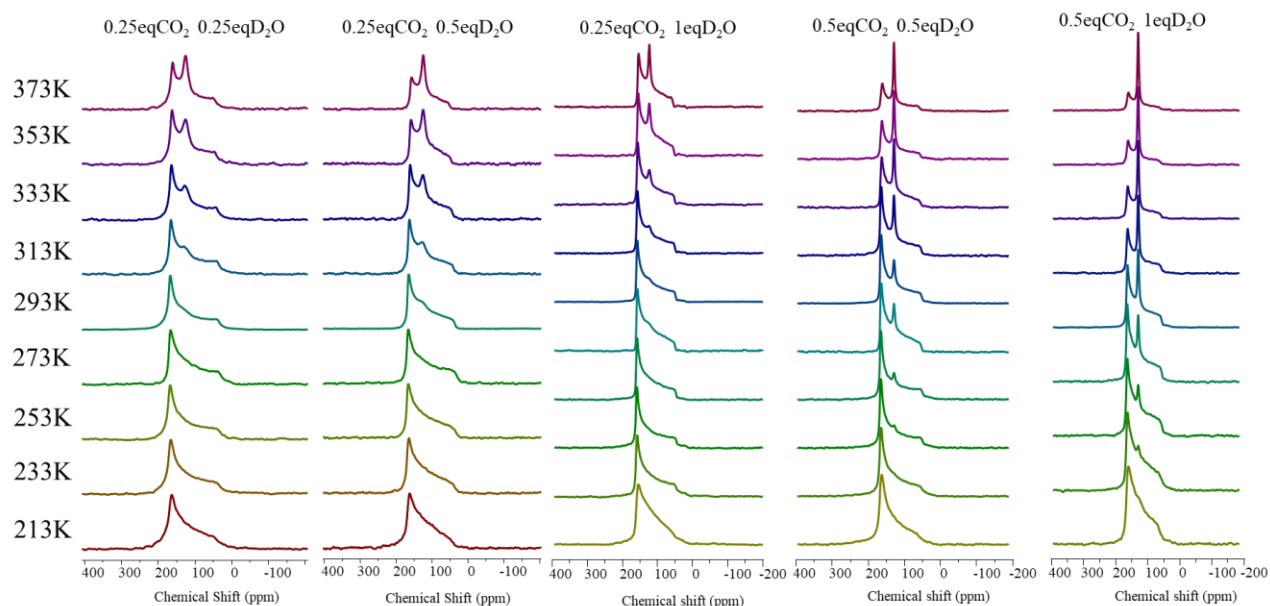


Figure 2.8. Experimental VT static ^{13}C SSNMR spectra of CO_2 at different $\text{CO}_2 + \text{D}_2\text{O}$ co-adsorbed loadings from 213 K to 373 K.

Detailed spectral analysis for the relatively mobile CO_2 signal (CO_2 signal 1) was carried out for all samples between 213 - 373 K. The experimental patterns were first simulated with Wsolids software package³ to extract the CSA parameters. After obtaining the CSA parameters, EXPRESS⁴ was used to simulate the effects of different types and rates of motions (**Figure 2.9**). **Table 2.2.** presents a sample simulation data extracted from Wsolids and EXPRESS.^{3,4} The simulation parameters for samples with 0.25eq CO_2/Zn and 0.25eq $\text{CO}_2 + 0.25\text{eq D}_2\text{O}$ loading are similar (**Table 2.2**). With decreasing temperature, the span slightly increases.

EXPRESS software package⁴ was used in order to obtain more detailed information on the types of motion and motional rates on the adsorbed CO_2 (**Figure 2.9**). The simulation results indicate that CO_2 exhibits 2 types of motions: (1) C_2 hopping motion and (2) C_3 wobbling motion. The delocalized C_2 hopping motion (see **Figure 2.10 (a)**) is 180° rotation about a C_2 axis with an angle β . The C_3 wobbling motion corresponds to CO_2 local rotation modeled by its C_3 axis at angle α (see **Figure 2.10 (b)**). Based on the simulation results from EXPRESS (**Table 2.2.**), it can be found that the span is affected by the wobbling motions of CO_2 , while the skew is affected by the hopping motions. The larger the C_3 wobbling angles, the smaller the span. The larger the C_2 hopping angles, the smaller the skew. The angle of motion changes as a function of temperature. Additionally, the

CO₂ molecules were assumed to be adsorbed at the hydrogens on the NH₂ groups on the benzylic dicarboxylate group.

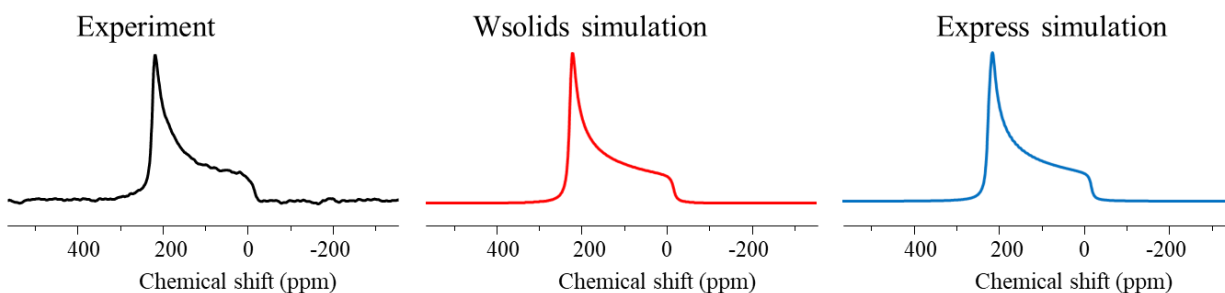


Figure 2.9. Experimental and simulated^{3,4} VT ¹³C static SSNMR spectra of CO₂ at 273 K with 0.25eq CO₂/Zn loading for ZTP-3.

Table 2.2. VT ¹³C static SSNMR simulation parameters^{3,4} of CO₂ signal 1 for 0.25eq CO₂/Zn and 0.25eq CO₂ + 0.25eq D₂O loading.

0.25eq CO ₂						
Temperature (K)	Ω (ppm)	κ	angle of motion β ($^{\circ}$) (C ₂ hopping)	jump rate	angle of motion α ($^{\circ}$) (C ₃ wobbling)	jump rate
213	188	1	9	1×10^7	32	1×10^7
233	194	0.94	11	1×10^7	31	1×10^7
253	181	0.95	11	1×10^7	32	1×10^7
273	171	0.95	11	1×10^7	33	1×10^7
293	160	0.96	11	1×10^7	34	1×10^7
313	150.4	0.955	11	1×10^7	35.5	1×10^7
333	139.6	0.94	12	1×10^7	37.5	1×10^7
353	132	0.93	12	1×10^7	38.5	1×10^7
373	127	0.93	12	1×10^7	39	1×10^7

0.25eq CO ₂ + 0.25eq D ₂ O						
temperature (K)	Ω (ppm)	κ	angle of motion β (°) (C ₂ hopping)	jump rate	angle of motion α (°) (C ₃ wobbling)	jump rate
213	137	0.86	15	1×10^7	38	1×10^7
233	141	0.89	14	1×10^7	38	1×10^7
253	142	0.92	13.5	1×10^7	38	1×10^7
273	140.5	0.93	13.5	1×10^7	38	1×10^7
293	139	0.93	13.5	1×10^7	38	1×10^7
313	133	0.93	13.5	1×10^7	38.5	1×10^7
333	130	0.92	13.5	1×10^7	38.5	1×10^7
353	126	0.9	14	1×10^7	39	1×10^7
373	121	0.9	14	1×10^7	39.5	1×10^7

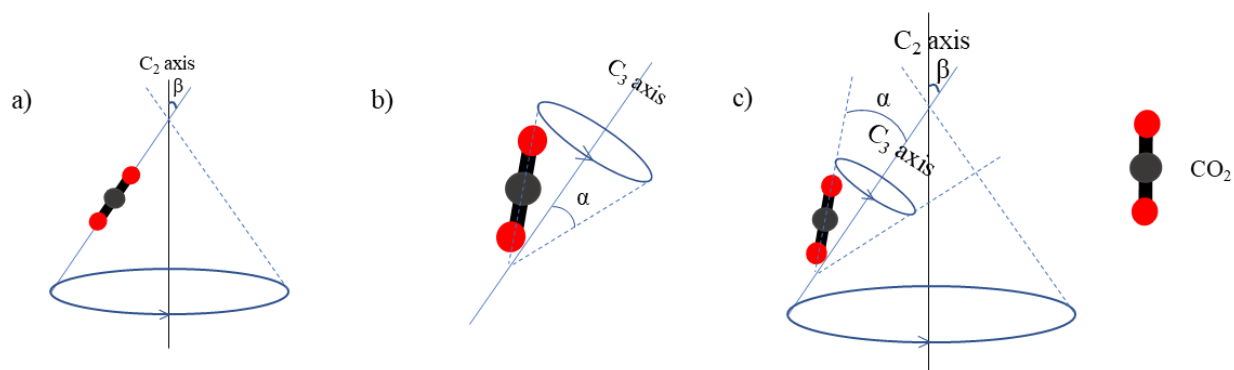


Figure 2.10. a) C₂ hopping motion of CO₂ molecule of 180° rotation about the C₂ axis scheme, b) C₃ wobbling motion scheme of CO₂, c) combined wobbling and hopping motions.

By looking at the simulation data in **Table 2.3**, it was found that the isotropic CO₂ signal appears at a lower temperature when D₂O was introduced into the system. At 0.25eq CO₂ loadings, when 0.25eq D₂O is introduced, the relative intensity of free CO₂ with respect to the adsorbed CO₂ also

increases (**Table 2.3**), leading to a decreased CO₂ adsorption capability at 313 - 373 K. However, at the same CO₂ loading, when 0.5eq D₂O is present in the system, the relative signal intensity of free CO₂ is lower than the sample loaded with less D₂O at 353 - 373 K (**Table 2.3**), indicating a possible increase in CO₂ uptake capacity. This could be due to the increase in D₂O introduction forcing the CO₂ to have a closer contact with the framework, resulting in more interactions. When more water was added to the system (0.25eq CO₂ + 1eq D₂O), the relative intensity of free CO₂ eventually increased (**Table 2.3**), indicating a decrease in CO₂ adsorption capacity.

Table 2.3. Free CO₂ relative signal intensities at different loadings

Temperature (K)	Relative intensity (%)			
	0.25eq CO ₂	0.25eq CO ₂ + 0.25eq D ₂ O	0.25eq CO ₂ + 0.5eq D ₂ O	0.25eq CO ₂ + 1eq D ₂ O
313	NA	1.2	NA	4.4
333	NA	2.1	0.6	7.5
353	2.5	4.7	2.0	13
373	5.3	8.8	4.0	18.4

0.5eq CO₂/Zn loaded samples are found to have similar results as the 0.25eq CO₂/Zn loaded samples (**Figure 2.6**). However, for the co-adsorbed samples, the increase of CO₂ uptake was not observed when water was introduced to the framework. Increase in water loadings results in decrease of CO₂ adsorption. Interestingly, the ¹³CO₂ adsorption signal for all the co-adsorbed samples were all narrower than pure CO₂ loaded sample. Indicating that CO₂ molecules were more mobile with the introduction of water.

The spectra of 0.75eq CO₂/Zn loaded samples also have similar features as the 0.25eq CO₂ and 0.5eq CO₂ loadings, except that a broad adsorption signal (CO₂ signal 2) with isotropic chemical shift at 125 ppm was found (see **Figure 2.7** orange signal). The breadth of the signal suggests that a more restricted motion (CO₂ signal 2) compared to CO₂ signal 1 (see **Figure 2.7** green signal) could be present within the cage, however, no further motional information can be extracted from simulation.

For most of the cases, the addition of water resulted in a reduction in CO₂ adsorption. Overall, the adsorbed CO₂ motional behaviors were not affected significantly by the introduction of water. To have a better understanding of the general picture, ²H VT SSNMR were conducted.

2.3.3. Static ²H variable temperature (VT) SSNMR

The majority of static ²H VT SSNMR spectra at different pure D₂O loadings contain 2 signals as depicted in **Figure 2.11**. The spectra consist of (1) a narrow axially symmetric pattern from adsorbed D₂O, and (2) a very broad pattern from -ND₂. The -ND₂ pattern arises from the deuterium exchange between NH₂ group on the framework and the D₂O from the guest molecules. We did not analyze the spectrum due to -ND₂ since the focus of the study is to investigate the guest molecules motions within the MOF.

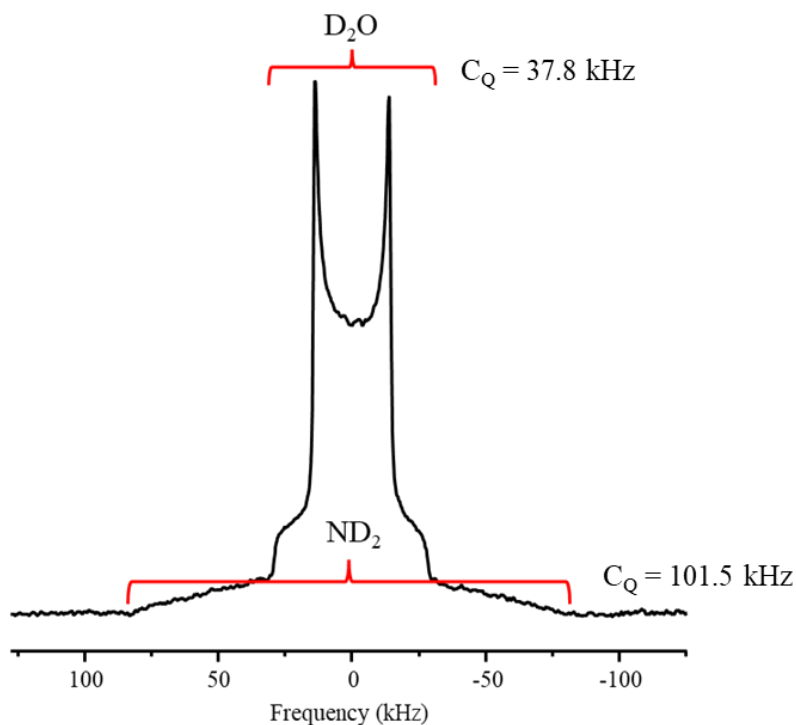


Figure 2.11. Experimental ²H static SSNMR spectrum of D₂O at 373 K with 0.5eq D₂O/Zn showing both D₂O and ND₂, the narrow signal from D₂O ($C_Q = 37.8$ kHz) superimposes on the broad signal with low intensity from ND₂ ($C_Q = 101.5$ kHz) in the MOF.

According to the static VT ²H spectra of pure D₂O adsorbed in the MOF with the pattern depicted in **Figure 2.11**, the -ND₂ signal was observed at all temperatures with a low intensity. From

temperature 233 K to 373 K for all loadings, the line shapes are dominated by a narrow signal which has a much smaller breadth compared to the pattern of rigid D₂O (**Figure 2.12, 2.13**), implying that the D₂O adsorbed in the framework has high mobility. The overall pattern from 173 K to 373 K are very similar for samples with 0.25eq and 0.5eq D₂O/Zn loadings, except that 0.5eq sample has a slightly narrower breadth, inferring the D₂O motions have very little difference for both loadings. The line shapes from 233 K to 373 K for a given loading are in the fast motion regime and are almost identical, indicating that the temperature within this range has little effect on changing the D₂O motions. However, the line shape at 213 K starts to lose its characteristic of relatively mobile narrow pattern, a broader pattern of rigid water begins to emerge, suggesting that the motional rate has been reduced significantly. When the temperature is lowered to 173 K, the narrow line shape is no longer observable, the mobility of D₂O is greatly reduced, ND₂ and rigid D₂O mainly contribute to the overall line shape.

The ²H VT static SSNMR spectra for 1.0eq D₂O/Zn sample show distinctly different patterns in the temperature range of 233 K - 373 K compared to the lower loadings (**Figure 2.13**). The overall breadth of the pattern is also significantly narrower. These results suggest that not only the mobility has significantly increased, the D₂O motions are also different at this loading. This results from weakened interaction of D₂O with the framework due to the interaction among water molecules at a larger amount of D₂O loading. From 233 K - 373 K, a narrower D₂O signal ($C_Q = 17$ kHz) in the fast regime is shown from the 1.0eq spectrum, the C_Q for this signal is very small and cannot be simulated based on its motions, which suggests that this signal results from the interaction among the D₂O molecules; at higher loadings, the line shapes were more affected by the interaction among D₂O molecules.⁷ At 173 K - 213 K, the spectra show very similar features as the patterns for lower loadings, representing the ND₂ and rigid D₂O motions (**Figure 2.12**).

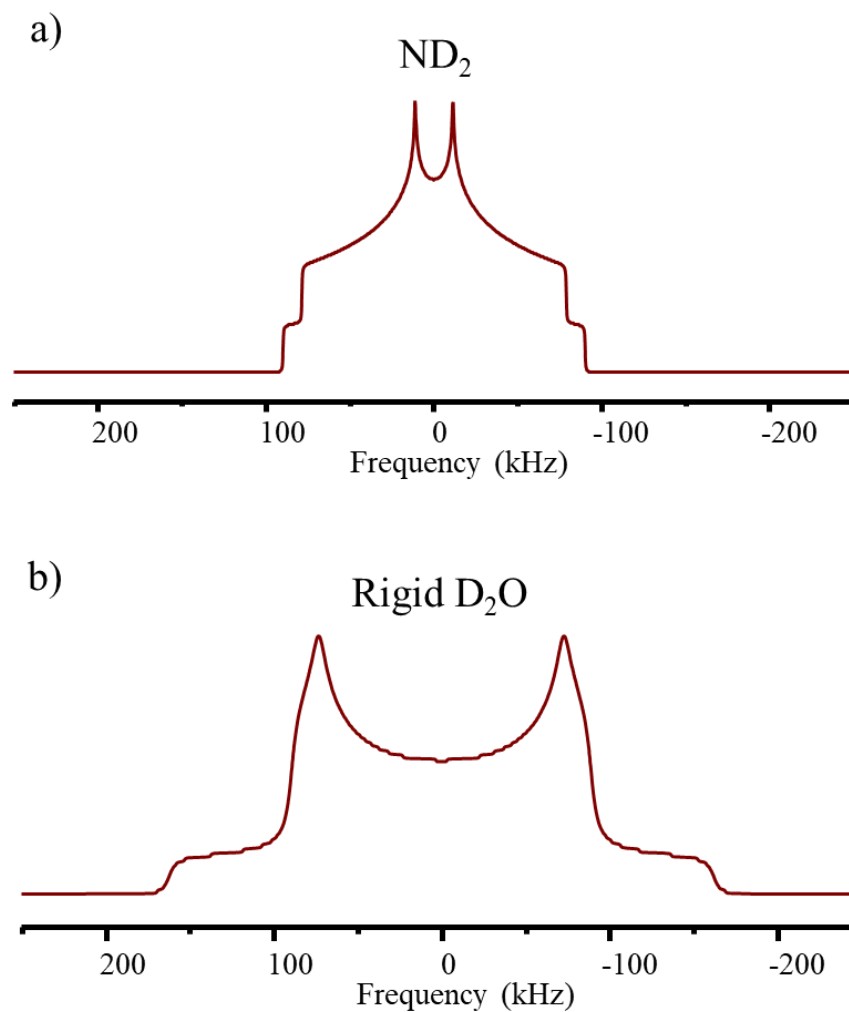


Figure 2.12. Simulated pattern of a) ND₂ ($C_Q = 120$ kHz, $\eta_Q = 0.75$) and b) rigid D₂O ($C_Q = 216$ kHz, $\eta_Q = 0.1$) at 220K.⁸

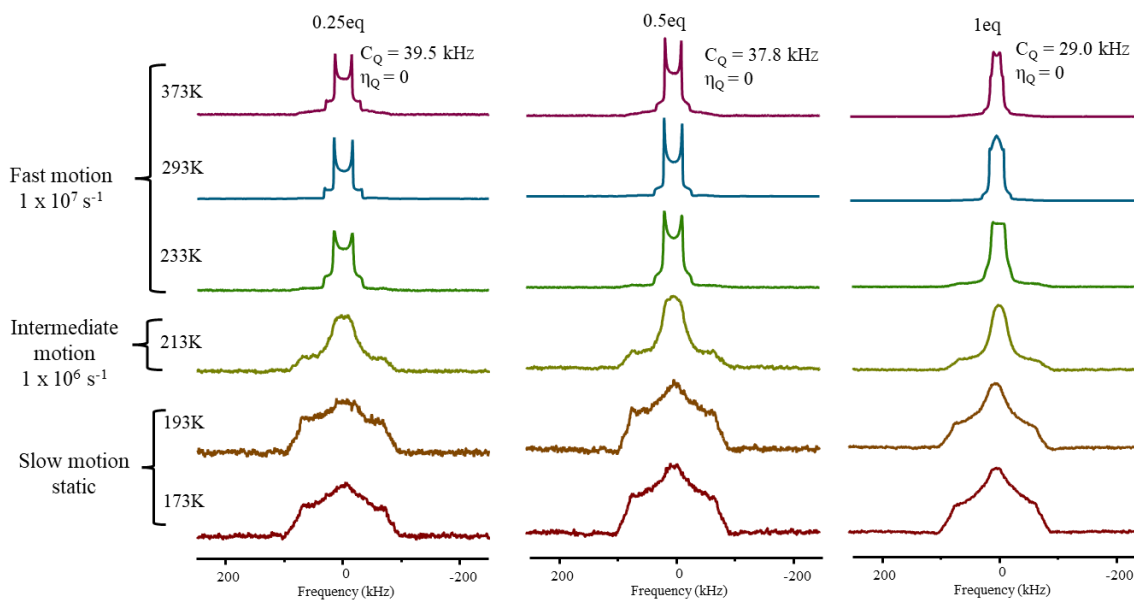


Figure 2.13. Experimental VT ^2H static SSNMR from 173 K to 373 K loaded with 0.25eq, 0.5eq and 1eq $\text{D}_2\text{O}/\text{Zn}$

^2H VT SSNMR spectra of samples co-adsorbed with D_2O and CO_2 are also obtained to explore the effect of CO_2 on the adsorption of D_2O . 0.25eq CO_2 + 0.25eq D_2O and 0.25eq CO_2 + 0.5eq D_2O loaded samples were found to have similar patterns with slightly different breadth and shape (**Figure 2.14**). Most of the patterns exhibit almost identical features compared to the pure D_2O loaded samples, with one strong signal of relatively mobile water and one weak signal from the - ND_2 . However, when the temperature goes down to 233 K, the water becomes less mobile. The overall pattern was contributed by rigid water and ND_2 .

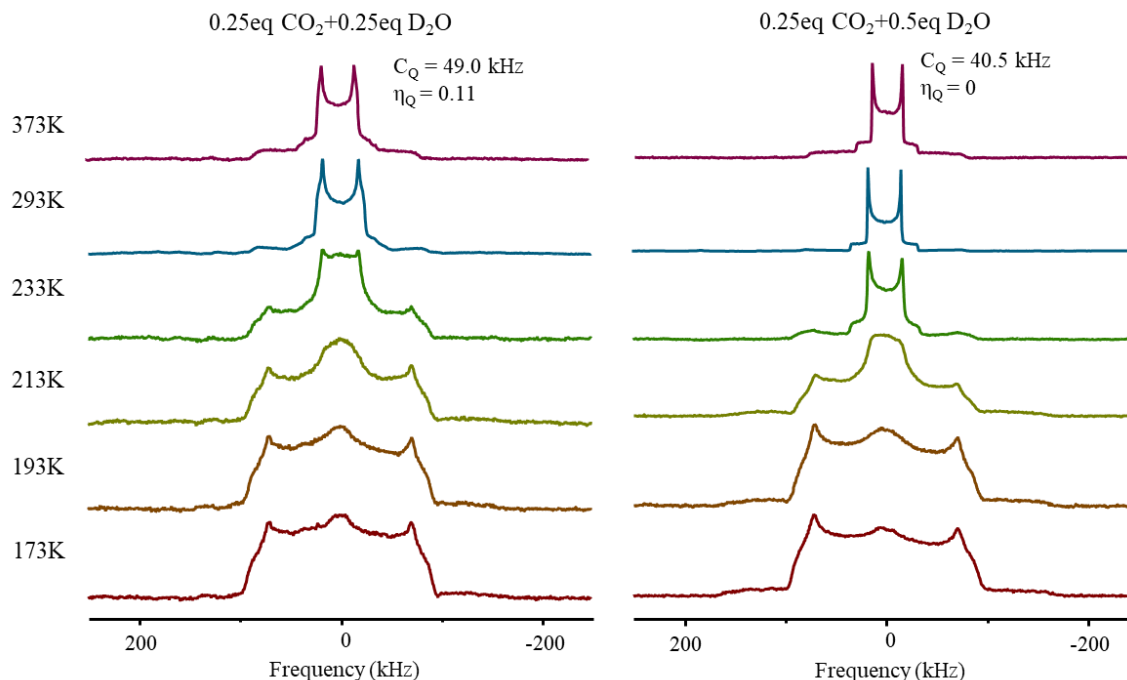


Figure 2.14. Experimental VT ^2H static SSNMR spectra from 173 K to 373 K loaded with 0.25eq CO_2 + 0.25eq D_2O and 0.25eq CO_2 + 0.5eq D_2O .

Detailed spectral analysis for the relatively mobile D_2O signal (D_2O signal 1) was carried out for the 0.5eq D_2O loaded and 0.25eq CO_2 + 0.5eq D_2O co-adsorbed samples between 233 - 373 K. The experimental pattern was first simulated with Wsolids software package³ to extract the quadrupolar coupling constant C_Q and the asymmetric parameter η_Q (**Figure 2.15.**). The simulation parameters for both samples are very similar (**Table 2.4.**). The quadrupolar coupling constant (C_Q) slightly increases with decreasing temperature for both samples. Since C_Q is a measure of the magnitude of quadrupolar interaction, the larger the C_Q , the stronger the quadrupolar interaction. Since the D_2O experiences molecular motions in the framework, the motions partially average the quadrupolar interaction, resulting in smaller C_Q values overall. The less mobile D_2O signal (rigid D_2O) in the co-adsorbed sample between 173 - 213 K was also analyzed using Wsolids³ (**Table 2.4.**), and it has a C_Q value similar to that of rigid water.

EXPRESS software package⁴ was used in order to obtain more detailed information on the types of motion and motional rates on the adsorbed D_2O (**Figure 2.15.**). The simulation results indicate that for all the narrow signals, D_2O exhibits 2 types of motions: (1) π -flipflop motion and (2) 4-site jumping motion. The π -flipflop motion (see **Figure 2.16.(a)**) is 180° rotation about the

molecular C₂ axis of D₂O bisecting the D-O-D angle (109.46°). The 4-site jumping motion corresponds to D₂O jumps among the four equivalent sites in the same plane involving 4 nitrogens from the benzylic dicarboxylate group (see **Figure 2.16.(b)**). The angle of motion only slightly varies with temperature (**Table 2.4.**). D₂O signal is found to be in the fast motion regime with a higher mobility.

Table 2.4. VT ²H static SSNMR spectra simulation parameters of D₂O signal 1 for 0.5eq D₂O/Zn and 0.25eq CO₂ + 0.5eq D₂O loading.

0.5eq D ₂ O					0.25eq CO ₂ + 0.5eq D ₂ O				
temperature (K)	C _Q (kHz)	η _Q	angle of motion β (°) (4 site jumping)	jump rate	temperature (K)	C _Q (kHz)	η _Q	angle of motion β (°) (4 site jumping)	jump rate
233	42	0	42	1 × 10 ⁷	233	45.9	0	44	1 × 10 ⁷
253	42	0	42	1 × 10 ⁷	253	45.9	0	44	1 × 10 ⁷
273	41.5	0	41.5	1 × 10 ⁷	273	44.3	0	43	1 × 10 ⁷
293	42	0	42	1 × 10 ⁷	293	44.8	0	43.5	1 × 10 ⁷
313	41	0	41	1 × 10 ⁷	313	44	0	43	1 × 10 ⁷
333	40.5	0	40.7	1 × 10 ⁷	333	43.2	0	42.3	1 × 10 ⁷
353	39	0	40	1 × 10 ⁷	353	42	0	42	1 × 10 ⁷
373	37.8	0	39.5	1 × 10 ⁷	373	40.5	0	40.7	1 × 10 ⁷

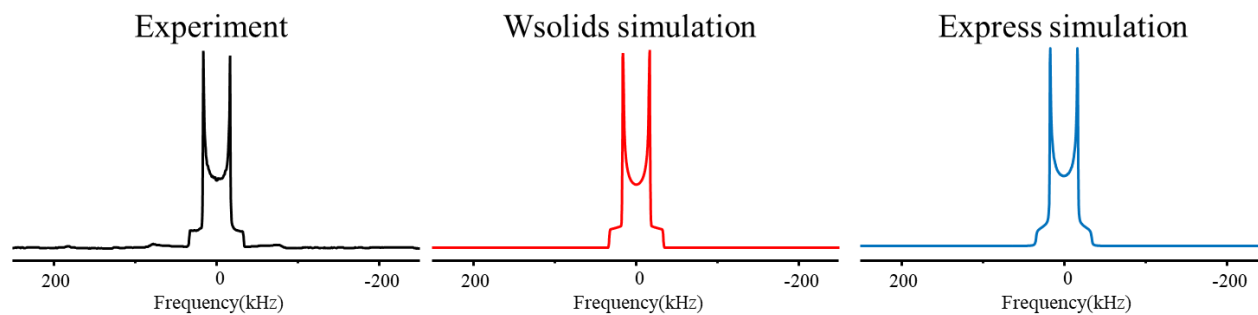


Figure 2.15. Experimental and simulated^{3,4} VT ^2H static SSNMR spectra at 273 K with 0.25eq CO_2 + 0.5eq D_2O loading.

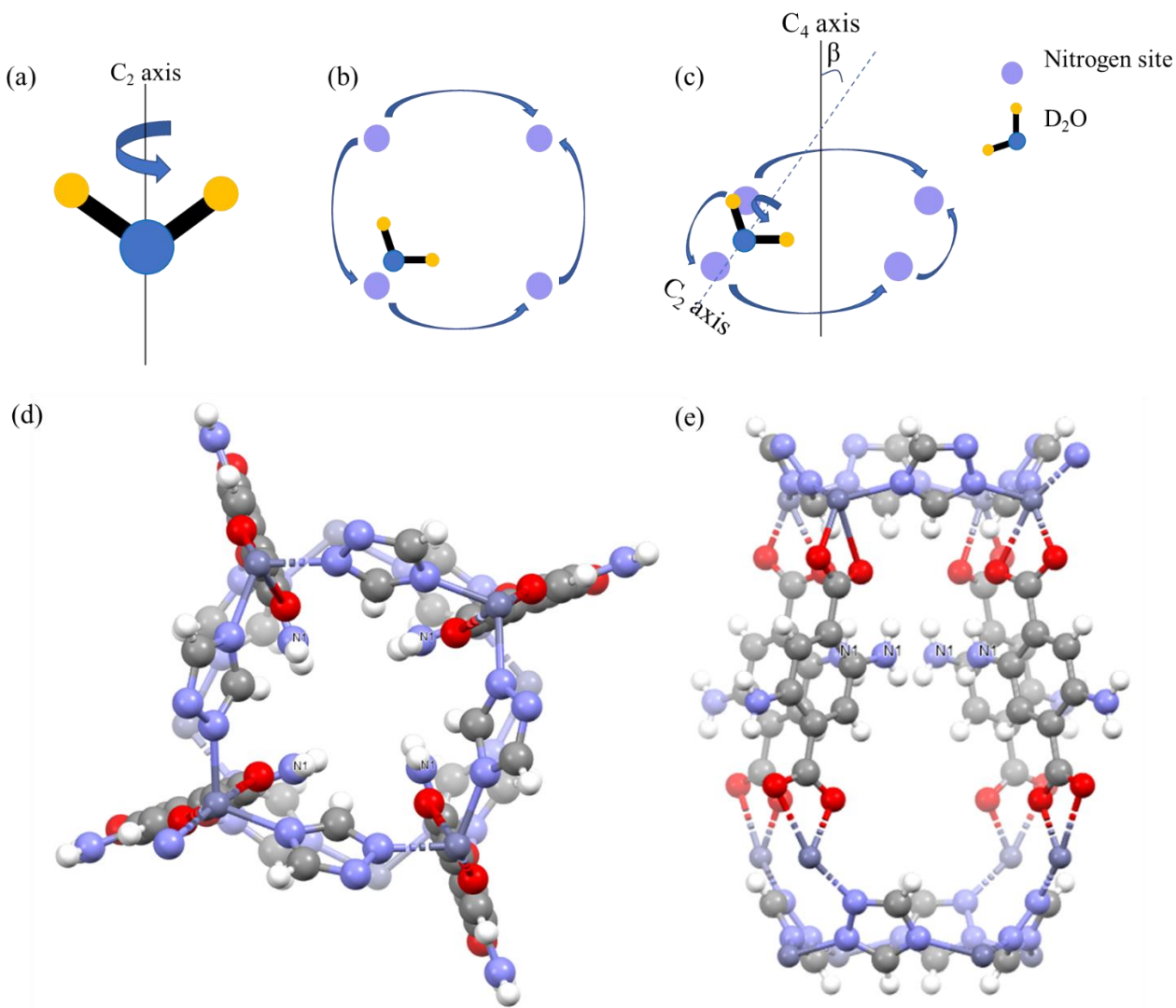


Figure 2.16. a) π -flipflop motion of 180° rotation about the molecular C_2 axis of D_2O scheme. 4-site jumping motion scheme of D_2O b) C_4 axis pointing out of paper with 4-nitrogen rings in the paper, c) C_4 axis parallel to the paper with ring perpendicular to the paper, (d) top view of ZTP-3 cages with nitrogen adsorption sites labeled as N1, (e) side view of ZTP-3 cages with nitrogen adsorption sites labeled as N1.

Loadings of 0.25eq D_2O , 1.0eq D_2O , 0.25eq CO_2 + 0.25eq D_2O , 0.25eq CO_2 + 1eq D_2O , 0.5eq CO_2 + 0.5eq D_2O , and 0.5eq CO_2 + 1eq D_2O are also found to have the narrow line shape of adsorbed D_2O undergoing π -flipflop motion and 4-site jumping motion within the framework at 233 K - 373 K. A broad signal of ND_2 ($C_Q = 122$ kHz) is found in all D_2O loaded samples at all

temperatures. The broad signal of $C_Q = 200$ kHz resulting from rigid D_2O between 173 K - 213 K is found in all the co-adsorbed samples.

Although the breadths of the signals were all similar for pure and co-adsorbed loadings, the symmetry of the adsorption varies with different loadings (**Table 2.5**). It can be seen that for all pure loadings, $\eta_Q = 0$. η_Q was also zero when 0.25eq $CO_2 + 0.5eq D_2O$ or 0.25eq $CO_2 + 1eq D_2O$ was loaded in the framework. Indicating that the motional behavior of D_2O in these 3 cases were similar. 0.25eq $CO_2 + 0.25eq D_2O$, 0.5eq $CO_2 + 0.5eq D_2O$ and 0.5eq $CO_2 + 1eq D_2O$ loaded samples have a similar η_Q value ($\eta_Q = \sim 0.1$), which is different from all other loadings. This suggests that D_2O adsorbed in the framework at these loadings was possibly affected by the CO_2 motions. Herein, we propose that the CO_2 and D_2O were adsorbed at the same cage at these specific loadings. While when $\eta_Q = 0$, D_2O motions were not affected significantly by CO_2 , CO_2 and D_2O were possibly adsorbed in separate cages.

Table 2.5. η_Q parameter extracted from 373 K ^2H VT SSNMR for all loadings.

Loading	η_Q
0.25eq D ₂ O	0
0.5eq D ₂ O	0
1eq D ₂ O	0
0.25eq CO ₂ + 0.25eq D ₂ O	0.11
0.25eq CO ₂ + 0.5eq D ₂ O	0
0.25eq CO ₂ + 1eq D ₂ O	0
0.5eq CO ₂ + 0.5eq D ₂ O	0.11
0.5eq CO ₂ + 1eq D ₂ O	0.1

2.3.4. Adsorption scenarios

According to the simulation results, the location and occupation of the guest molecules can be predicted tentatively as the following:

Since the spectra for 0.75eq CO₂ reveals a second peak that was a lot broader than CO₂ signal 1, we propose that this signal could be resulting from a more restricted motion. On the other hand, CO₂ molecules are much larger in size than D₂O molecules, it is less likely for CO₂ to be preferentially adsorbed in the narrower part of the cage. It is predicted that CO₂ was adsorbed at the bottom part of the cage for all the cases except the 0.75eq CO₂ loading.

For 0.25eq CO₂ loading, half of the number of cages were occupied by 1 CO₂ molecule. Only the bottom part of the cage had CO₂ molecules adsorbed. With 0.5eq CO₂ loading, all the cages had one CO₂ molecule adsorbed at the bottom part. And for 0.75eq CO₂ loadings, since there were two signals with very different breadth, CO₂ were adsorbed at a different location. The span of CO₂

signal 1 also increased at the loading compared to 0.5eq CO₂, which suggests that half of the number of cages had 2 CO₂ molecules adsorbed at the bottom part, resulting in a more rigid pattern. The other half had 1 CO₂ molecule adsorbed at the top part. The occupation of the CO₂ molecules for pure CO₂ are depicted in **Figure 2.17**.

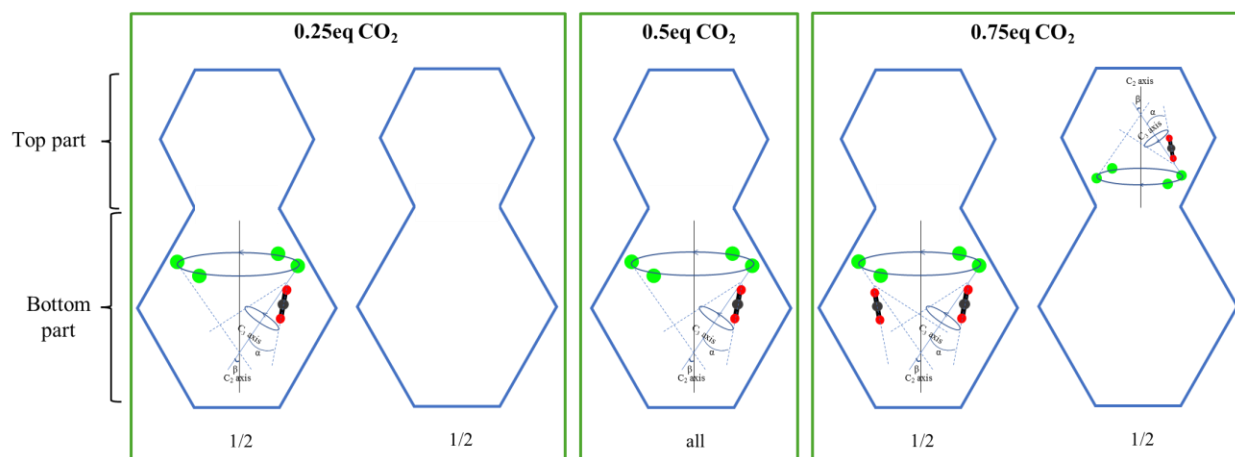


Figure 2.17. Occupation of CO₂ molecules for pure CO₂ loadings.

For pure D₂O loadings, all the D₂O molecules prefer to occupy the top part of the pore. Given that D₂O is a much smaller molecule, shorter distance between the adsorption sites is favored to have a stronger interaction with the framework. 0.25eq D₂O and 0.5eq D₂O loadings tend to have 1 D₂O molecule occupying the top part of the cage, while for 1.0eq D₂O loadings, 2 D₂O molecules were adsorbed at the top part of the cage (**Figure 2.18**).

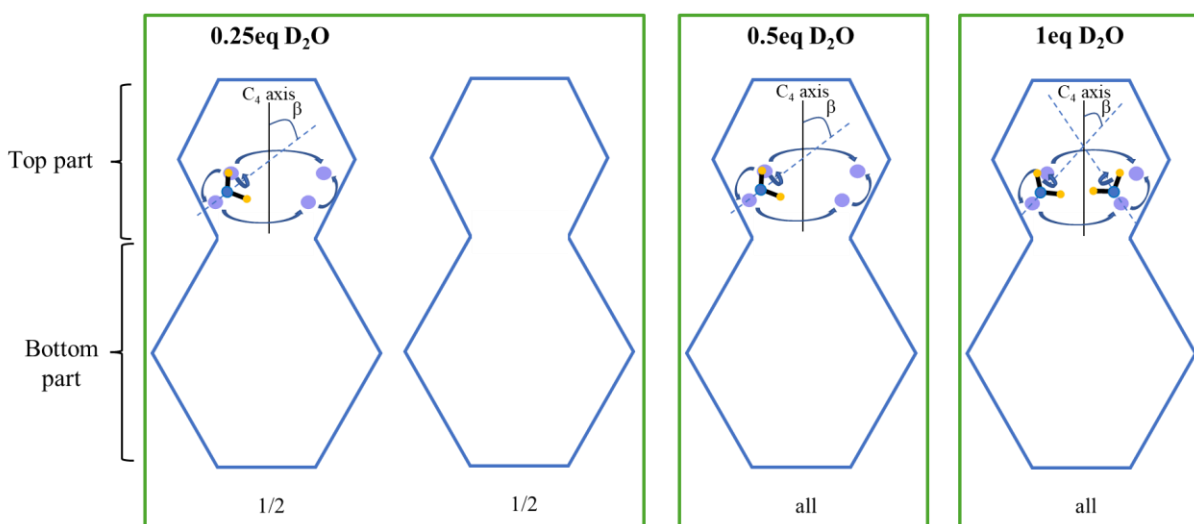


Figure 2.18. Occupation of CO₂ molecules for pure D₂O loadings.

The CO₂ molecules in co-adsorbed samples had very similar adsorption as the pure CO₂ loadings. However, D₂O was adsorbed similarly in some cases, and differently in others (see **Figure 2.19**). For 0.25eq CO₂ + 0.5eq D₂O and 0.25eq CO₂ + 1eq D₂O loadings, the D₂O molecules occupy the top part of the cages that don't contain CO₂. When 0.25eq CO₂ + 0.5eq D₂O was loaded, half of the number of cages had one CO₂ molecule adsorbed at the bottom part, the other half had 2 D₂O adsorbed at the top part. At 0.25eq CO₂ + 1eq D₂O loadings, one CO₂ molecule still occupies half the number of cages. At the same time, the other half had 4 D₂O molecules adsorbed at the same adsorption sites: 2 adsorbed at the top part of the cage, 2 adsorbed at the bottom part. Since all the D₂O molecules were adsorbed on the same amine group, the motions didn't change dramatically. For the other 3 co-adsorption cases, D₂O is proposed to be adsorbed in the same cage as CO₂, resulting in the symmetry change in the ²H static SSNMR pattern.

For most of the co-adsorption cases, there was a decrease in CO₂ adsorption compared to the pure loadings, which could be attributed to overcrowded adsorption sites. Since the D₂O molecules were adsorbed on the nitrogens from the amine group, while CO₂ molecules were adsorbed on the hydrogens from the same amine group, they could be competitive against each other upon co-adsorption. On the co-adsorption ¹³C SSNMR spectra, free CO₂ signals were found to have higher intensities, but free water was not observed from the co-adsorption static ²H SSNMR spectra. This suggests that water has a stronger affinity to the framework compared to CO₂.

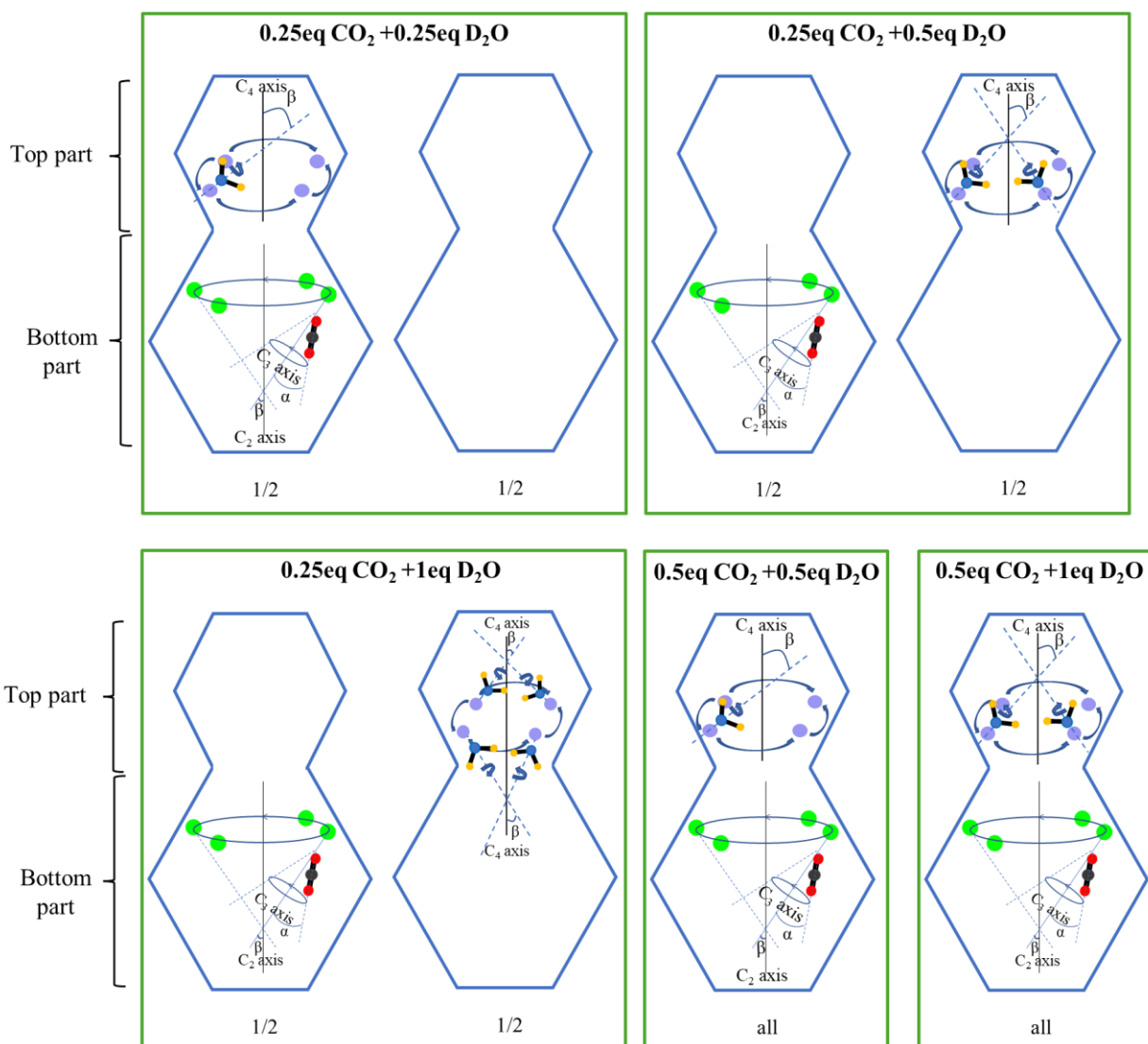


Figure 2.19. Occupation of CO₂ and D₂O molecules for co-adsorption loadings.

2.3.5. MAS SSNMR

The ¹H-¹³C CP MAS SSNMR experiments were conducted on activated and CO₂ loaded samples. However, the CO₂ adsorption signal at around 125 ppm cannot be found on the loaded samples (see **Figure 2.20.(a)**). Only structural signal was observed from the pattern. To confirm that CO₂ was adsorbed in the framework while the CP MAS spectrum was being measured, one-pulse MAS spectrum was also measured after the CP MAS experiment. In the one-pulse spectrum (**Figure 2.20.(b)**), a signal at 124 ppm was observed, indicating that CO₂ was adsorbed in the framework at the time when the CP MAS experiment was taking place. One of the reasons for not observing

the CO₂ signal from the CP MAS spectrum is possibly the large cage size of the framework. When the cage is large, the CO₂ adsorbed to the framework might be far away from the hydrogens on the framework itself. The ¹³C nuclei signal therefore cannot be greatly enhanced through borrowing the signal intensity from the protons. Another explanation for this phenomenon could be attributed to the fast CO₂ motion within the framework. The fast motion of CO₂ averages out the dipole-dipole interaction between the carbon on CO₂ and hydrogen on the framework, weakening the polarization transfer of signal from H to C. Though the CO₂ adsorption cannot be seen on the CP MAS spectra, the structural signal of each carbon from the framework can be assigned, 5 signals were observed for this framework in total (see **Figure 2.20 (c)** for origin of the signal).

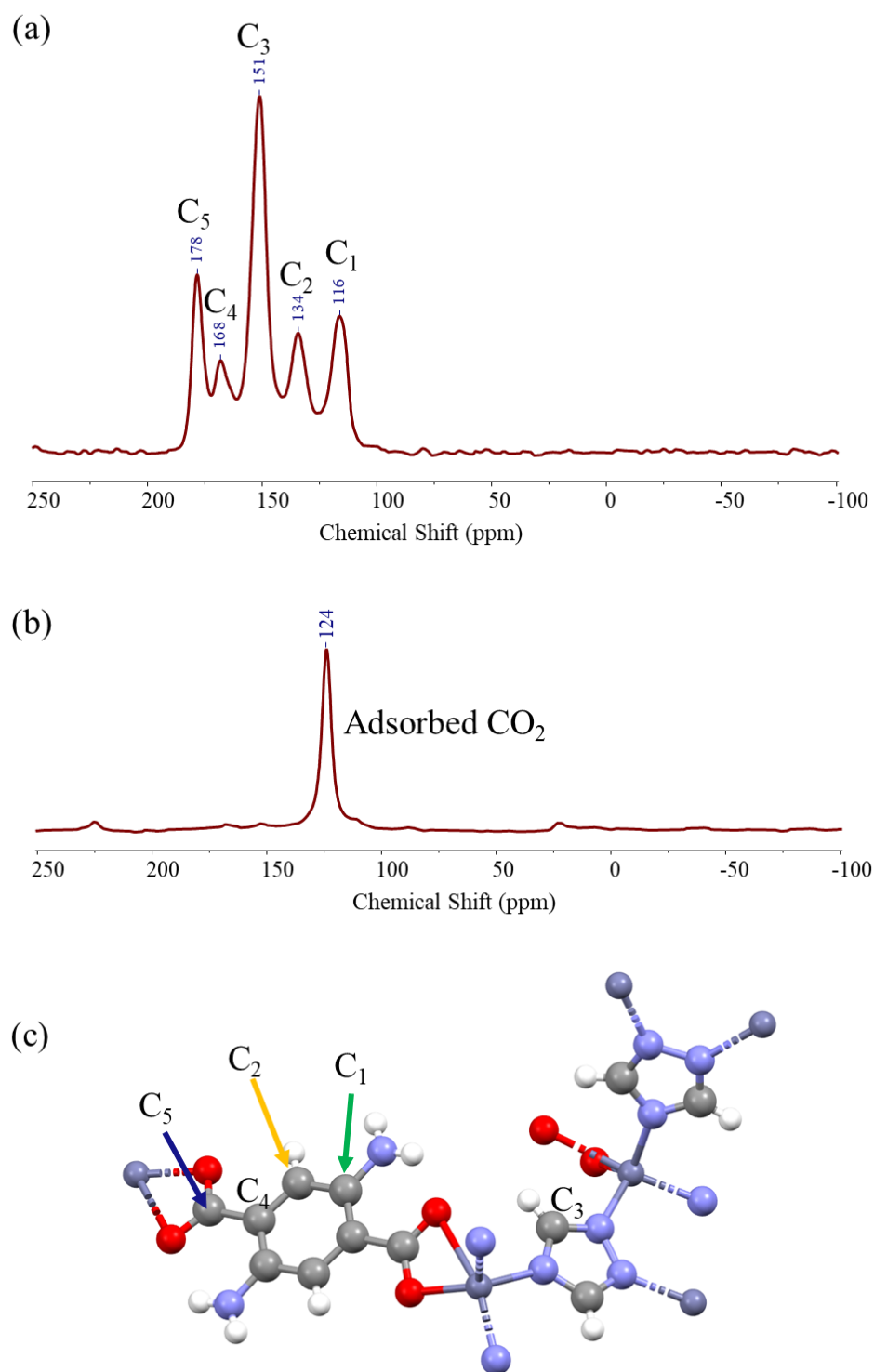


Figure 2.20 (a) ^1H - ^{13}C CP MAS SSNMR for 0.5eq CO_2 loaded ZTP-3. (b) One-pulse ^{13}C MAS SSNMR for 0.5eq CO_2 loaded ZTP-3. (c) Asymmetric carbons on the ZTP-3 structure.

2.4. Summary

The VT static ^2H and ^{13}C SSNMR allow us to probe the co-adsorbed D_2O and CO_2 motions in the ZTP-3. D_2O undergoes both π -flipflop motion and 4-site jumping motion with and without the introduction of CO_2 . Meanwhile, CO_2 undergoes both C_2 hopping motion and C_3 wobbling motion with and without the introduction of D_2O . When pure D_2O is loaded, the ^2H patterns between 233 - 373 K demonstrate one narrow adsorption signal in the fast regime, while rigid D_2O pattern emerges when the temperature is dropped to 213 K.

When pure CO_2 is loaded, one narrow signal representing the adsorption in the bottom part of the cages in fast motion regime is found at all tested temperatures. Upon co-adsorption, ^2H VT static SSNMR produces a broad signal at the slow regime at 173 - 373 K, ^{13}C VT static SSNMR remains the same. Based on the results, it is possible that for most cases, D_2O molecules are adsorbed in the top part. While the CO_2 molecules are adsorbed at the bottom part at pure CO_2 loadings. However, computational simulations will be needed to assist the accuracy of the prediction. For pure CO_2 adsorption, the higher the CO_2 loadings, the higher the amount of CO_2 adsorbed. While interestingly, water was found to have both positive and negative effects on CO_2 adsorption capacity depending on the amount of both CO_2 and D_2O loaded in the framework. Unfortunately, the enhancement of CO_2 adsorption upon water introduction cannot be explained without further analysis. For most of the cases, water reduces the CO_2 adsorption capacity of the ZTP-3 framework due to the competition of the 2 guest molecules at the adsorption site. These results on the guest molecules motions assist the understanding on CO_2 adsorption mechanism with the introduction of water, paving the way for developing and utilizing MOFs for practical carbon capturing purposes.

References

1. Zhai, Q. G.; Bai, N.; Li, S.; Bu, X.; Feng, P. Design of Pore Size and Functionality in Pillar-Layered Zn-Triazolate-Dicarboxylate Frameworks and Their High CO_2/CH_4 and C_2 Hydrocarbons/ CH_4 Selectivity. *Inorg. Chem.* **2015**, *54* (20), 9862–9868.
<https://doi.org/10.1021/acs.inorgchem.5b01611>

2. Facelli, J. C.; Orendt, A. M.; Beeler, A. J.; Solum, M. S.; Depke, G.; Malsch, K. D.; Downing, J. W.; Murthy, P. S.; Grant, D. M.; Michl, J. Low-Temperature Carbon-13 Magnetic Resonance in Solids. 5. Chemical Shielding Anisotropy of the $^{13}\text{CH}_2$ Group. *J. Am. Chem. Soc.* **1985**, *107* (24), 6749–6754. <https://doi.org/10.1021/ja00310a001>.
3. Eichele K., Wasylishen R. E., WSolid1: Solid-State NMR Spectrum Simulation Package, ver. 1.20.21; Universität Tübingen: Tübingen, **2013**.
4. Vold, R. L.; Hoatson, G. L. Effects of Jump Dynamics on Solid State Nuclear Magnetic Resonance Line Shapes and Spin Relaxation Times. *J. Magn. Reson.* **2009**, *198*, 57–72.
5. Stepanov, A. G.; Shegai, T. O.; Luzgin, M. V.; Essayem, N.; Jovic, H. Deuterium Solid-State NMR Study of the Dynamic Behavior of Deuterons and Water Molecules in Solid D₃Pw12O₄₀. *J. Phys. Chem. B* **2003**, *107* (45), 12438–12443. <https://doi.org/10.1021/jp030204c>.
6. Long, J. R.; Ebelhäuser, R.; Griffin, R. G. ^2H NMR Line Shapes and Spin–lattice Relaxation in $\text{Ba}(\text{ClO}_3)_2 \cdot 2\text{H}_2\text{O}$. *J. Phys. Chem. A* **1997**, *101* (6), 988–994. <https://doi.org/10.1021/jp962116g>.
7. Liu, J.; He, X.; Zhang, J. Z. H.; Qi, L. W. Hydrogen-Bond Structure Dynamics in Bulk Water: Insights from: Ab Initio Simulations with Coupled Cluster Theory. *Chem. Sci.* **2018**, *9* (8), 2065–2073. <https://doi.org/10.1039/c7sc04205a>.
8. Wittebort, R. J.; Usha, M. G.; Ruben, D. J.; Wemmer, D. E.; Pines, A. Observation of Molecular Reorientation in Ice by Proton and Deuterium Magnetic Resonance. *J. Am. Chem. Soc.* **1988**, *110* (17), 5668–5671. <https://doi.org/10.1021/ja00225a013>
9. Miyatou, T.; Ohashi, R.; Ida, T.; Kittaka, S.; Mizuno, M. An NMR Study on the Mechanisms of Freezing and Melting of Water Confined in Spherically Mesoporous Silicas SBA-16. *Phys. Chem. Chem. Phys.* **2016**, *18* (27), 18555–18562. <https://doi.org/10.1039/c6cp03111k>.
10. Morcombe, C. R.; Zilm, K. W. Chemical Shift Referencing in Mas Solid State NMR. *J. Magn. Reson.* **2003**, *162* (2), 479–486. [https://doi.org/10.1016/s1090-7807\(03\)00082-x](https://doi.org/10.1016/s1090-7807(03)00082-x).
11. Department of Chemistry. <https://chem.washington.edu/facilities/nmr> (accessed 2024-04-15).
12. Beeler, A. J.; Orendt, A. M.; Grant, D. M.; Cutts, P. W.; Michl, J.; Zilm, K. W.; Downing, J. W.; Facelli, J. C.; Schindler, M. S.; Kutzelnigg, W., Low-Temperature Carbon-13 Magnetic Resonance in Solids. 3. Linear and Pseudolinear Molecules. *J. Am. Chem. Soc.* **1984**, *106* (25), 7672–7676.

Chapter 3. CO₂ adsorption in CALF-20 at different loading levels and temperatures

3.1. Introduction

CALF-20 has gained significant attention in recent years as a carbon dioxide capturing material. It is known for its largescale production capability, high CO₂ adsorption capability, water resistance, and excellent thermal stability.¹ However, the adsorbed CO₂ motional behavior were not investigated for this material. Therefore, in this chapter, CO₂ behavior will be investigated to provide insights for further applications.

3.2. Experimental Section

3.2.1. MOF synthesis CALF-20

As-made CALF-20 sample was synthesized according to previously recorded research procedures with some modifications.¹ All starting materials were used as received without further purification. A mixture of zinc oxalate (ZnC₂O₄, 6.60 g or 43.0 mmol, 99% AA Blocks), and 1,2,4-triazole (C₂H₃N₃, 0.138 g, 72.5 mmol, 99% Alfa Aesar) were dissolved in 66.0 mL methanol (CH₃OH, Fisher Chemical) in an autoclave. The autoclave was sealed and placed in an oven at 180°C for 2 days. White powder was obtained after cooling the sample to room temperature. Vacuum filtration was performed to remove unreacted reagents dissolved in methanol. To perform the vacuum filtration, the powdered sample was washed with methanol, and dried using the vacuum. The pure sample was further collected and placed in an oven and dried at 80°C for 1 day. The resulting white crystal powder sample was referred to as-made CALF-20 sample in this work.

3.2.2. Sample activation

To prepare ZTP-3 for loading guest molecules, activation of the MOF is necessary in order to remove all residual solvent molecules and unreacted chemicals. Since the synthesis of this MOF only used methanol as the solvent, vacuum filtration of the sample is sufficient for the purification of CALF-20, there is no necessity for a solvent exchange process.

The same activation process as mentioned in Chapter 2.2.2. at a different temperature was performed for the activation of CALF-20. The glass tube was placed in a furnace at 150°C for 2 days and cooled to room temperature during the activation process. The end product of the activation gives rise to activated CALF-20.

3.2.3. Powder X-ray diffraction (PXRD) measurements

Powder X-ray Diffraction patterns were performed to measure the diffraction pattern in order to confirm the phase purity and structure identity of the synthesized MOF by comparing the powder pattern of the synthesized product with the ones reported in literature.¹ The PXRD pattern were obtained using a Inel CPS powder diffractometer operating with Cu K α radiation ($\lambda=1.5406$ Å). The powder pattern was collected in the range $5^\circ \leq 2\theta \leq 45^\circ$ at a rate of 10°/min, with a step size of 0.02°.

3.2.4. Thermogravimetric analysis (TGA)

To confirm the completion of solvent removal during the activation process, thermogravimetric analysis of as-made and activated samples was carried out under N₂ atmosphere (40 mL·min⁻¹) using Mettler Toledo AG TGA/SDTA851e instrument. The samples were heated from 30 to 750 °C at a rate of 10 °C·min⁻¹. The TGA graphs were compared to those provided in the literature.¹

3.2.5. CO₂ adsorption

The CO₂ loading process is identical to those on ZTP-3 in Chapter 2.2.5.

3.2.6. Solid-State Nuclear Magnetic Resonance Spectroscopy (SSNMR)

¹³C, and ²H SSNMR experiments were conducted on a 400WB Varian Infinity Plus SSNMR spectrometer operating at a magnetic field of 9.4 T. Variable temperature experiments were performed using a Varian VT temperature control unit.

3.2.6.1. Magic-angle spinning (MAS)

¹H-¹³C cross-polarization (CP) experiments were conducted using a 5mm HXY Varian/Chemagnetics probe at a spinning rate of 10 kHz. ¹H-¹³C CP MAS spectra were acquired using a contact time of 9 ms. The spectra were referenced using solid adamantane set at a chemical

shift of 38.5 ppm.⁷ The 90° pulse width was set to 2.7 μ s, and the pulse delay was set to 2.9 s. Samples were first prepared in L-shaped glass tubes and then transferred to the 5mm rotor in a glove box filled with N₂. Acquisition number varies between 1000-1500 depending on signal intensity. All ¹H-¹³C CP MAS spectra were measured at room temperature.

3.2.6.2. Static SSNMR

Static ²H and ¹³C SSNMR spectra of activated samples of CALF-20 with different CO₂ loadings were measured with Varian Infinity Plus spectrometer equipped with a 9.4 T Oxford Instruments superconducting magnet and a double channel (HX) 5 mm Varian/Chemagnetics static probe.

¹³C static SSNMR spectra were acquired at Larmor frequency $\nu_0 = 100.46$ MHz. The experiment was performed using the DEPTH-echo no dec pulse sequence. The spectra were referenced using liquid ethanol (C₂H₆O) set at a chemical shift of 56.96 ppm.⁸ The parameters used were 90° pulse width = 2.40 μ s; pulse delay = 2.9 s; spectral width = 149.254 kHz; and number of scans = 1000 – 120000, depending on signal intensity.

Static Variable temperature (VT) SSNMR spectra of loaded samples were collected at temperatures between 173 K and 373 K using a Varian VT temperature control unit to probe CO₂ motions in CALF-20. The spectrum at each temperature was not measured until the temperature was stable and the sample reached thermal equilibrium.

3.2.6.3. Spectral simulations

The same parameters were used with the same procedure carried out for ¹³C static powder pattern as in **Chapter 2.2.8.3.**²⁻⁶

3.3. Results and discussion

3.3.1. Characterization

3.3.1.1. PXRD results

The CALF-20 structure is constructed by connecting the Zn-triazolate 2D layers with the oxalate group pillars. The distance between each layer is $\sim 9.5 \text{ \AA}$.¹ The identity and purity of the sample were confirmed by PXRD. The experimental powder pattern matches well with the simulated

pattern as shown in **Figure 3.1**. At higher 2θ range, diffraction pattern could be possibly affected by the present of solvent, resulting in peak shifts.

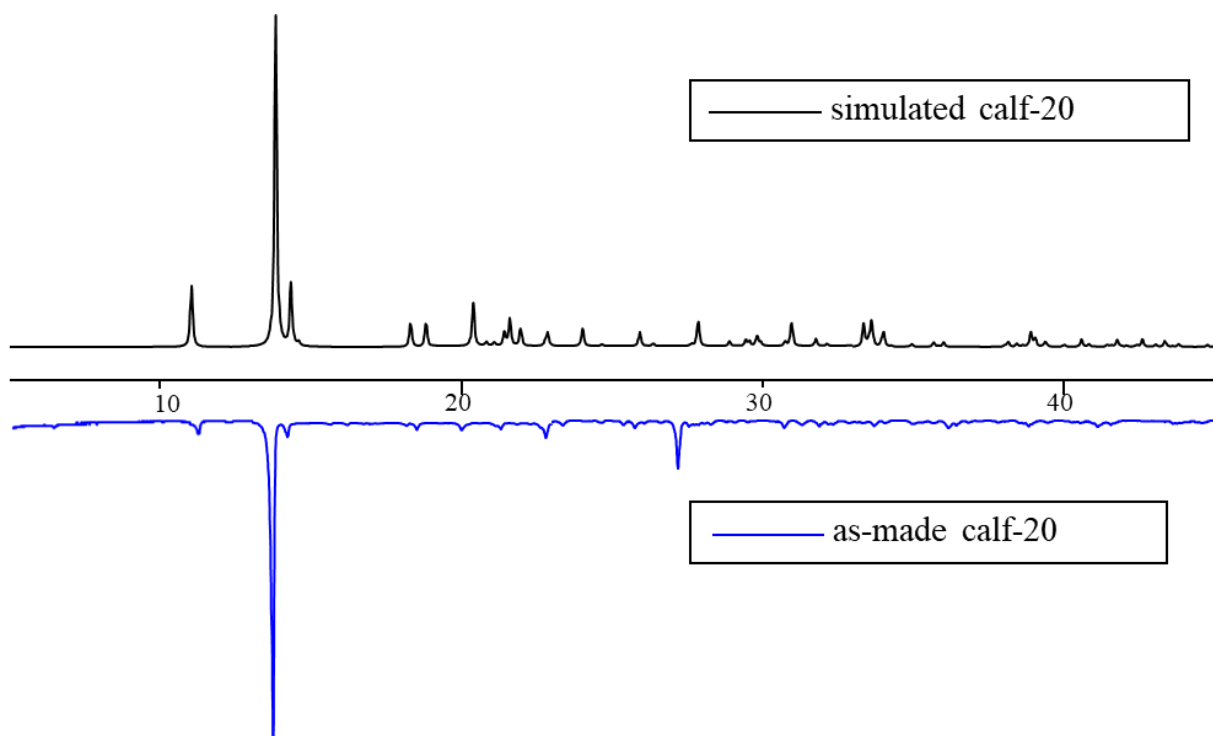


Figure 3.1. Powder X-ray diffraction patterns (PXRD) pattern of CALF-20 and the simulated as-made PXRD pattern was extracted based on the crystal structure provided in the reported literature¹.

3.3.1.2. TGA results

The activation process of CALF-20 was confirmed by temperature-programmed TGA. Activation refers to the process of removing solvents from the pores of the sample to create available binding sites for guest molecules. Therefore, the complete removal of solvents is an indication of successful activation. By monitoring the weight loss of the sample as a function of temperature, 1 weight loss responsible for the solvent desorption of methanol was observed for the as-made sample. The 13% weight loss from 100% to 87% starting from 30°C indicates the departure of methanol (**Figure 3.2**). The weight loss for methanol was not observed in the TGA graph of the activated sample, which indicates the successful activation of the sample. Furthermore, the decomposition

temperature of the as-made and activated sample was found to be around 375°C, which matches well with the reported literature.¹

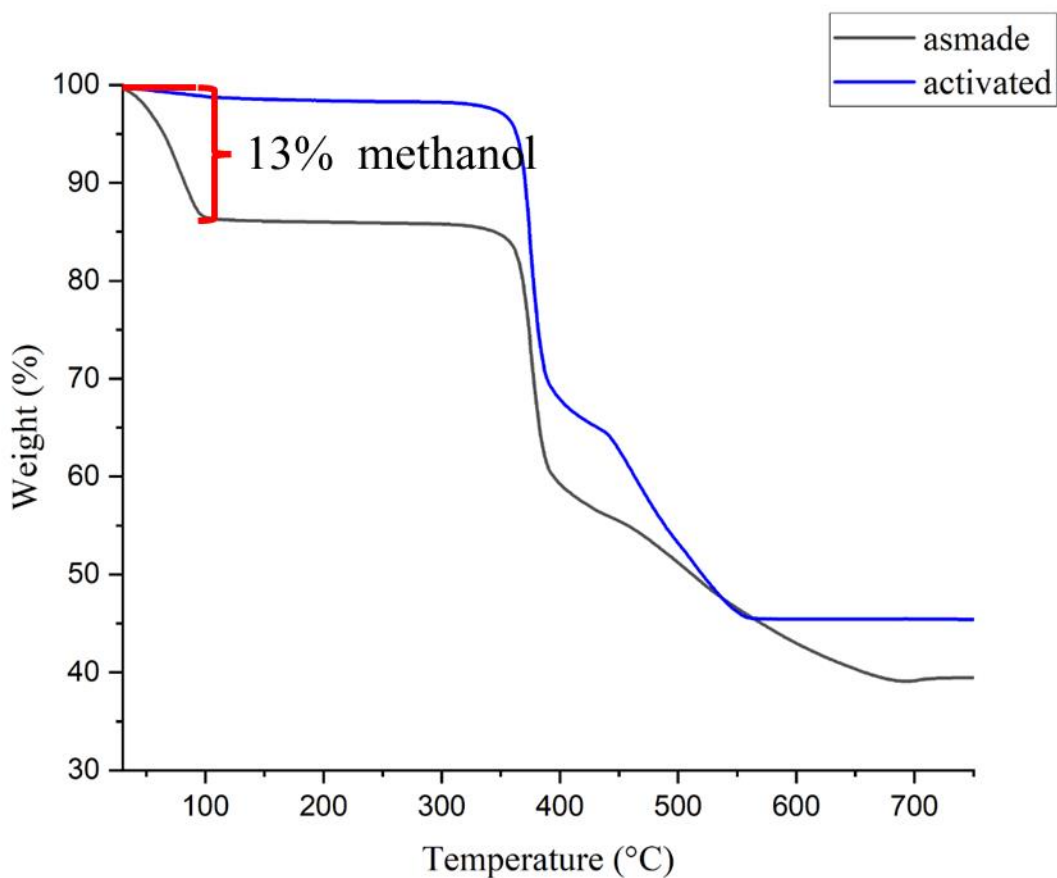


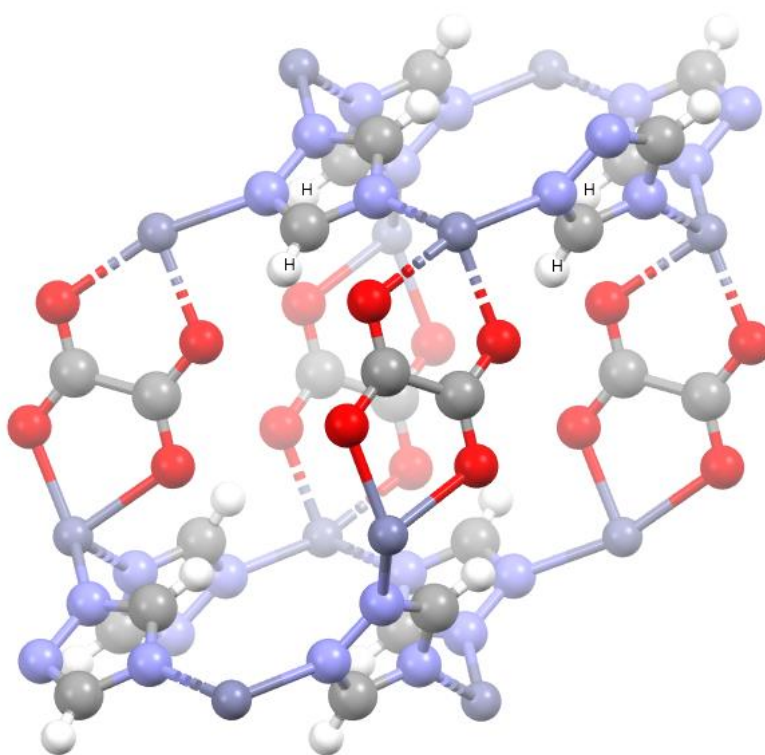
Figure 3.2. Thermogravimetric analysis (TGA) curves of as-made (black curve) and activated (blue curve) CALF-20.

3.3.1.3. Distribution of guest molecules in CALF-20

Based on the symmetry and structural information provided by the literature,¹ each unit cell consists of 2 cages, and 4 Zn ions. Each of the cages would therefore have 2 Zn ions available on average. **Figure 3.3** illustrates the CALF-20 cage. The number of molecules on average for each cage can therefore be calculated as indicated in **Table 3.1**.

Table 3.1. average distribution of guest molecules within CALF-20

# of equivalents per Zn	average # of guest molecules in each cage	
0.25eq	0.5	1 molecule in every 2 cages
0.5eq	1	1 molecule in each cage
0.75eq	1.5	3 molecules in 2 cages

**Figure 3.3.** Side view of CALF-20 cage.

3.3.2. Static ^{13}C variable temperature (VT) SSNMR of CO_2

All of the ^{13}C VT SSNMR spectra at different pure CO_2 loadings contain 1 adsorption signal with an isotropic signal at around 125 ppm as depicted in **Figure 3.4. (a)**. The CO_2 adsorbed for all loadings and all temperatures were relatively mobile compared to rigid CO_2 (**Figure 3.4. (b)**). The

breadth of the signal is very similar for all loadings. The breadth of the pattern increases with increased CO₂ loadings and decreased temperature, suggesting that CO₂ adsorbed in the framework becomes less mobile. It could be observed that the shape of the CO₂ pattern also changes with changes in temperature and loading. This indicates a possible change in motion of CO₂ molecules, which the detailed information could be extracted furtherly through simulations. The experimental static VT ¹³C spectra are shown in **Figure 3.5**. At higher temperatures for the highest loading (0.75eq), a small bump was observed at around 125 ppm. This could be due to that at higher temperatures, the CO₂ adsorbed in the framework became more mobile, when the framework is crowded, part of the CO₂ tends to be desorbed from CALF-20. Which suggests that the framework could at most adsorb 2 molecules in each cage at higher temperatures. Due to experimental restrictions, higher loadings for further investigations were not done.

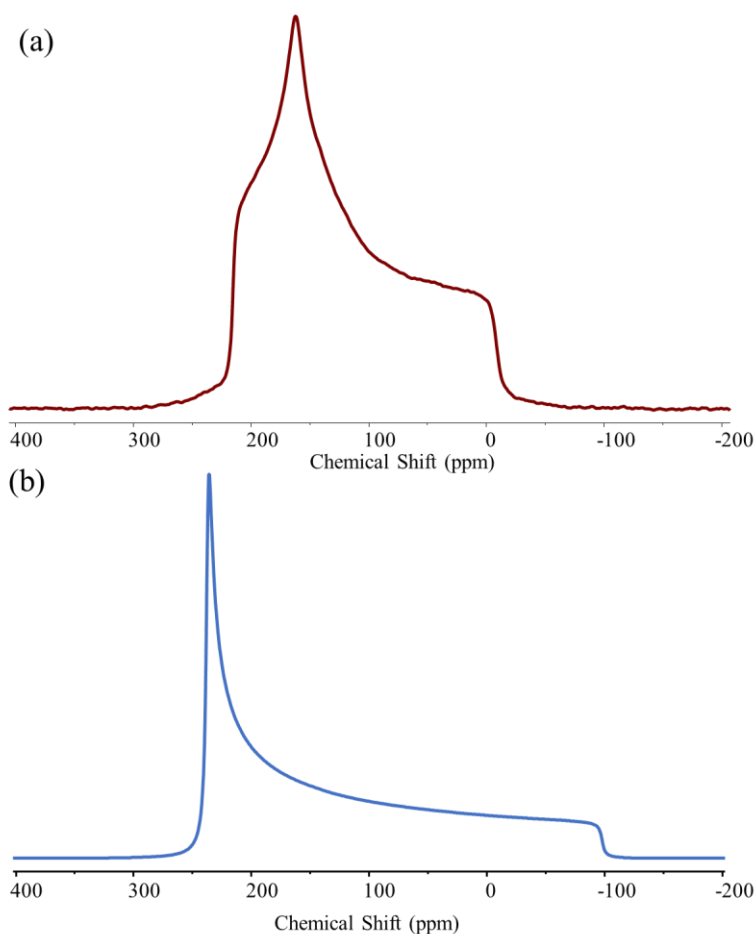


Figure 3.4. static ¹³C SSNMR pattern of a) CO₂ with 0.25eq CO₂/Zn loading for CALF-20 at 173 K ($\Omega = 226$ ppm, $\kappa = 0.52$), b) rigid CO₂ ($\Omega = 335$ ppm, $\kappa = 1$).⁹

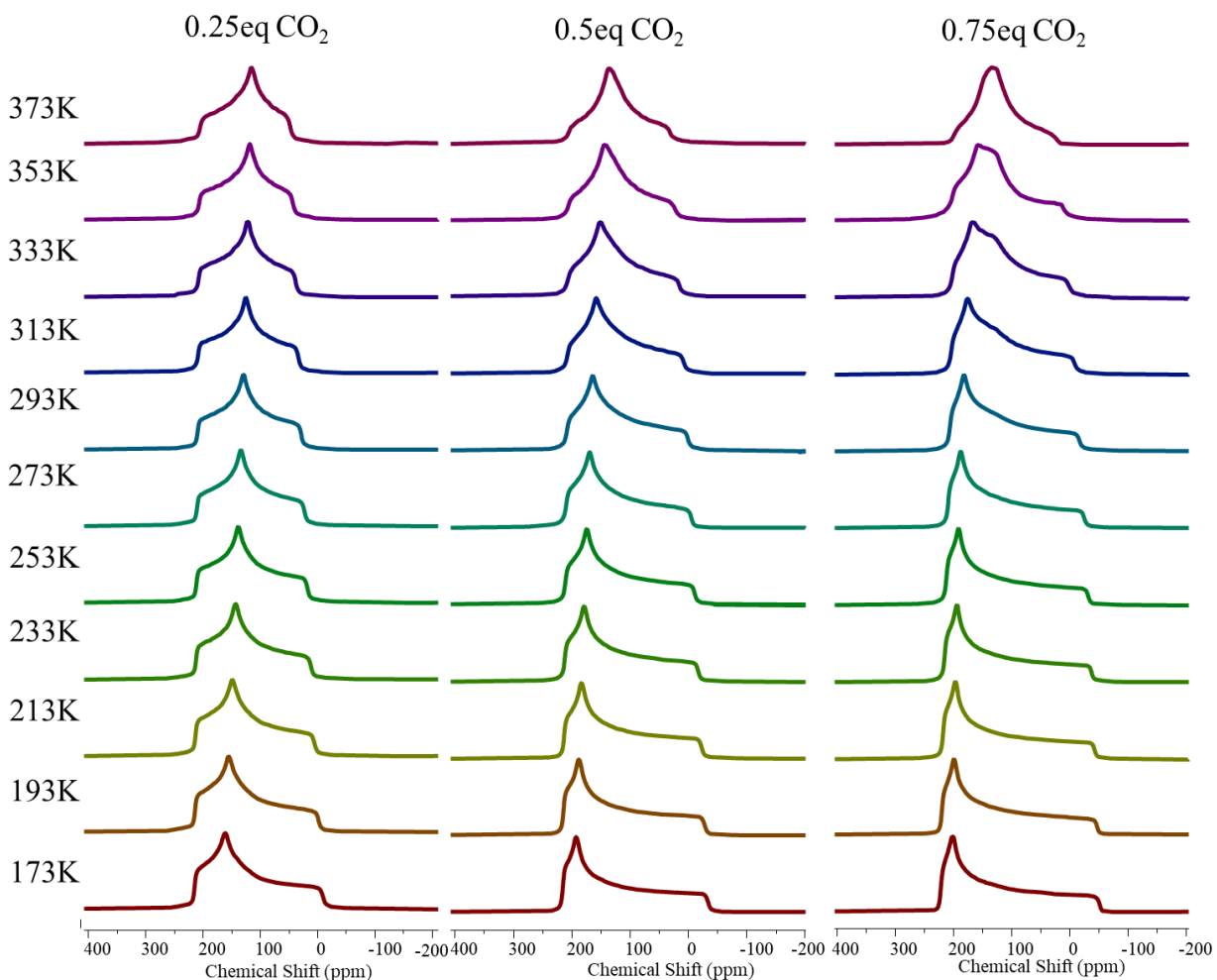


Figure 3.5. Experimental VT static ^{13}C SSNMR spectra of adsorbed CO_2 at various CO_2 loadings and temperatures for CALF-20.

Detailed spectral analysis for the relatively mobile CO_2 signal was carried out for all the tested samples between 173 K - 373 K. The experimental pattern was first simulated with Wsolids software package³ to extract the CSA parameters. After obtaining the CSA parameters, EXPRESS⁴ was used to simulate the effects of different types and rates of motions (**Figure 3.6.**). The simulation parameters for both samples are similar (**Table 3.2.**). With decreasing temperature, the span slightly increases.

EXPRESS software package⁴ was used in order to obtain more detailed information on the types of motion and motional rates on the adsorbed CO_2 (**Figure 3.6.**). The simulation results indicate that for all the CO_2 adsorption signals, CO_2 exhibits 2 types of motions: (1) C_2 hopping motion

and (2) C_3 wobbling motion. The delocalized C_2 hopping motion (see **Figure 3.7.(a)**) is 180° rotation about a C_2 axis with an angle β . The C_3 wobbling motion corresponds to CO_2 local rotation modeled by its C_3 axis at angle α (see **Figure 3.7.(b)**). Based on the simulation results from EXPRESS (**Table 3.2, 3.3, 3.4**), it can be found that the skew (symmetry of the lineshape) is affected by the hopping motions of CO_2 , while the span (breadth of the lineshape) is affected by the wobbling motions. The larger the C_2 hopping angles, the smaller the skew. The larger the C_3 wobbling angles, the smaller the span. The angle of motion changes as a function of temperature. In all three loadings, the higher the temperature, the larger the angle of motion, suggesting that the CO_2 molecules are more mobile at higher temperatures.

Similar results were found at all pure CO_2 loadings. Except that at higher loadings, the breadth of the signal becomes larger, the angle of C_3 wobbling and C_2 hopping were both smaller, meaning that the CO_2 adsorbed in the framework has more restricted motions.

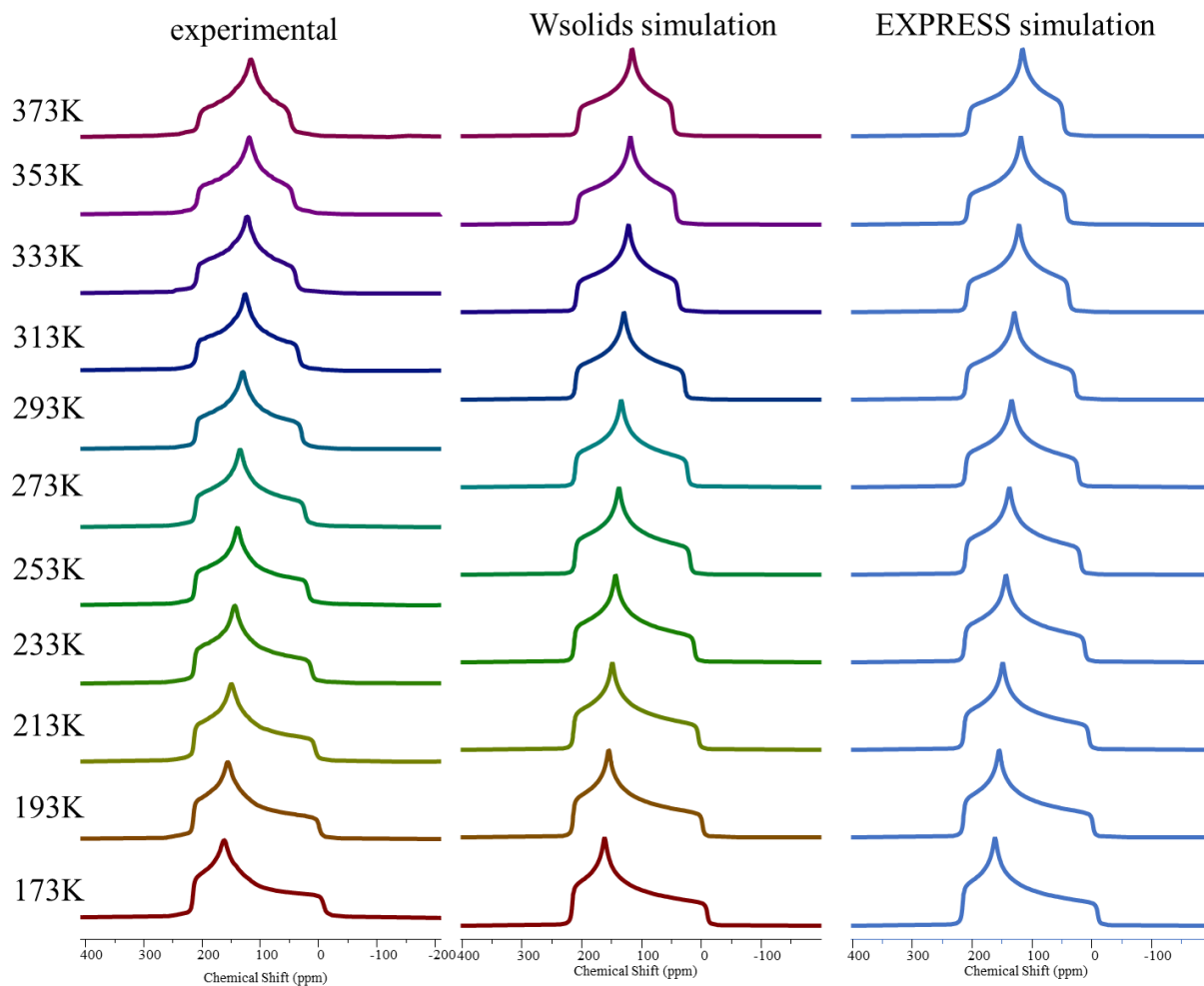


Figure 3.6. Experimental and simulated^{3,4} VT ^{13}C static SSNMR spectra of CO_2 from 173 K to 373 K with 0.25eq CO_2/Zn loading for CALF-20.

Table 3.2. VT ^{13}C static SSNMR simulation parameters^{3,4} for 0.25eq CO_2 loading.

0.25eq CO_2						
temperature (K)	Ω (ppm)	κ	angle of motion β ($^\circ$) (C_2 hopping)	jump rate	angle of motion α ($^\circ$) (C_3 wobbling)	jump rate
173	226	0.52	19.5	1×10^7	22.5	1×10^7
193	216.1	0.45	20	1×10^7	23.7	1×10^7
213	208.5	0.378	20.5	1×10^7	24.5	1×10^7
233	201	0.31	20.8	1×10^7	24.9	1×10^7
253	192.2	0.24	21.2	1×10^7	25.4	1×10^7
273	188	0.182	22.3	1×10^7	25.7	1×10^7
293	182	0.115	23	1×10^7	26.2	1×10^7
313	176	0.05	24	1×10^7	26.7	1×10^7
333	170	-0.02	24.5	1×10^7	27.3	1×10^7
353	164	-0.08	24.9	1×10^7	28	1×10^7
373	158	-0.14	25.3	1×10^7	29	1×10^7

Table 3.3. VT ^{13}C static SSNMR simulation parameters^{3,4} for 0.5eq CO_2 loading.

0.5eq CO_2						
temperature (K)	Ω (ppm)	κ	angle of motion β ($^\circ$) (C_2 hopping)	jump rate	angle of motion α ($^\circ$) (C_3 wobbling)	jump rate
173	250.5	0.82	16	1×10^7	20	1×10^7
193	243	0.78	17	1×10^7	21	1×10^7
213	238	0.75	17.5	1×10^7	21.8	1×10^7
233	230	0.71	18	1×10^7	22.7	1×10^7
253	223	0.67	18.5	1×10^7	23.5	1×10^7
273	215	0.63	18.9	1×10^7	24	1×10^7
293	208	0.57	19.2	1×10^7	24.8	1×10^7
313	199	0.51	19.7	1×10^7	25.2	1×10^7
333	188	0.43	20.2	1×10^7	26	1×10^7
353	178	0.33	21	1×10^7	27	1×10^7
373	168	0.21	21.9	1×10^7	28	1×10^7

Table 3.4. VT ^{13}C static SSNMR simulation parameters^{3,4} for 0.75eq CO_2 loading.

0.75eq CO_2						
temperature (K)	Ω (ppm)	κ	angle of motion β ($^\circ$) (C_2 hopping)	jump rate	angle of motion α ($^\circ$) (C_3 wobbling)	jump rate
173	274	0.85	14	1×10^7	16	1×10^7
193	268	0.845	14.2	1×10^7	17	1×10^7
213	262	0.84	14.5	1×10^7	18	1×10^7
233	254	0.835	15	1×10^7	19	1×10^7
253	245	0.825	15.5	1×10^7	20	1×10^7
273	236	0.815	16.2	1×10^7	21.5	1×10^7
293	225	0.78	16.8	1×10^7	22.8	1×10^7
313	214	0.74	17.8	1×10^7	24	1×10^7
333	199	0.67	18.6	1×10^7	25	1×10^7
353	192	0.55	19.6	1×10^7	25.8	1×10^7
373	190	0.54	19.6	1×10^7	25.5	1×10^7

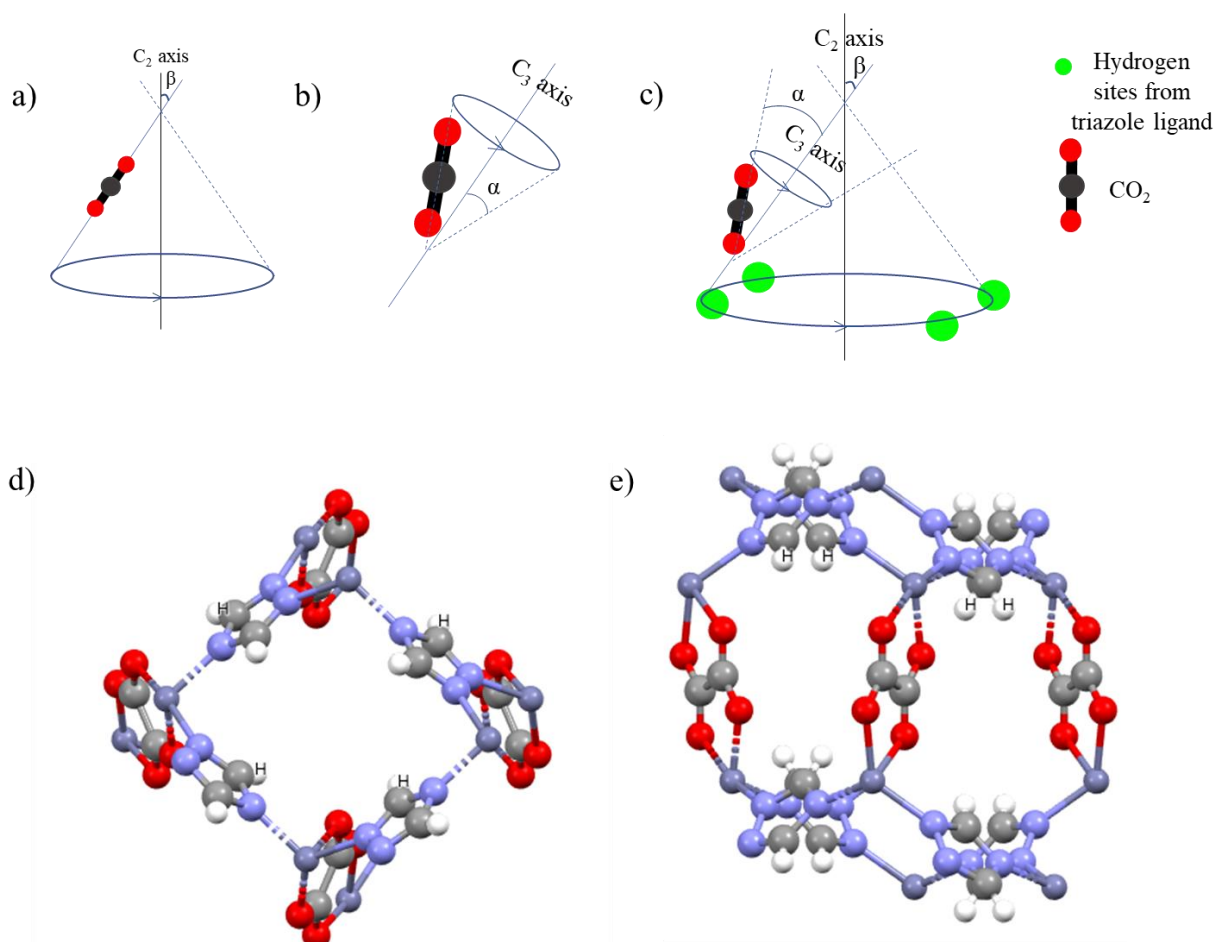


Figure 3.7. a) C₂ hopping motion of CO₂ molecule of 180° rotation about the C₂ axis scheme, b) C₃ wobbling motion scheme of CO₂, c) C₂ hopping + C₃ wobbling motion in the CALF-20 framework with pure CO₂ loadings. Hydrogen adsorption sites labeled as H on the CALF-20 framework d) top view, e) side view.

3.3.3. Adsorption scenarios

The CO₂ molecules for all three loadings in CALF-20 were predicted to have similar motions and occupations. The predictions on the occupation at different CO₂ loadings are demonstrated in **Figure 3.8**. At 0.25eq CO₂ loadings, half of the cages are occupied by 1 CO₂ molecule, while the other half of the cages remain empty. When the loading increases to 0.5eq CO₂, all of the cages are occupied by 1 CO₂ molecule. For 0.75eq CO₂ loading, half of the cages have 1 CO₂ molecule, and the other half contains 2 of the CO₂ molecules.

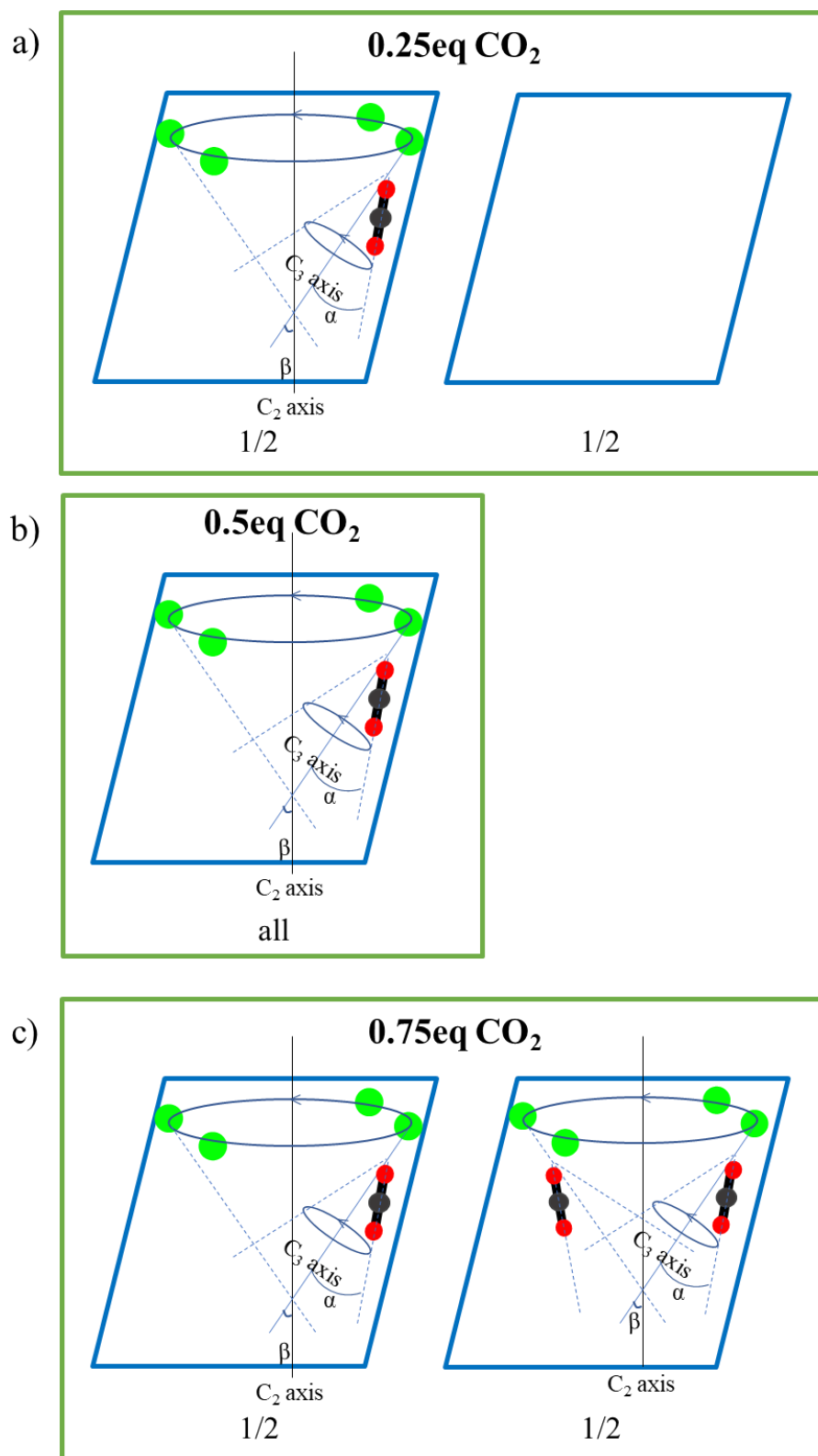


Figure 3.8. Adsorption scenarios of different CO₂ loadings in CALF-20.

3.3.4. MAS SSNMR

The ^1H - ^{13}C CP MAS SSNMR experiments were conducted on activated and loaded samples. The results were similar to those of ZTP-3 in **Chapter 2.3.6.**, adsorbed CO_2 signal at around 125 ppm was not seen on the ^1H - ^{13}C CP MAS spectrum (see **Figure 3.9. (a)**). 1-pulse experiments were conducted and confirmed that CO_2 was successfully loaded to the framework for the loaded samples (see **Figure 3.9 (b)**). Though the CO_2 adsorption cannot be seen on the CP MAS spectra, the structural signal of each carbon from the framework can be labelled. 2 signals were observed within CALF-20. The ^{13}C signal at 152 ppm arises from the carbon in the triazole group on the framework, and the second signal at 169 ppm originates from the carbon in the oxalate ligands (see **Figure 3.9. (c)**).

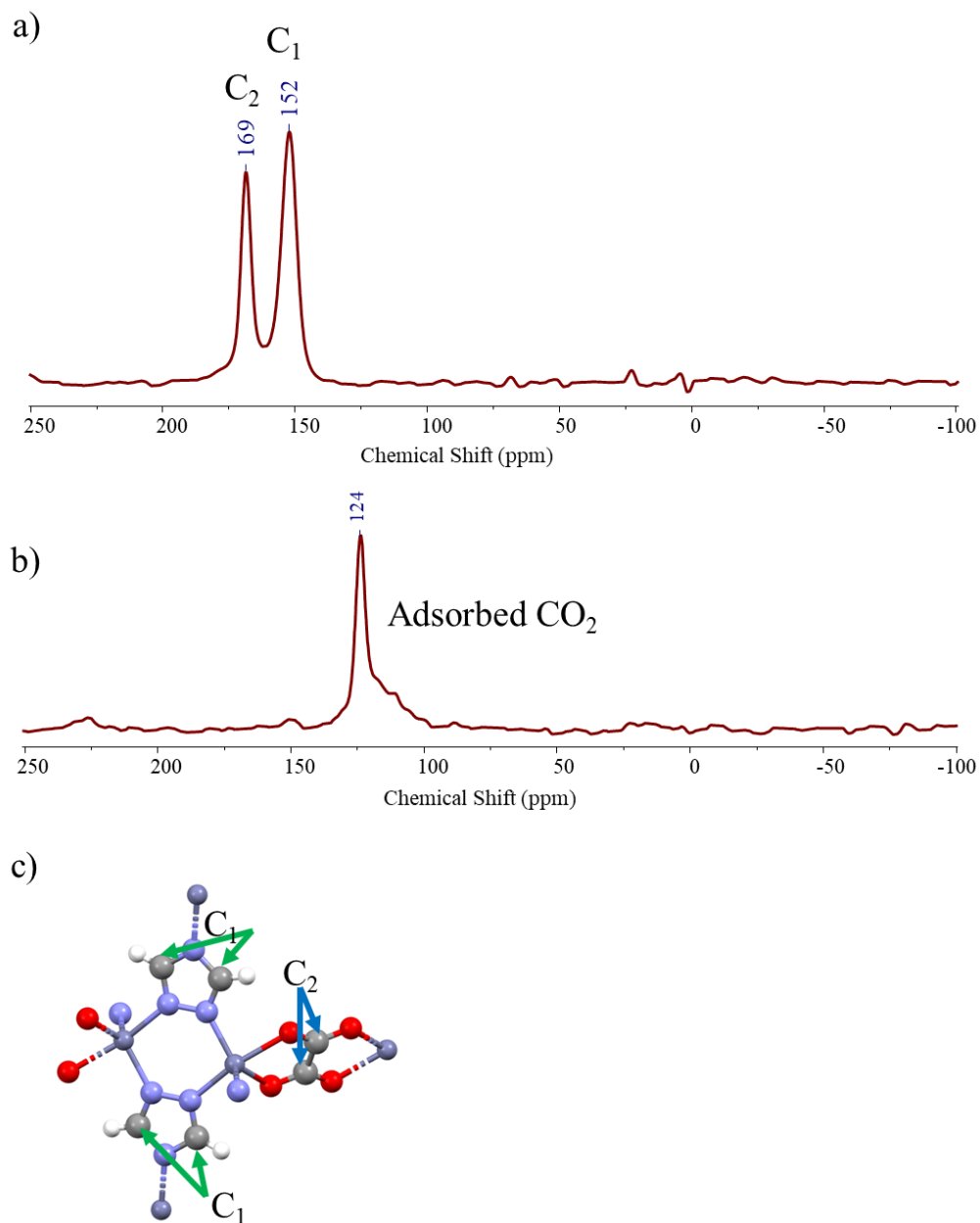


Figure 3.9. (a) ^1H - ^{13}C CP MAS SSNMR for 0.5eq CO_2 loaded CALF-20 framework. (b) One-pulse ^{13}C MAS SSNMR for 0.5eq CO_2 loaded CALF-20. (c) Asymmetric carbons on the CALF-20 framework structure.

3.4. Summary

Motional information of CO_2 adsorption behavior was first revealed using SSNMR. The analysis of ^{13}C static SSNMR spectra across different pure CO_2 loadings provided valuable insights on the

adsorption behavior of CO₂ in CALF-20. A single adsorption signal was consistently observed at approximately 125 ppm for all tested loadings, indicating that there is only one series of CO₂ adsorption motion within the CALF-20 framework, remained mobile across all loadings and temperatures.

At higher temperatures at the highest loading (0.75 eq), part of the CO₂ adsorbed to the framework became more mobile, which suggests that high temperature reduces the performance of the MOF's CO₂ adsorption capability.

Further simulation analysis allows us to reveal the detailed motional information originated from the signal. Two types of CO₂ motions were identified: C₂ hopping motion and C₃ wobbling motion. Interestingly, the angle of motion varied with temperature, with higher temperatures leading to larger motion angles and increased CO₂ mobility within the framework.

Although similar trends were observed across all pure CO₂ loadings, higher loadings resulted in broader signals and smaller motion angles, indicating that CO₂ undergoes more restricted motions within the framework. At room temperature for all loadings, no free CO₂ signal was observed, which indicates that all CO₂ was adsorbed into the framework. Thus, the amount of CO₂ adsorbed in CALF-20 was found to increase with increasing loading. The adsorption capacity of CALF-20 was also found to be closely related to temperature, the higher the temperature, the less CO₂ adsorbed to the framework.

References

1. Lin, J.-B.; Nguyen, T. T.; Vaidhyanathan, R.; Burner, J.; Taylor, J. M.; Durekova, H.; Akhtar, F.; Mah, R. K.; Ghaffari-Nik, O.; Marx, S.; Fylstra, N.; Iremonger, S. S.; Dawson, K. W.; Sarkar, P.; Hovington, P.; Rajendran, A.; Woo, T. K.; Shimizu, G. K. A Scalable Metal-Organic Framework as a Durable Physisorbent for Carbon Dioxide Capture. *Science* **2021**, *374* (6574), 1464–1469. <https://doi.org/10.1126/science.abi7281>.
2. Facelli, J. C.; Orendt, A. M.; Beeler, A. J.; Solum, M. S.; Depke, G.; Malsch, K. D.; Downing, J. W.; Murthy, P. S.; Grant, D. M.; Michl, J. Low-Temperature Carbon-13 Magnetic Resonance in Solids. 5. Chemical Shielding Anisotropy of the ¹³CH₂ Group. *J. Am. Chem. Soc.* **1985**, *107* (24), 6749–6754. <https://doi.org/10.1021/ja00310a001>.

3. Eichele K., Wasylishen R. E., WSolid1: Solid-State NMR Spectrum Simulation Package, ver. 1.20.21; Universität Tübingen: Tübingen, **2013**.
4. Vold, R. L.; Hoatson, G. L. Effects of Jump Dynamics on Solid State Nuclear Magnetic Resonance Line Shapes and Spin Relaxation Times. *J. Magn. Reson.* **2009**, 198, 57–72.
5. Stepanov, A. G.; Shegai, T. O.; Luzgin, M. V.; Essayem, N.; Jovic, H. Deuterium Solid-State NMR Study of the Dynamic Behavior of Deuterons and Water Molecules in Solid D₃Pw12O₄₀. *J. Phys. Chem. B* **2003**, 107 (45), 12438–12443. <https://doi.org/10.1021/jp030204c>.
6. Long, J. R.; Ebelhäuser, R.; Griffin, R. G. 2H NMR Line Shapes and Spin–lattice Relaxation in BA(CLO₃)₂·2H₂O. *J. Phys. Chem. A* **1997**, 101 (6), 988–994. <https://doi.org/10.1021/jp962116g>.
7. Morcombe, C. R.; Zilm, K. W. Chemical Shift Referencing in Mas Solid State NMR. *J. Magn. Reson.* **2003**, 162 (2), 479–486. [https://doi.org/10.1016/s1090-7807\(03\)00082-x](https://doi.org/10.1016/s1090-7807(03)00082-x).
8. Department of Chemistry. <https://chem.washington.edu/facilities/nmr> (accessed 2024-04-15).
9. Beeler, A. J.; Orendt, A. M.; Grant, D. M.; Cutts, P. W.; Michl, J.; Zilm, K. W.; Downing, J. W.; Facelli, J. C.; Schindler, M. S.; Kutzelnigg, W., Low-Temperature Carbon-13 Magnetic Resonance in Solids. 3. Linear and Pseudolinear Molecules. *J. Am. Chem. Soc.* **1984**, 106 (25), 7672-7676.

Chapter 4. Conclusions and future work

4.1. Conclusions

In this thesis, static VT ^{13}C SSNMR were carried out to investigate the CO_2 behavior within ZTP-3 and CALF-20. Static VT ^2H SSNMR were also carried out to observe the effects of D_2O on the CO_2 adsorption capability within ZTP-3. Gas loading levels and temperatures were altered in the experiment to monitor how the spectra change based on these variations. To extract spectral parameter and motional information from the static spectra, two simulation software packages were employed: 1) Wsolids¹ and 2) EXPRESS². For ^{13}C SSNMR spectra, CSA parameters including δ_{iso} , Ω and κ at variable temperature were extracted from Wsolids¹. For ^2H SSNMR spectra, C_Q and η_Q were obtained. The simulation patterns yielded from Wsolids¹ were then used for matching in EXPRESS². Motional information of CO_2 and D_2O including motional angles, motional rates and modes was then obtained from EXPRESS² simulations.

In Chapter 2, the CO_2 and D_2O adsorption behaviors in ZTP-3 were investigated. Single component and Co-adsorption experiment of these 2 molecules were carried out. The CO_2 in all cases were found to have 2 motions: 1) localized C_2 hopping motion and 2) non-localized C_3 wobbling motion. CO_2 in ZTP-3 was predicted to be adsorbed on the $-\text{NH}_2$ on the benzylic dicarboxylate ligand. Higher mobility of CO_2 was observed to be related to increase in temperatures. While higher CO_2 adsorption capability was found to be associated with lower temperatures. Water was found to exhibit 2 types of motions: (1) π -flipflop motion and (2) 4-site jumping motion. It was predicted to be adsorbed at the amine sites on the benzylic dicarboxylate group. Increase in D_2O loadings generally enhances CO_2 mobility according to the co-adsorption spectra. Water was found to have a negative effect on the CO_2 adsorption capacity of the MOF in most cases. However, there were exceptions, at 0.25eq CO_2 + 0.5eq D_2O loading, water was found to enhance the CO_2 adsorption within the MOF.

In Chapter 3, pure CO_2 adsorption behavior was investigated for CALF-20. CO_2 was found to have both localized C_2 hopping motion and non-localized C_3 wobbling motion at all temperature and loadings. The CO_2 molecules in CALF-20 was predicted to be adsorbed at the hydrogen sites attached to the triazole ring. Higher mobility of the adsorbed CO_2 was found to be associated with

higher temperatures and lower CO₂ loadings. Hence, to achieve a higher level of CO₂ adsorption in CALF-20, higher CO₂ loadings and lower temperatures would be required.

4.2. Future work

To draw a more precise conclusion for the water effects on carbon dioxide adsorption in ZTP-3, further experiments exploring variations in the CO₂ and D₂O loading ratios are necessary. The specific mechanism behind the enhancement of CO₂ adsorption remains unclear with limited data. Moreover, controlled experiments can be conducted to explore the influence of -NH₂ functional groups on the CO₂ adsorption capacity and behavior in MOF [Zn₂(TRZ)₂(BDC)], which shares a similar structure as ZTP-3.³

For CALF-20, investigating higher carbon dioxide loading and co-adsorption with water is essential, given its water-resistant properties. Obtaining static SSNMR at different humidity levels would help understanding the motional effects between CO₂ and D₂O molecules, which provides key information on maximizing CO₂ adsorption capacity, paving the way for better utilization in industries.

References

1. Eichele K., Wasylshen R. E., WSolids1: Solid-State NMR Spectrum Simulation Package, ver. 1.20.21; Universität Tübingen: Tübingen, **2013**.
2. Vold, R. L.; Hoatson, G. L. Effects of Jump Dynamics on Solid State Nuclear Magnetic Resonance Line Shapes and Spin Relaxation Times. *J. Magn. Reson.* **2009**, 198, 57–72.
3. Zhai, Q. G.; Bai, N.; Li, S.; Bu, X.; Feng, P. Design of Pore Size and Functionality in Pillar-Layered Zn-Triazolate-Dicarboxylate Frameworks and Their High CO₂/CH₄ and C₂ Hydrocarbons/CH₄ Selectivity. *Inorg. Chem.* **2015**, 54 (20), 9862–9868. <https://doi.org/10.1021/acs.inorgchem.5b01611>

Appendices

Appendix A2.

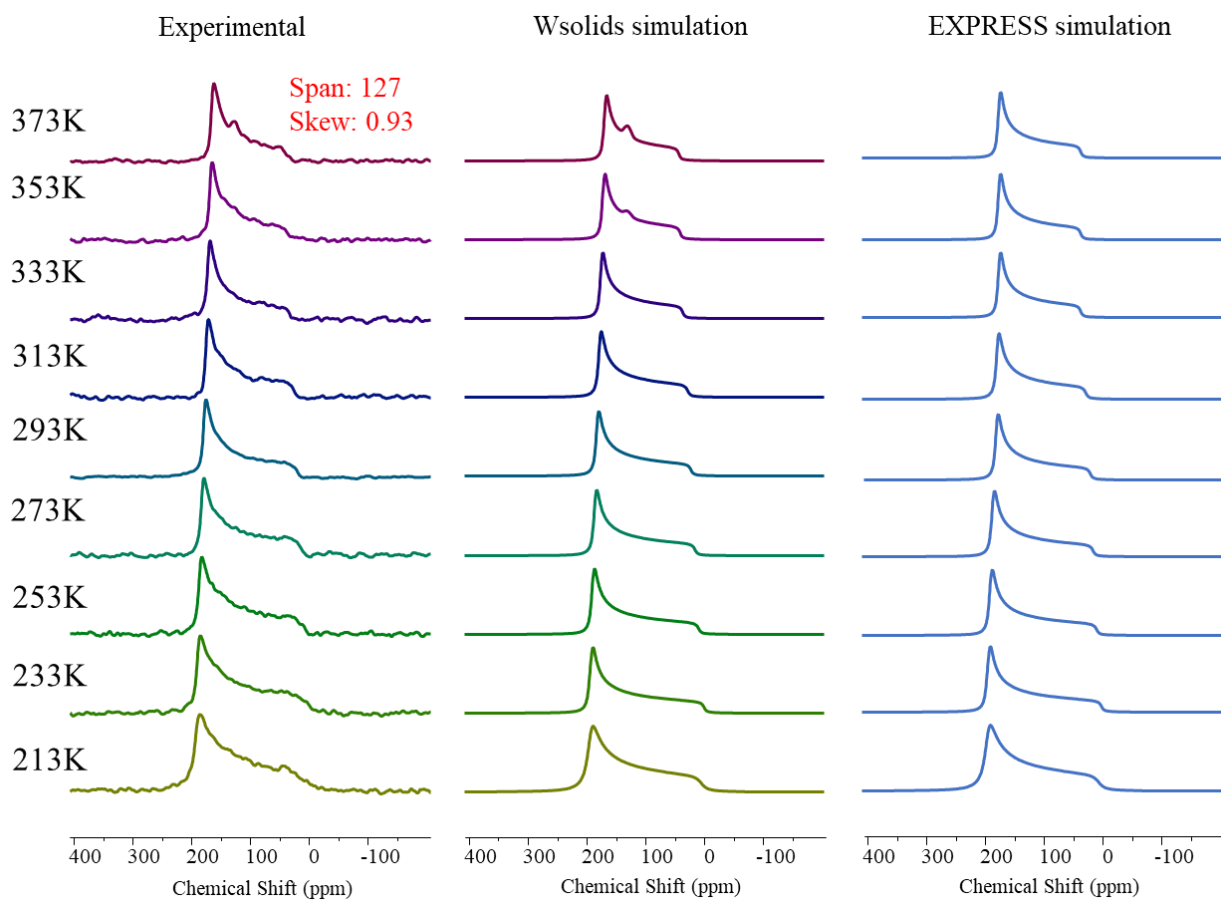


Figure A2.1. Experimental and simulated VT ^{13}C static SSNMR spectra at variable temperature with 0.25eqCO₂/Zn loading ZTP-3.

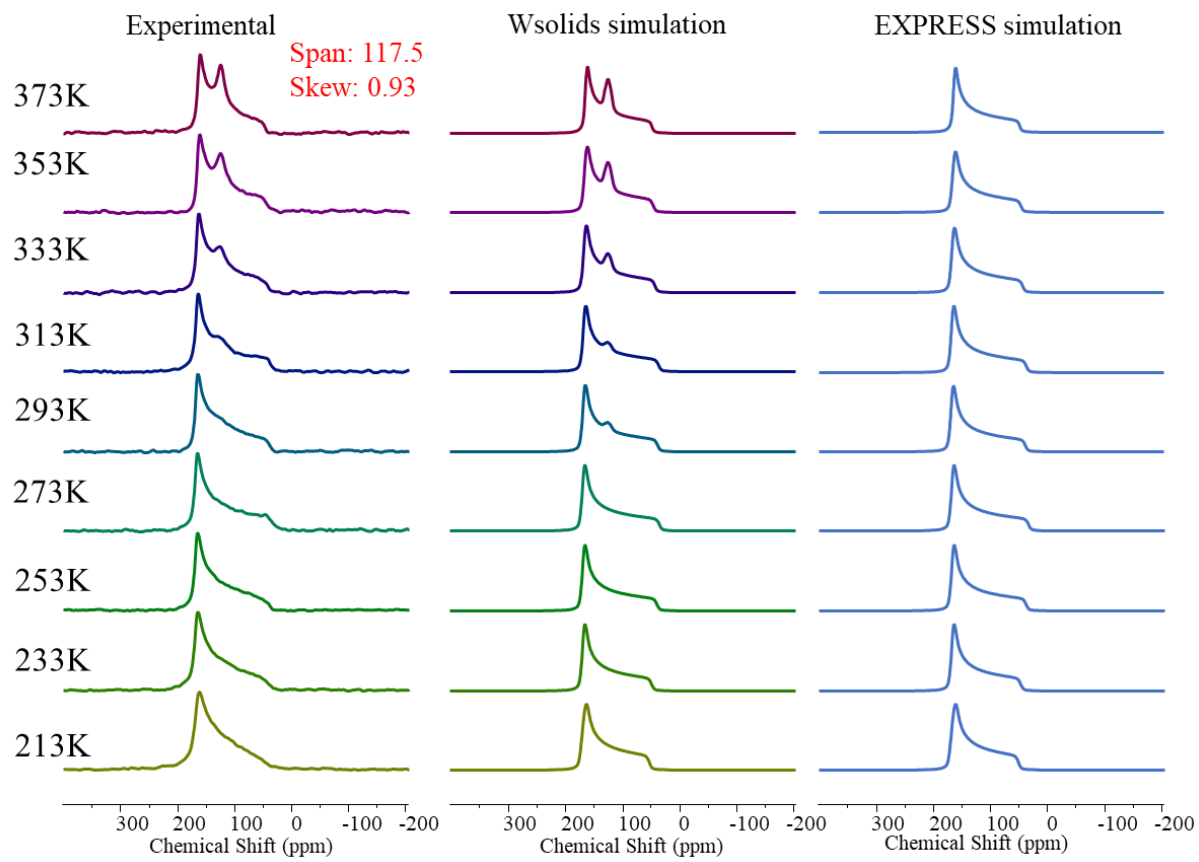


Figure A2.2. Experimental and simulated VT ^{13}C static SSNMR spectra at variable temperature with 0.5eqCO₂/Zn loading ZTP-3.

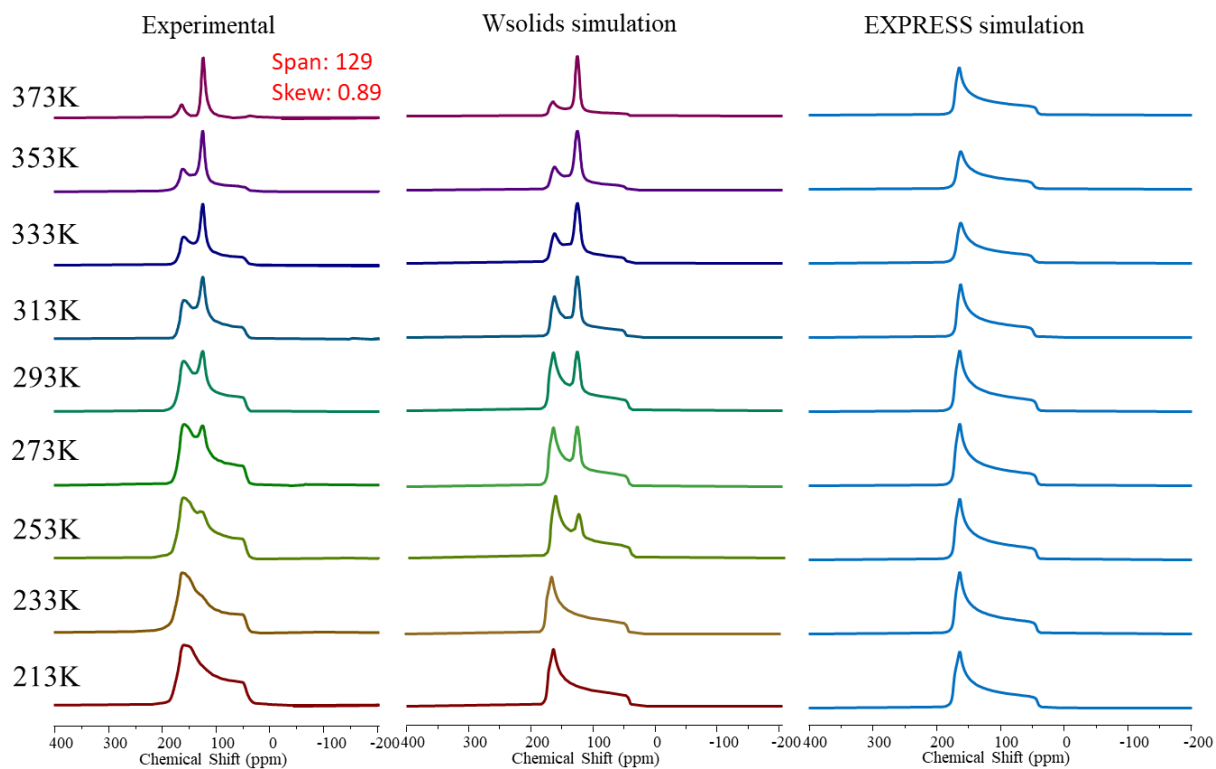


Figure A2.3. Experimental and simulated VT ^{13}C static SSNMR spectra at variable temperature with 0.75eqCO₂/Zn loading ZTP-3.

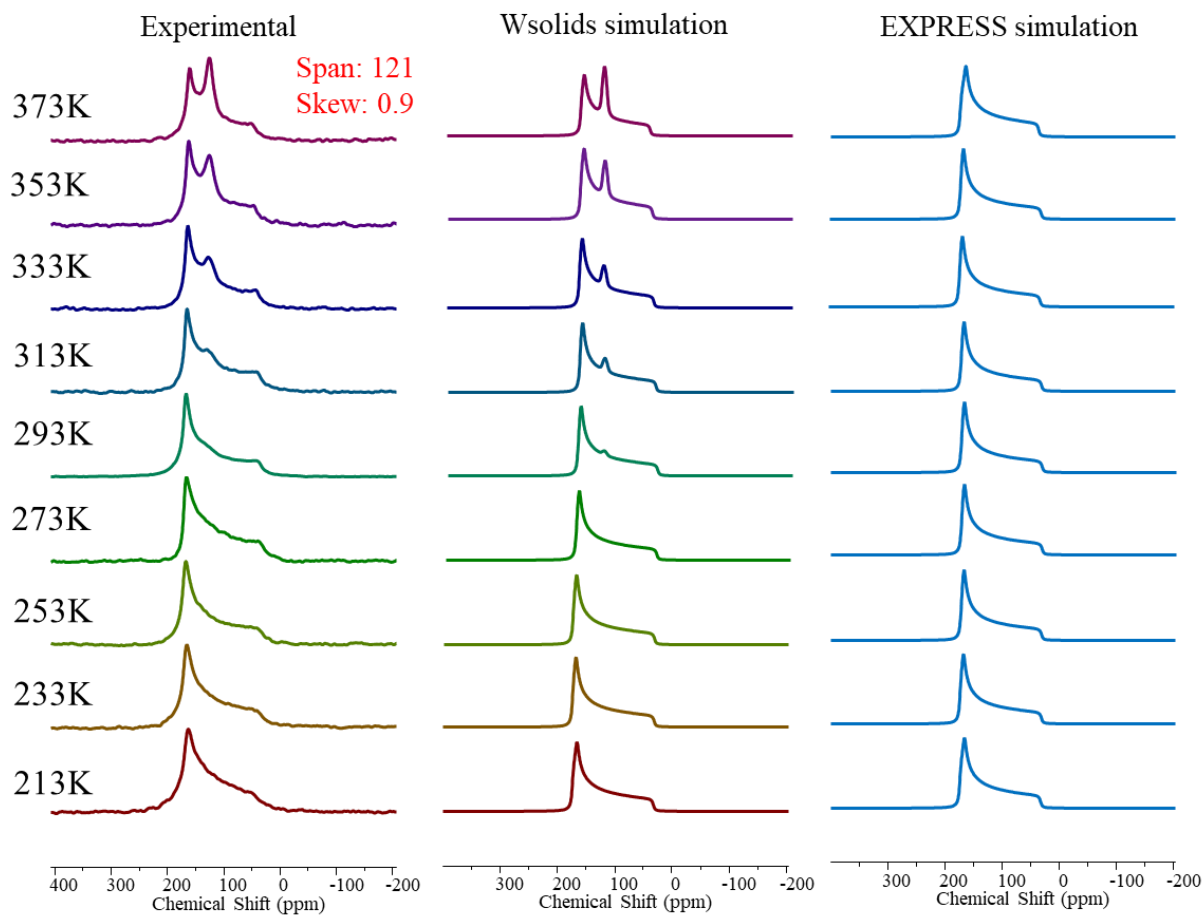


Figure A2.4. Experimental and simulated VT ^{13}C static SSNMR spectra at variable temperature with $0.25\text{eqCO}_2/\text{Zn}+0.25\text{eqD}_2\text{O}/\text{Zn}$ loading ZTP-3.

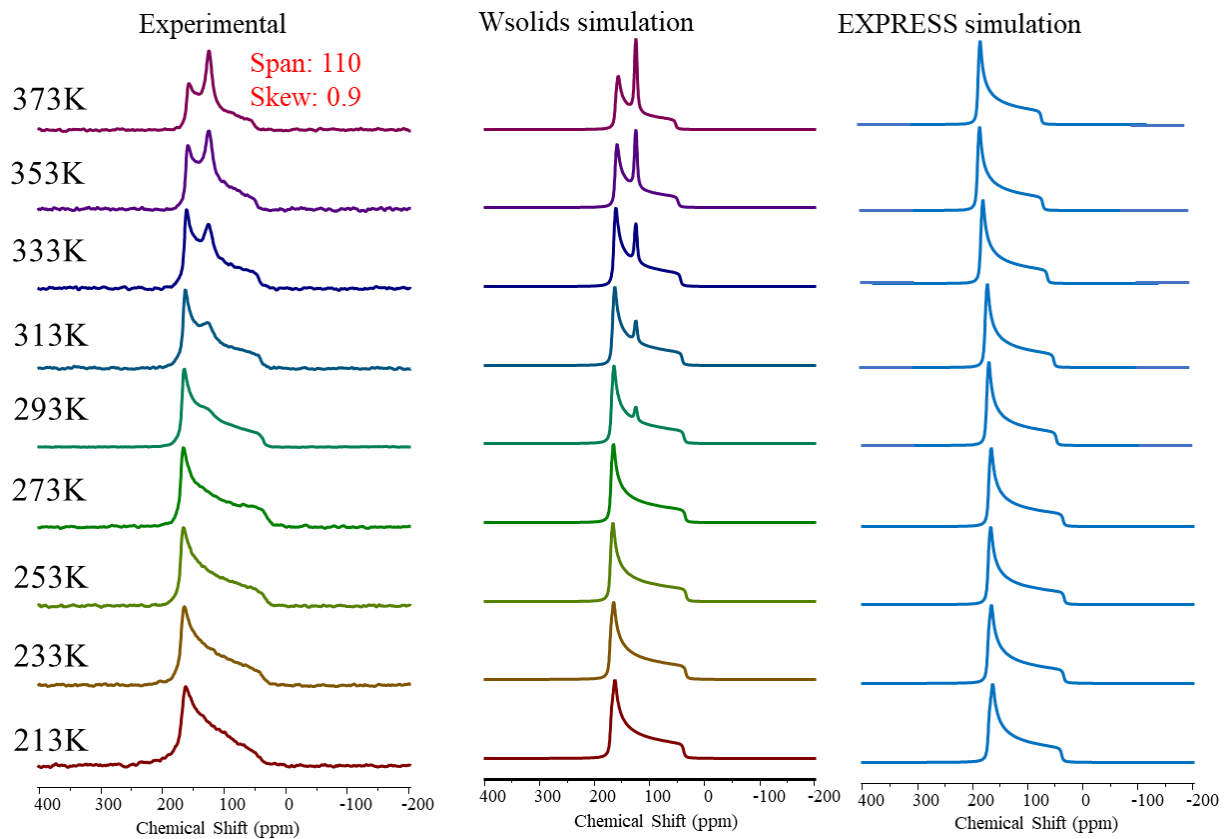


Figure A2.5. Experimental and simulated VT ^{13}C static SSNMR spectra at variable temperature with 0.25eq $\text{CO}_2/\text{Zn}+0.5\text{eqD}_2\text{O}/\text{Zn}$ loading ZTP-3.

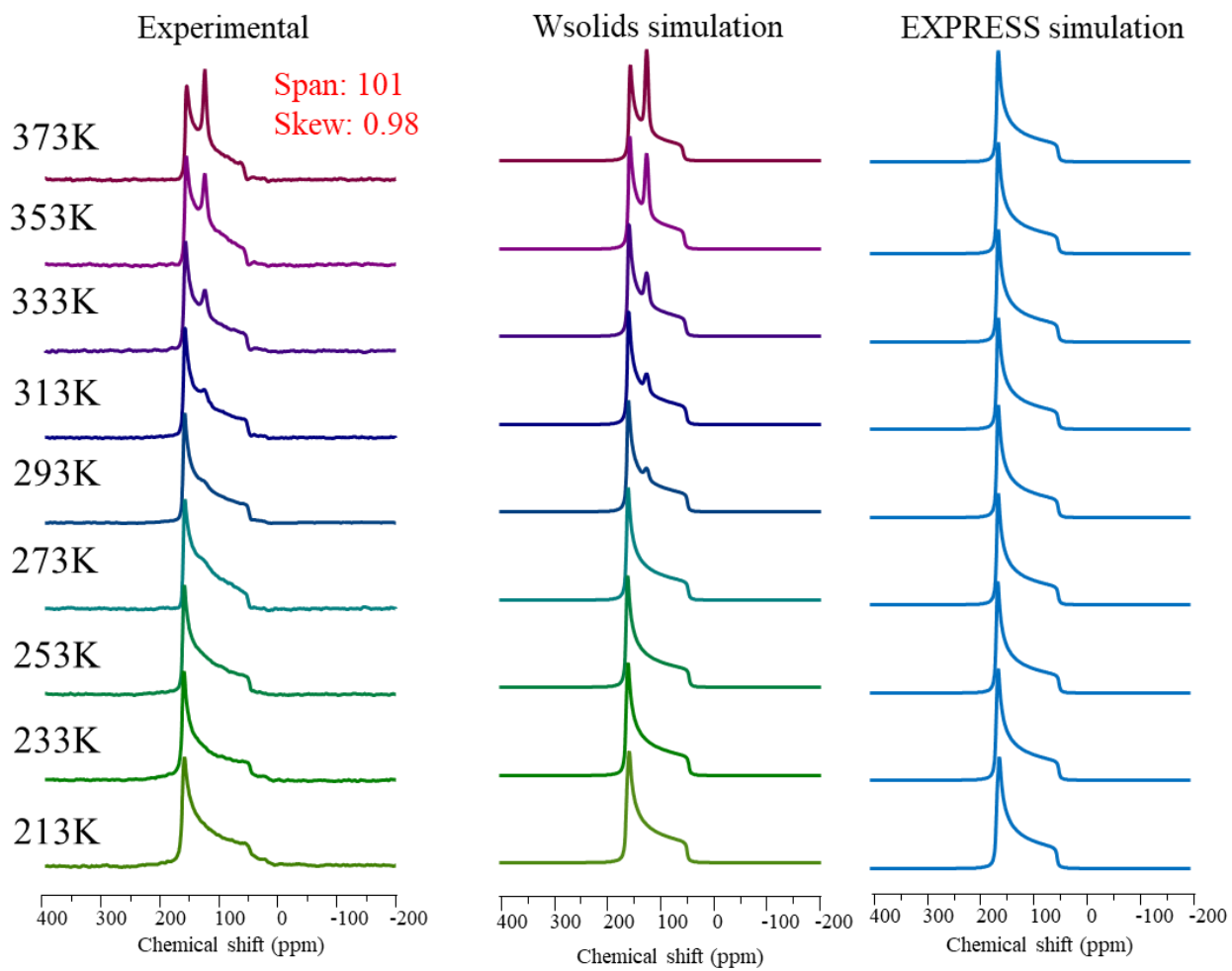


Figure A2.6. Experimental and simulated VT ^{13}C static SSNMR spectra at variable temperature with $0.25\text{eqCO}_2/\text{Zn}+1\text{eqD}_2\text{O}/\text{Zn}$ loading ZTP-3.

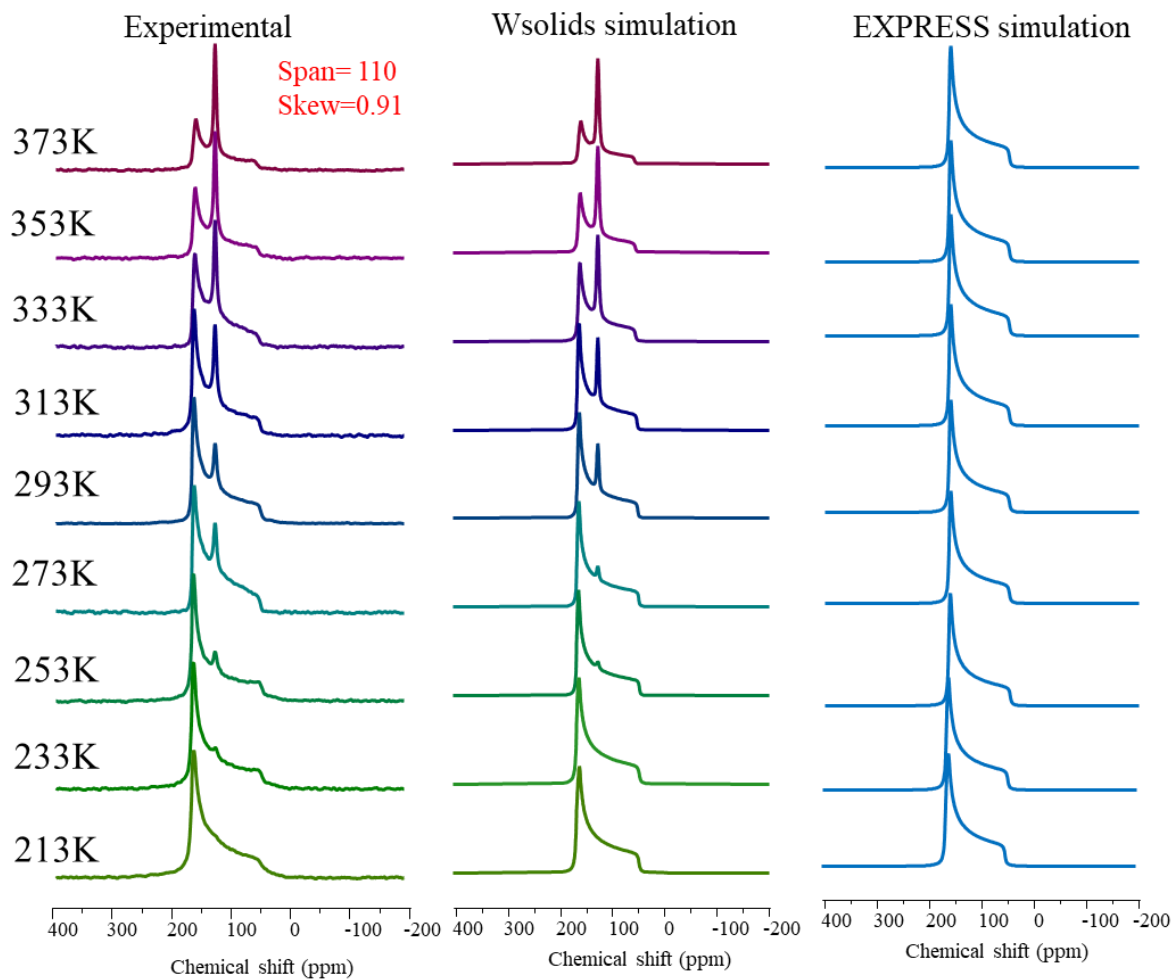


Figure A2.7. Experimental and simulated^{1,2} VT ¹³C static SSNMR spectra at variable temperature with 0.5eqCO₂/Zn+0.5eqD₂O/Zn loading ZTP-3.

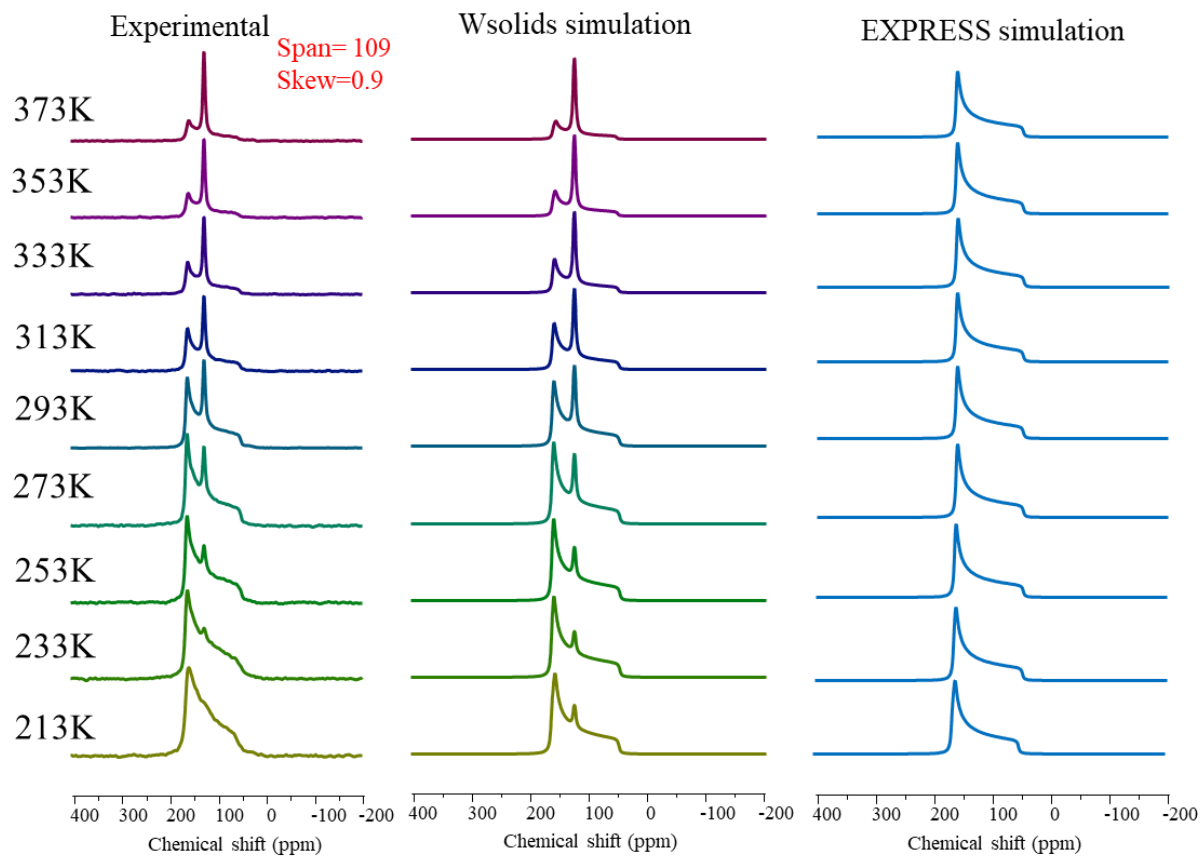


Figure A2.8. Experimental and simulated^{1,2} VT ¹³C static SSNMR spectra at variable temperature with 0.5eqCO₂/Zn+1eqD₂O/Zn loading ZTP-3.

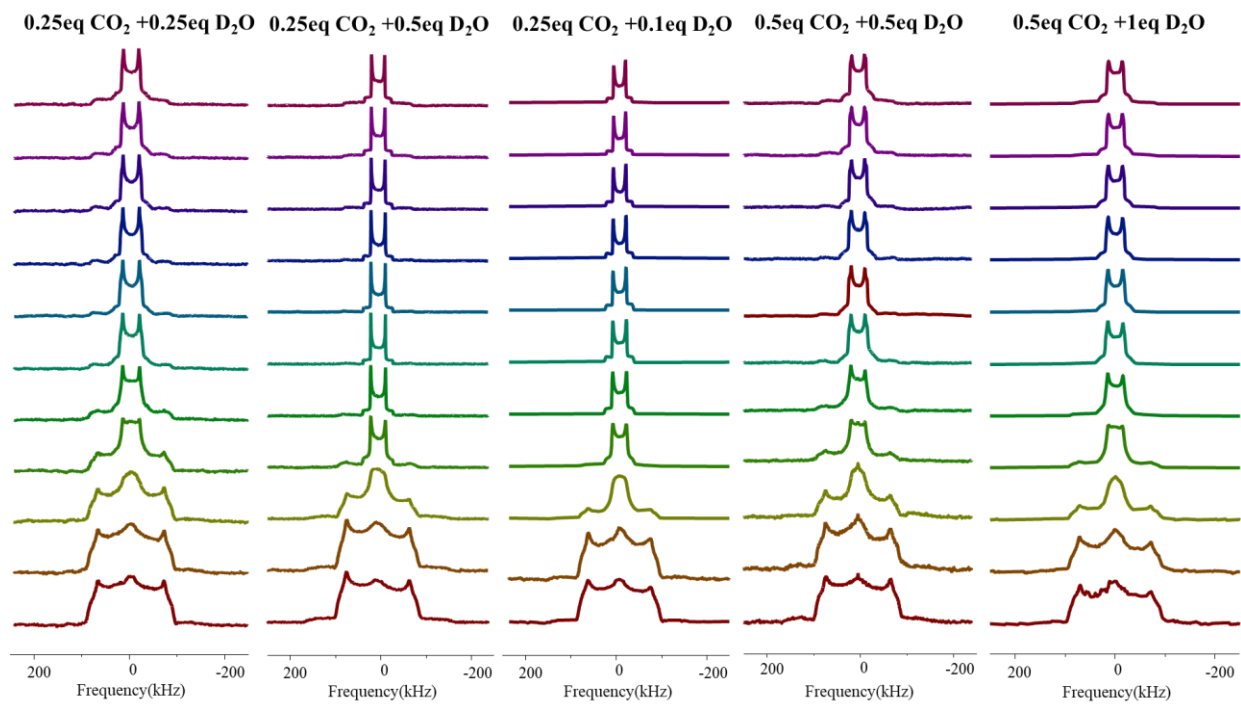


Figure A2.9. Experimental and simulated^{1,2} VT ^2H static SSNMR spectra at variable temperature for all coloaded samples of ZTP-3.

Table A2.1. VT ^{13}C static SSNMR simulation parameters of CO_2 signal 1 for 0.25eq CO_2/Zn

0.5eq CO_2						
Temperature (K)	Ω (ppm)	κ	angle of motion β ($^\circ$) (C_2 hopping)	jump rate	angle of motion α ($^\circ$) (C_3 wobbling)	jump rate
213	119	0.85	15	1×10^7	41	1×10^7
233	121	0.95	12.	1×10^7	40.7	1×10^7
253	130.5	0.95	12	1×10^7	39.5	1×10^7
273	135	0.95	12	1×10^7	39	1×10^7
293	131	0.95	12	1×10^7	39.5	1×10^7
313	132	0.95	12	1×10^7	40	1×10^7
333	125.3	0.93	12.5	1×10^7	40.7	1×10^7
353	121	0.92	12.5	1×10^7	41	1×10^7
373	117.5	0.93	12.5	1×10^7	41	1×10^7

Table A2.2. VT ^{13}C static SSNMR simulation parameters of CO_2 signal 1 for 0.75eq CO_2/Zn

0.75eq CO_2						
Temperature (K)	Ω (ppm)	κ	angle of motion β ($^\circ$) (C_2 hopping)	jump rate	angle of motion α ($^\circ$) (C_3 wobbling)	jump rate
213	132	0.85	15.5	1×10^7	39	1×10^7
233	132	0.86	15	1×10^7	39	1×10^7
253	129	0.87	14.5	1×10^7	39.5	1×10^7
273	129	0.87	14.5	1×10^7	39.5	1×10^7
293	129	0.87	14.5	1×10^7	39.5	1×10^7
313	129	0.89	14	1×10^7	39.5	1×10^7
333	129	0.89	14	1×10^7	39.5	1×10^7
353	129	0.89	14	1×10^7	39.5	1×10^7
373	129	0.89	14	1×10^7	39.5	1×10^7

Table A2.3. VT ^{13}C static SSNMR simulation parameters of CO_2 signal 1 for 0.25eq CO_2 + 0.25eq CO_2 + 0.5eq D_2O loading.

0.25eq CO_2 + 0.5eq D_2O						
Temperature (K)	Ω (ppm)	κ	angle of motion β ($^\circ$) (C_2 hopping)	jump rate	angle of motion α ($^\circ$) (C_3 wobbling)	jump rate
213	133	0.88	13	1×10^7	39	1×10^7
233	138	0.9	13	1×10^7	38.5	1×10^7
253	138	0.93	12.5	1×10^7	38.5	1×10^7
273	135	0.93	12.5	1×10^7	39	1×10^7
293	132	0.93	12.5	1×10^7	39	1×10^7
313	127	0.93	12.5	1×10^7	39.5	1×10^7
333	122	0.93	12.5	1×10^7	40	1×10^7
353	115	0.93	12.5	1×10^7	40.7	1×10^7
373	110	0.9	13	1×10^7	41.5	1×10^7

Table A2.4. VT ^{13}C static SSNMR simulation parameters of CO_2 signal 1 for 0.25eq CO_2 + 0.25eq CO_2 + 1eq D_2O loading.

0.25eq CO_2 + 1eq D_2O						
Temperature (K)	Ω (ppm)	κ	angle of motion β ($^\circ$) (C_2 hopping)	jump rate	angle of motion α ($^\circ$) (C_3 wobbling)	jump rate
213	114.5	0.9	14	1×10^7	40.5	1×10^7
233	118	0.94	12	1×10^7	40.7	1×10^7
253	117	0.97	10	1×10^7	40.7	1×10^7
273	115.4	0.97	10	1×10^7	41	1×10^7
293	113	0.97	10	1×10^7	41	1×10^7
313	110.5	0.97	10	1×10^7	41.5	1×10^7
333	108.3	0.97	10	1×10^7	42	1×10^7
353	104.5	0.97	10	1×10^7	42.5	1×10^7
373	101	0.98	10	1×10^7	42.5	1×10^7

Table A2.5. VT ^{13}C static SSNMR simulation parameters of CO_2 signal 1 for 0.25eq CO_2 + 0.5eq CO_2 + 0.5eq D_2O loading.

0.5eq CO_2 + 0.5eq D_2O						
Temperature (K)	Ω (ppm)	κ	angle of motion β ($^\circ$) (C_2 hopping)	jump rate	angle of motion α ($^\circ$) (C_3 wobbling)	jump rate
213	123	0.9	13	1×10^7	40	1×10^7
233	123	0.93	12.5	1×10^7	40	1×10^7
253	123	0.94	12	1×10^7	40	1×10^7
273	121	0.94	12	1×10^7	40	1×10^7
293	118	0.94	12	1×10^7	40.5	1×10^7
313	117	0.94	12	1×10^7	40.5	1×10^7
333	112	0.95	12	1×10^7	41	1×10^7
353	112	0.93	12.5	1×10^7	41	1×10^7
373	110	0.91	13	1×10^7	41.5	1×10^7

Table A2.6. VT ^{13}C static SSNMR simulation parameters of CO_2 signal 1 for 0.25eq CO_2 + 0.5eq CO_2 + 1eq D_2O loading.

0.5eq CO_2 + 1eq D_2O						
Temperature (K)	Ω (ppm)	κ	angle of motion β ($^\circ$) (C_2 hopping)	jump rate	angle of motion α ($^\circ$) (C_3 wobbling)	jump rate
213	115	0.89	14	1×10^7	40.5	1×10^7
233	116	0.93	12.5	1×10^7	40.5	1×10^7
253	115.5	0.95	12	1×10^7	40.5	1×10^7
273	115.2	0.95	12	1×10^7	40.5	1×10^7
293	114	0.95	12	1×10^7	40.5	1×10^7
313	114.5	0.94	12	1×10^7	40.5	1×10^7
333	112	0.94	12	1×10^7	41	1×10^7
353	111.5	0.91	13	1×10^7	41	1×10^7
373	109	0.9	13	1×10^7	41.5	1×10^7

Appendix A3

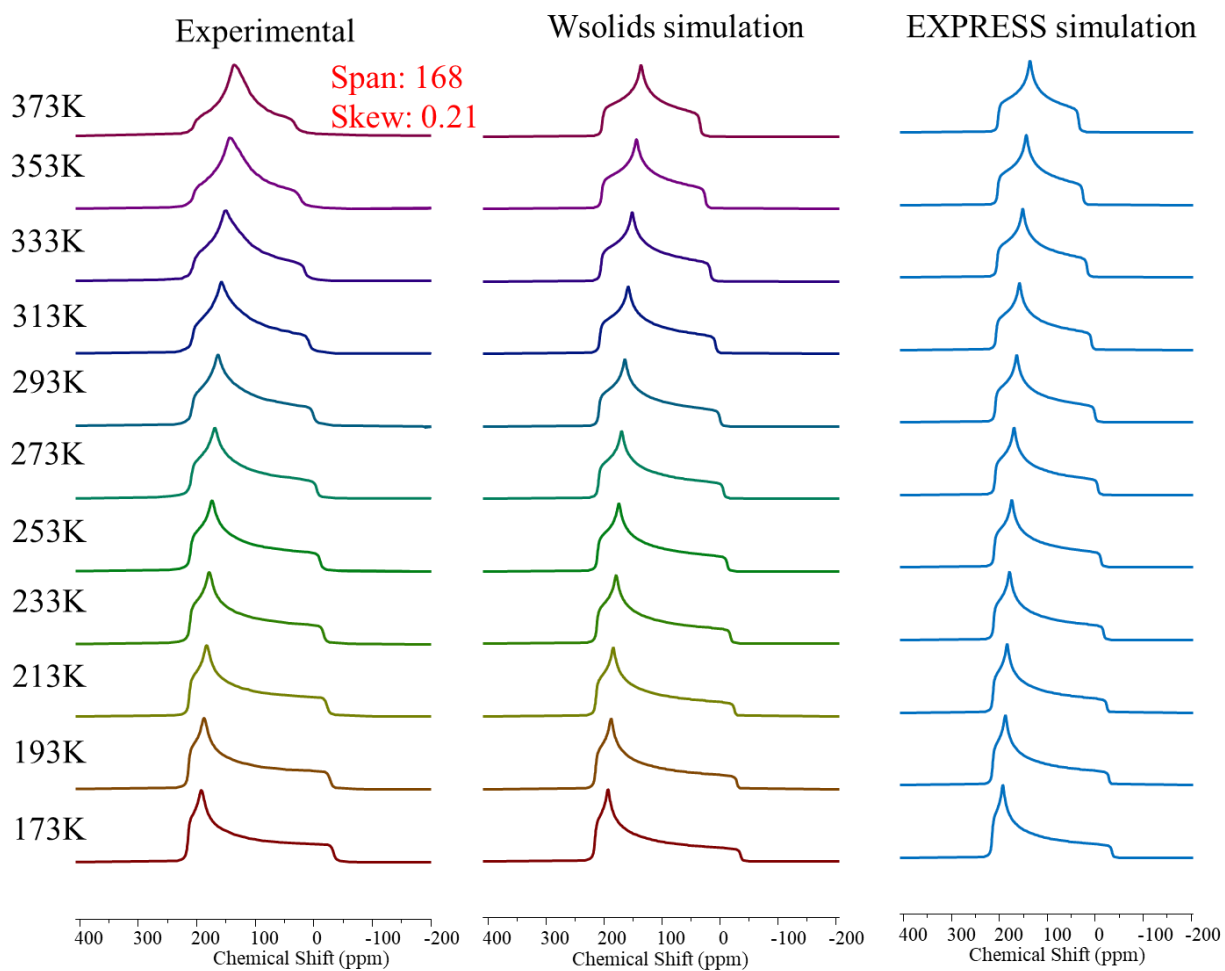


Figure A3.1. Experimental and simulated VT ^{13}C static SSNMR spectra at variable temperature with $0.5\text{eqCO}_2/\text{Zn}$ loading for Calf-20.

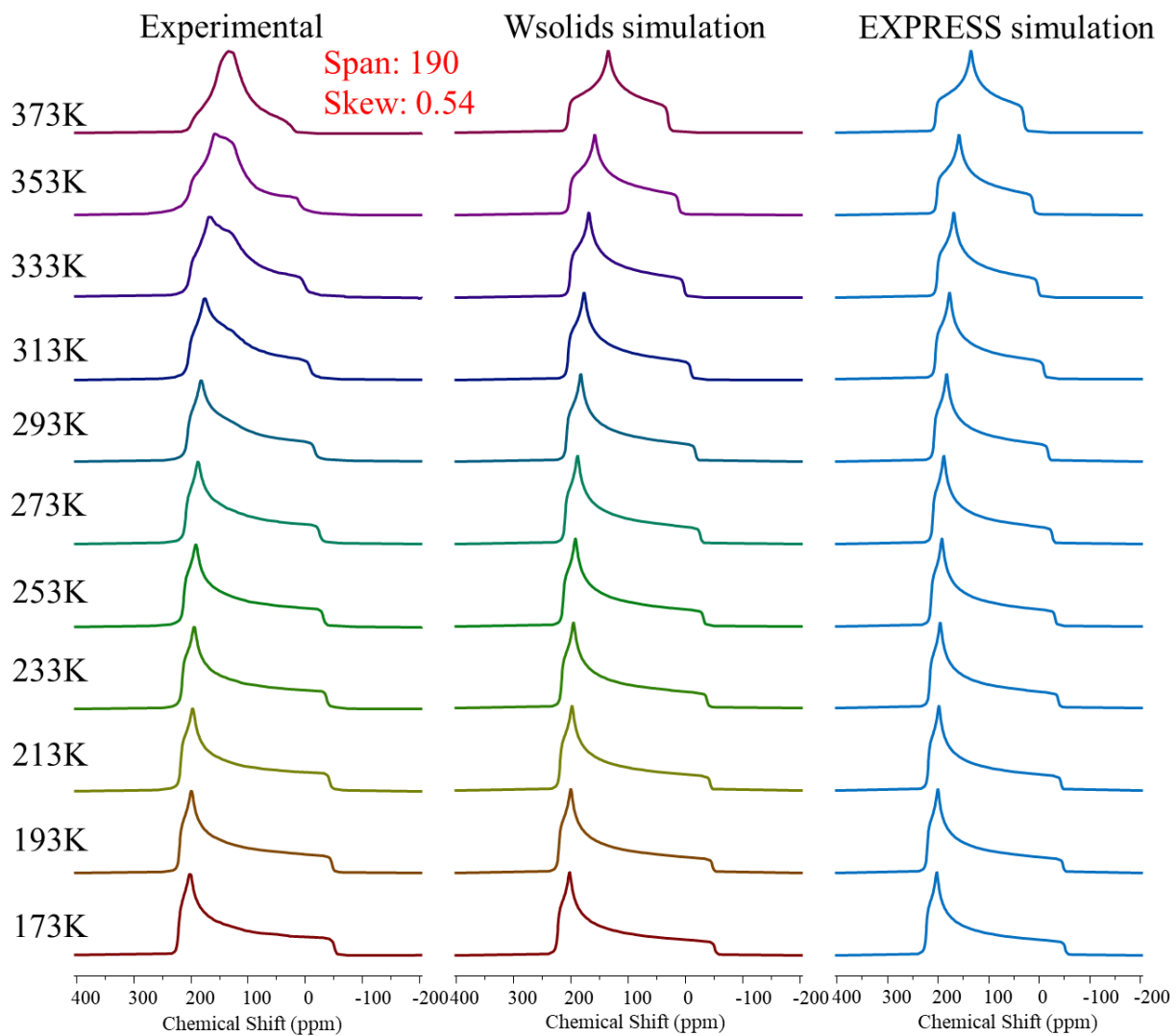


Figure A3.2. Experimental and simulated VT ^{13}C static SSNMR spectra at variable temperature with $0.75\text{eqCO}_2/\text{Zn}$ loading for Calf-20.

Curriculum Vitae

Yan Ham Ng

Education

- M.Sc. Chemistry** **University of Western Ontario** (London,
Sep 2021 to present Ontario – Canada) Supervisor: Prof. Dr. Yining
Huang
- B.Sc. Chemistry** **University of Western Ontario** (London,
Sep 2017 to May 2021 Ontario – Canada) Supervisor: Prof. Dr. Yining
Huang
-

Professional Experience

- Teaching Assistant** **University of Western Ontario**
Sep 2021 to present London, Ontario – Canada
- Lab Assistant** **University of Western Ontario**
Sep 2022 – April 2024 London, Ontario – Canada
-

Awards and Scholarships

- Poster presentation** 65th ICASS 2023 conference. University of Ottawa,
2023 Ottawa, ON, CA
- Poster presentation** MOOT 2022 NMR conference. University of Guelph,
2022 Guelph, ON, CA
- Albert E. Wells** Scholarship received during undergraduate degree
Scholarship
2019
- The Western** Scholarship received during undergraduate degree
Scholarship of
Excellence
2017

Summary of Course Work

Chemistry 9541 X-ray Crystallography Chemistry 9774Q	89
Synchrotron and Materials I	84
Chemistry 9784R Materials and Synchrotron Radiation II	96